

Analysis Note of the Experiment

Measurement of diffractive Central Exclusive Production of h^+h^- pairs ($h = \pi, K, p$) in proton-proton collisions at $\sqrt{s} = 200$ GeV with forward proton reconstruction in Roman Pot detectors

Leszek Adamczyk , Łukasz Fulek , Mariusz Przybycień , and Rafał Sikora

AGH University of Science and Technology, FPACS, Kraków, Poland

May 8, 2019

Abstract

In this note we present analysis of diffractive Central Exclusive Production using 2015 data from proton-proton collisions at $\sqrt{s} = 200$ GeV. This dataset was collected with newly installed Roman Pot detectors in Phase II* configuration which ensured efficient triggering and measuring diffractively scattered protons. We describe intermediate stages of analysis involving choice of selection cuts, comparison of data with Monte Carlo models folded into detector acceptance, and study of systematic uncertainties specific to the analysis. Finally, we show the physics outcome of the analysis. Parts of the analysis which are of more technical nature (calculation of efficiencies, derivation of corrections to efficiencies, adjustment of the STAR simulation, systematic uncertainty of efficiencies) are described in a supplementary analysis note [1].

ver. 0.9

Contents

List of contributions	4
Change log	4
1 Introduction	5
1.1 Central Exclusive Production	5
1.2 Double IPomeron Exchange	5
1.3 Physics motivation for the measurement	6
1.3.1 DIPE differential cross-sections, mass spectrum	6
1.3.2 Absorption effects	6
1.3.3 Size of interaction region	6
2 Data set	7
2.1 Trigger	7
2.2 Reconstruction software	8
2.3 Data format	8
3 Event selection	9
3.1 List of cuts	9
3.2 Description of cuts	10
3.2.1 (C1,C2) Primary vertex and its z -position	10
3.2.2 (C3) TPC tracks	10
3.2.3 (C4) RP tracks	14
3.2.4 (C5) TPC-RP z -vertex matching	14
3.2.5 (C6) BBC-large signal veto	14
3.2.6 (C7) TOF clusters limit	16
3.2.7 (C9) Exclusivity cut (missing p_T cut)	17
3.2.8 (C8) Particle identification	17
3.3 Signal per integrated luminosity	18
3.4 Cut flow	18
4 Corrections	19
4.1 Method of corrections application	19
4.2 Acceptances and efficiencies	19
4.2.1 Trigger efficiency	19
4.2.1.1 Online veto (BBC-small and ZDC veto)	19
4.2.1.2 RP triggering efficiency	20
4.2.1.3 Up and Down RP combination veto (due to dead material)	20
4.2.2 Selection efficiency	21
4.2.2.1 TPC z -vertex cut (C2)	21
4.2.2.2 TPC-RP z -vertex matching (C5)	22
4.2.2.3 Primary vertices limit (C1), BBC-large veto (C6), TOF clusters limit (C7) and Up and Down RP combination veto (due to pile-up)	22
4.2.2.4 Missing p_T cut (C9)	23
4.2.2.5 Particle identification (C8)	23
4.2.3 RP track acceptance and reconstruction efficiency	25
4.2.4 TPC vertex reconstruction efficiency	26
4.3 Particle energy loss	28
4.4 Background subtraction	28

5 Backgrounds	29
5.1 Sources of background	29
5.1.1 Non-exclusive background	29
5.1.2 Exclusive background (particle misidentification)	29
5.2 Relative normalization of background and signal	30
6 Systematic errors	31
7 Physics results	32
Appendix A BBC response	37
Appendix B Formulation of total RP efficiency	46
Appendix C Reconstruction of m_{TOF}^2	48
Appendix D RP efficiency	49
D.1 RP track acceptance, reconstruction and selection efficiency	49
D.2 RP trigger veto probability related to dead material	55
Appendix E Particle identification efficiency	61
List of Figures	63
List of Tables	63
References	65

List of contributions

Leszek Adamczyk	Analysis coordination/supervision, production of picoDST, production of embedded MC samples
Lukasz Fulek	Analysis support
Mariusz Przybycień	Analysis supervision
Rafał Sikora*	Main analyzer

* - contact editor

Change log

?? Apr 2019 ver. 1.0 Initial revision

1. Introduction

1.1 Central Exclusive Production

The Central Exclusive Production (CEP) takes place when interacting particles form a state in the mid-rapidity region (“central production”) whose all constituents/decay products are measured in the detector (“exclusive”). The initial state particles can either dissociate, excite or stay intact. The latter case of CEP in proton-proton collisions can be written as

$$p + p \rightarrow p + X + p \quad (1.1)$$

and depicted as in Fig. 1.2. Mass and rapidity of state X is given by

$$M_X = \sqrt{s \left(\xi_1 \xi_2 \sin^2(\alpha/2) - (1 - \xi_1 - \xi_2) \cos^2(\alpha/2) \right)} \stackrel{\alpha=\pi}{=} \sqrt{s \xi_1 \xi_2}, \quad (1.2)$$

$$y_X = \frac{1}{2} \ln \frac{\xi_1}{\xi_2}, \quad (1.3)$$

where α is angle between scattered protons and $\xi = (p_0 - p)/p_0$ is the fractional momentum loss of proton.

1.2 Double IPomeron Exchange

Reaction from Eq. (1.1) can exhibit purely electromagnetic ($\gamma\gamma$ interaction), mixed ($\gamma\mathcal{O}$ interaction) or purely strong nature ($\mathcal{O}\mathcal{O}$ interaction). The last type is dominant at RHIC energies. It is characterized by the lack of hard scale (if protons are scattered at small angles), therefore perturbative QCD cannot be applied and Regge theory [2] is used instead. An object \mathcal{O} does not have unequivocal QCD representation - in Regge formalism it is the so-called “trajectory” (IReggeon, IR). IReggeon with quantum numbers of vacuum is called “IPomeron” (IP) and IP-IP reaction (Fig. 1.1) is called “Double IPomeron Exchange“.

Processes involving IPomeron exchange are referred as diffraction due to cross-section in scattering angle resembling similar shape to intensity pattern of diffracted light. For low values of Mandelstam t (small scattering angles) cross-section takes exponential form

$$\frac{d\sigma}{dt} \propto e^{-B|t|}, \quad (1.4)$$

where the slope parameter B reflects the size of target at which IPomerons scatter.

Diffractive events have specific property of the ”rapidity gap“ which is an angular region free of hadrons. In DIPPE two such gaps are present, marked in Fig. 1.2 as $\Delta\eta_1$ and $\Delta\eta_2$. Figure 1.3 shows the topology of the DIPPE event on top of the STAR detector, with centrally produced particles marked with green arrows and two forward protons escaping the interaction point inside the beam pipe drawn with red arrows.

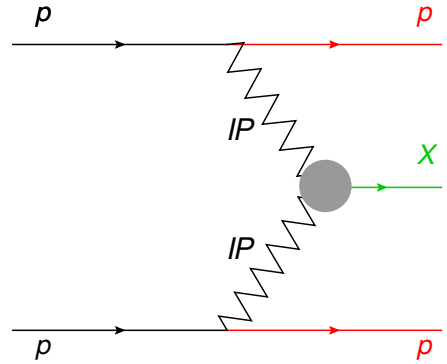


Figure 1.1: Diagram of DIPPE process.

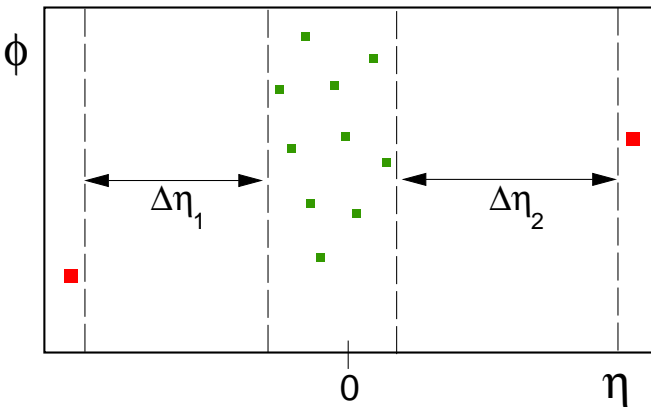


Figure 1.2: CEP represented in $\eta\phi$ space.

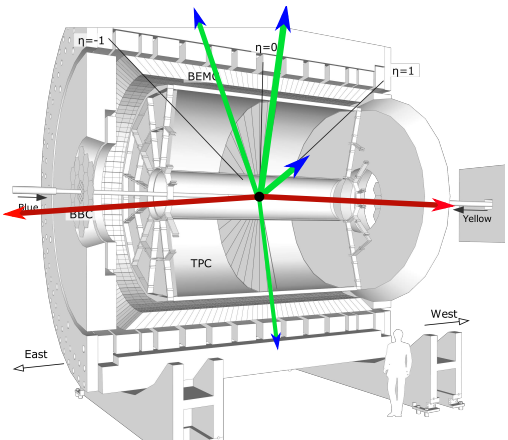


Figure 1.3: Central Production event at STAR.

DIPE is a spin-parity filter - the fact that scattered particles have all quantum numbers unchanged after the interaction, production of central states satisfying Eq. (1.5) is enhanced

$$I^G J^{PC} = 0^+ \text{even}^{++}. \quad (1.5)$$

The lowest order QCD picture of the IPomeron is a pair of oppositely colored gluons (colour singlet). This fact makes the DIPE recognized as the gluon-rich environment process in which bound states of gluons ("glueballs") or hybrid mesons could be preferably produced.

For detailed introduction to the topic of diffraction see Refs. [3, 4].

1.3 Physics motivation for the measurement

STAR collected in 2015 large dataset dedicated for measurement of the Central Diffraction (DIPE in particular). Since that year the experiment was enriched with Roman Pot Phase II* subsystem and thus gained possibility of detection of forward protons. It enabled studies of properties of the central state with respect to observables related to exchanged IPomerons. No such measurement was performed before at that high c.m.s. energy ($\sqrt{s} = 200$ GeV, contamination from Reggeon exchanges is small) which makes it particularly attractive. A brief list of physics issues that can be covered with the study described in this note is briefly introduced below.

1.3.1 DIPE differential cross-sections, mass spectrum

As stated in Sec. 1.2 DIPE is a soft process whose theoretical description is done mainly using phenomenological tools, thus measurement of differential cross-sections is needed to verify various production models.

The main focus is put on the simplest state (and most numerous) produced in DIPE, namely a pair of oppositely charged pions, $\pi^+\pi^-$. It can be formed either in a non-resonant or resonant mechanism. In the first case the $\pi^+\pi^-$ continuum is formed by the exchange of the off-shell pion between IPomerons. Currently there are two models of this reaction on the market [5, 6], [7]. In the second case the IPomerons directly couple into resonance (e.g. $f_2(1270)$), which then decays to $\pi^+\pi^-$. Attempts to calculate cross-section for this production mechanism are presented in Ref. [6] and [8].

Understanding of the mass spectrum in $\pi^+\pi^-$ channel is important to learn about relative contribution from continuum and resonant production, as well as relative production of resonances. Recognition of resonant states may indicate candidates for low-mass glueballs of $J^{PC} = 0^{++}$, however presence of underlaying scalar $q\bar{q}$ states makes this task challenging.

Other channels, like K^+K^- , are also of great interest. Comparison of the cross-sections for production of $\pi^+\pi^-$ and K^+K^- gives information about strength of the IPomeron coupling to different quark flavors. Also, structures in $d\sigma/dm$ can be easier attributed to resonances by measuring more than one channel and known branching ratios thereof.

Detection of intact protons scattered at very small angle with respect to the beamline enables determination of the reaction plane which makes the Partial Wave Analysis (PWA) possible. It also allows to look at the cross-sections more differentially, especially with respect to properties of exchanged IPomerons, like carried squared four-momentum t , azimuthal separation of IPomerons in the transverse plane $\Delta\varphi$ or relative momentum of IPomerons Δp_T . The last quantity was proposed to distinguish pure $q\bar{q}$ states from these with gluonic content [9].

1.3.2 Absorption effects

One can imagine in diagram in Fig. 1.1 additional soft lines e.g. between protons in the initial state or one of IPomerons and final state proton. These so-called rescattering effects (or absorption effects) lead to production of hadrons other than these belonging to central state X hence the diffractive signature of an event in form of rapidity gap is no longer present. Measurement of the probability that the state X will remain exclusive and forward protons will remain intact, in other words the rapidity gap survival probability S^2 , would be valuable ingredient for development of absorption models.

1.3.3 Size of interaction region

From the measurement of protons in Roman Pots one is able to reconstruct squared four-momenta transferred in proton-IPomeron vertices and determine the differential cross-section $d\sigma/d|t|$. Fit of exponent allows to extract the slope parameter B , which may depend on the IPomeron-IPomeron c.m.s. energy, or in other words on the mass of diffractive system X . Knowledge on the slope parameter gives insight to the form factor of the object at which IPomeron scatters.

2. Data set

2.1 Trigger

The main trigger designed for studies of Central Diffraction in run 15 was RP_CPT2. It was formed of the following conditions combined by logical AND ($\&\&$):

1. **(ET $\&\&$!IT) || (!ET $\&\&$ IT)** = signal in at least one RP on each side of the STAR central detector
- to ensure presence of two forward-scattered protons; a veto was imposed on simultaneous signal in RPs above and below the beamline, which might have originated either from proton dissociation, or pile-up event, or beam halo proton etc.,
2. **!BBC-E $\&\&$!BBCW $\&\&$!ZDCE $\&\&$!ZDCW** = veto on any signal in small BBC tiles or ZDCs on any side of STAR central detector - such requirement is in accordance with the double-gap topology of CEP events, it mostly filtered out CEP events with parallel pile-up event(s),
3. **TOF ≥ 2** = at least 2 hits in TOF - aim of this condition was to ensure activity in the mid-rapidity; since the lowest multiplicity allowed in CEP is 2, that was the lower threshold of L0 TOF multiplicity.

This trigger was running with an average prescale of 5 and average DAQ rate of 250 Hz, which allowed to collect in total about 560 M events corresponding to 16.5 pb^{-1} of integrated luminosity. More information about number of events per run, rates etc. can be found under link provided in Ref. [10], which contains selected data from STAR run log [11]. Luminosity data used in this analysis comes from Ref. [12].

All RP triggers which were intended for usage in diffractive physics analyses or efficiency studies are listed in Tab. 2.1. Components used in definitions of these triggers are outlined in Fig. 2.1. Detailed explanation of all trigger bits can be found in Refs. [13, 14]. Explanation of naming convention in Roman Pot system can be found in Ref. [15].

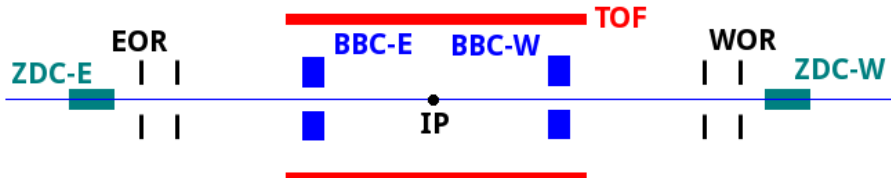


Figure 2.1: Sketch of the trigger components used in definitions of diffractive triggers in run 15.

Trigger name	Definition	Events [M]	Comment
RP_CP	EOR $\&\&$ WOR	73.3	Loose trigger (mostly elastic events) designed for monitoring/trigger efficiency study
RP_CPT	EOR $\&\&$ WOR $\&\&$!BBC-E $\&\&$!BBCW $\&\&$!ZDCE $\&\&$!ZDCW $\&\&$ TOF ≥ 1	38.9	Intended to be main CEP trigger (later switched to RP_CPT2 due to large prescale)
RP_CPT2	(ET $\&\&$!IT) (!ET $\&\&$ IT) $\&\&$!BBC-E $\&\&$!BBCW $\&\&$!ZDCE $\&\&$!ZDCW $\&\&$ TOF ≥ 2	556.5	Main CEP trigger Note: On Apr 14 added upper TOF limit (10)
RP_CPX	IT $\&\&$!BBC-E $\&\&$!BBCW $\&\&$!ZDCE $\&\&$!ZDCW $\&\&$ TOF ≥ 2	40.1	The same as RP_CPT2 but only IT configuration
RP_CPEI	ET $\&\&$ IT $\&\&$!BBC-E $\&\&$!BBCW $\&\&$!ZDCE $\&\&$!ZDCW $\&\&$ TOF ≥ 2	15.6	Control trigger for CPT2 to estimate effect of !(ET $\&\&$ IT) veto

Table 2.1: Central Diffraction physics triggers and control triggers involving Roman Pot detectors in run 15.

2.2 Reconstruction software

Raw data was processed with STAR libraries in versions SL17f. All four trigger datasets were processed: production_pp200trans_2015, production_pp200long2_2015, production_pp200long3_2015 and production_pp200long_2015 (see [16]).

The following BFC options were used in the reconstruction:

```
DbV20160418,pp2015c,btof,mtd,mtdCalib,pp2pp,-beamline,beamline3D,useBTOFmatchOnly,VFStoreX,  
fmsDat,fmsPoint,fpsDat,BEmcChkStat,-evout,CorrX,OSpaceZ2,OGridLeak3D,-hitfilt
```

Main attention should be put on option **useBTOFmatchOnly** which forced vertexing algorithm to form vertices only from the global TPC tracks which are matched with hits in the TOF system. This solution was found to yield significantly larger signal reconstruction efficiency (vertexing efficiency) and better resolutions. The study which lead to above conclusions, presented in Ref. [17], was performed on the same dataset processed with older libraries SL15k (without useBTOFmatchOnly option).

2.3 Data format

The analyzed data was stored in ROOT files in the picoDST format which was in large part a skimmed MuDST (standard STAR format). The picoDST format was introduced in Ref. [18]. PicoDST description files (C++ headers etc.) can be found in the analysis code repository [19].

3. Event selection

Complete list of analysis cuts used for signal extraction is presented in Sec. 3.1. Detailed description of each cut can be found in Sec. 3.2.

3.1 List of cuts¹

C1. Exactly 1 primary vertex with TPC track(s) matched with hits in TOF.

C2. TPC vertex from C1 is placed within $|z_{\text{vx}}| < 80$ cm.

C3. Exactly 2 opposite-sign primary TPC tracks (C3.2) of good quality (C3.4) matched with hits in TOF (C3.1), reconstructed within kinematic region of high TPC acceptance (C3.3), with small distance of closest approach (DCA) to the vertex (C3.5) and high proximity to each other at the beamline (C3.6).

C3.1. Exactly 2 TOF-matched (match flag > 0) primary tracks and no additional primary tracks matched with BEMC clusters,

C3.2. Tracks are of opposite signs,

C3.3. Both tracks are contained within the kinematic range: $|\eta| < 0.7$, $p_T > 0.2$ GeV/ c ,

C3.4. Both tracks satisfy quality criteria: $N_{\text{hits}}^{\text{fit}} \geq 25$, $N_{\text{hits}}^{\text{dE/dx}} \geq 15$, $|d_0| < 1.5$ cm,

C3.5. Both tracks match well to the primary vertex: $\text{DCA}(R) < 1.5$ cm, $|\text{DCA}(z)| < 1$ cm,

C3.6. Tracks are close to each other at the beamline: $|\Delta z_0| < 2$ cm.

C4. Exactly 1 RP track on each side of STAR central detector (C4.3) of good quality (C4.1), with local angles consistent with the IP being the track origin (C4.2), lying within fiducial region of high geometrical acceptance (C4.4).

C4.1. RP tracks contain only track-points with at least 3 (out of 4) planes used in reconstruction,

C4.2. Local angles (θ_x^{RP} , θ_y^{RP}) consistent with expectation for protons originating from the IP

$$-2 \text{ mrad} < \theta_x^{\text{RP}} - x^{\text{RP}}/|z^{\text{RP}}| < 4 \text{ mrad}, \quad -2 \text{ mrad} < \theta_y^{\text{RP}} - y^{\text{RP}}/|z^{\text{RP}}| < 2 \text{ mrad},$$

C4.3. Exactly 1 track passing cuts C4.1-C4.2 per side,

C4.4. Tracks passing cut C4.3 lie within the fiducial (p_x, p_y) region defined as:

$$0.2 < |p_y| < 0.4, \quad -0.2 < p_x, \quad (p_x + 0.3)^2 + p_y^2 < 0.5^2 \quad (\text{all in GeV}).$$

C5. Vertex z -positions measured in TPC and reconstructed from the difference of proton detection time in west and east RPs are consistent with each other within the resolution (at $3.5\sigma_{\Delta z_{\text{vtx}}}$ level):

$$|\Delta z_{\text{vtx}}| = |z_{\text{vx}}^{\text{TPC}} - z_{\text{vx}}^{\text{RP}}| < 36 \text{ cm}.$$

C6. No signal in any tile of BBC-large (east or west) with $\text{ADC} > \text{ADC}_{\text{thr}}$ and $100 < \text{TDC} < 2400$, where ADC_{thr} is specific for each channel.

C7. Maximally 3 reconstructed TOF clusters $N_{\text{clstrs}}^{\text{TOF}} \leq 3$.

C8. Particle (pair) identification:

C8.1. Identification of particle pairs based on dE/dx and m_{TOF}^2 :

```

if  $n\sigma_{\text{pion}}^{\text{pair}} > 3$  and  $n\sigma_{\text{kaon}}^{\text{pair}} > 3$  and  $n\sigma_{\text{proton}}^{\text{pair}} < 3$  and  $m_{\text{TOF}}^2 > 0.6$  GeV/ $c^2$  →  $p\bar{p}$ 
elif  $n\sigma_{\text{pion}}^{\text{pair}} > 3$  and  $n\sigma_{\text{kaon}}^{\text{pair}} < 3$  and  $n\sigma_{\text{proton}}^{\text{pair}} > 3$  and  $m_{\text{TOF}}^2 > 0.15$  GeV/ $c^2$  →  $K^+K^-$ 
elif  $|n\sigma_{\text{pion}}^{\text{trk1}}| < 3$  and  $|n\sigma_{\text{pion}}^{\text{trk2}}| < 3$  →  $\pi^+\pi^-$ 
else event rejected.

```

C8.2. Restricting fiducial cuts on K^+K^- and $p\bar{p}$:

```

if  $p\bar{p}$ :  $p_T > 0.4$  GeV/ $c$ ,  $\min(p_T^+, p_T^-) < 1.1$  GeV/ $c$ 
if  $K^+K^-$ :  $p_T > 0.3$  GeV/ $c$ ,  $\min(p_T^+, p_T^-) < 0.7$  GeV/ $c$ 

```

C9. Missing (total) momentum of TPC tracks and RP tracks $p_T^{\text{miss}} < 75$ MeV/ c .

¹Some cuts (e.g. C3) are decomposed to constituent sub-cuts. Cut is formed by the logical AND of all its sub-cuts. Events must pass all cuts to be identified as a signal.

3.2 Description of cuts

3.2.1 (C1,C2) Primary vertex and its z -position

As it was designed in the trigger logic, we aim to perform CEP analysis in a clean, pile-up-free environment, therefore we cut on primary vertex multiplicity (Fig. 3.1) to reject events with more than one interaction per bunch crossing. We require exactly one primary vertex containing TPC tracks matched with hits in TOF (matching of the track with hit in TOF is identified with the TOF match flag being different from 0). Later in the text we refer to such events as a single “TOF vertex” events.

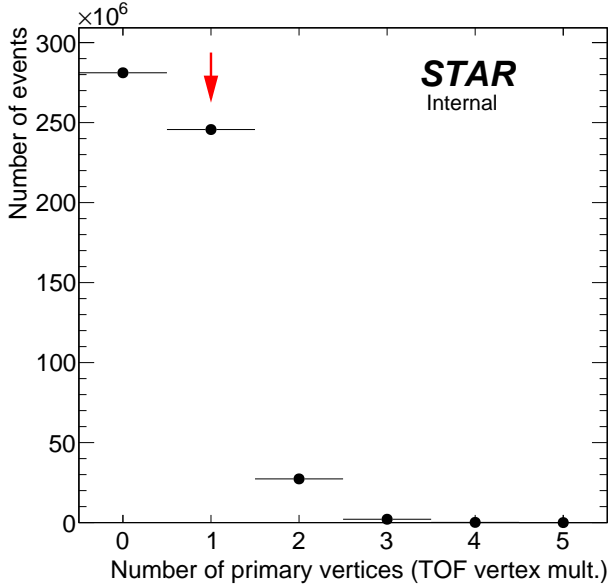


Figure 3.1: Primary vertex multiplicity. Red arrow marks bin with events with exactly one primary vertex (with track(s) matched with hit in TOF), which are used in physics analysis.

The single TOF vertex is required to be placed within a range (-80 cm, 80 cm) along the z -axis (Fig. 3.2). Events with vertices away from the nominal IP have low acceptance both for the central tracks and the forward protons (comparing to events with vertices close to nominal IP), therefore we reject them as their inclusion to analysis would naturally introduce large systematic uncertainties. See Sec. 3.2.3 in Ref. [1]

3.2.2 (C3) TPC tracks

The TPC track selection starts from the selection of events with exactly two primary tracks matched with hit in TOF (Fig. 3.3). Matching with TOF guarantee that analyzed tracks originate from the triggered bunch crossing (ensures that tracks are “in-time”). It is in accordance with the trigger logic which required at least 2 L0 TOF hits, as well as it enables more accurate particle identification with merged time-of-flight and dE/dx method, comparing to sole usage of dE/dx . Primary tracks not matched with hit in TOF, whose average multiplicity in single TOF vertex is ~ 8 , are hardly distinguished between real and fake (off-time) tracks, which is an additional reason for not analyzing events with only one TOF-matched primary TPC track (the other track might be unmatched due to TOF inefficiency).

Primary TPC tracks from the single TOF vertex which are matched with TOF are allowed to be also matched with BEMC clusters. Matching with BEMC cluster is claimed if the distance in $\eta - \phi$ space between the BEMC cluster position (η_{clus} , ϕ_{clus}) and projected position of the track in BEMC (η_{proj} , ϕ_{proj}), defined as

$$R = \sqrt{(\eta_{\text{clus}} - \eta_{\text{proj}})^2 + (\phi_{\text{clus}} - \phi_{\text{proj}})^2}, \quad (3.1)$$

is less than $R_{\text{max}}^{\text{match}} = 0.05$. Distribution of the distance between the primary TPC track and the closest BEMC cluster is shown in Fig. 3.4.

However, if there are any primary TPC tracks matched with BEMC cluster and not matched with TOF in the single TOF vertex with two TOF-matched tracks, an event is rejected. Such configuration implies higher-than-2 multiplicity of the real tracks in the vertex, hence an event is unlikely a Central Exclusive Production of two particles.



Figure 3.3: Multiplicity of primary TPC tracks matched with hit in TOF for single TOF vertex events. Red arrow marks bin with events with exactly two primary tracks matched with hit in TOF, which are used in physics analysis.



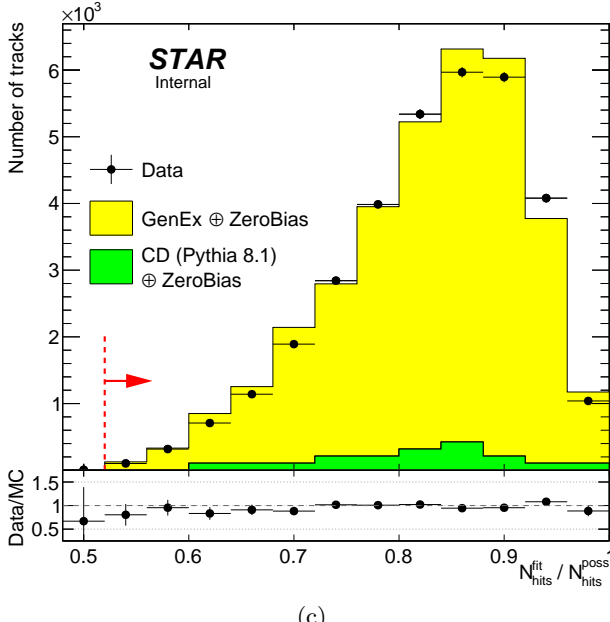
Figure 3.4: Distribution of a distance in $\eta - \phi$ space between the BEMC cluster closest to primary TPC track matched (filled circle) or not matched (open circle) with hit in TOF, for single TOF vertex events. Red dashed line indicate matching threshold $R_{\max}^{\text{match}} = 0.05$.



(a)



(b)



(c)

Figure 3.5: Comparison of distribution of the number of hits used in TPC track reconstruction $N_{\text{hits}}^{\text{fit}}$ (3.5a), number of hits used in specific energy loss reconstruction $N_{\text{hits}}^{\text{dE/dx}}$ (3.5b) and fraction of number of hits potentially generated by the track and finally used in the reconstruction $N_{\text{hits}}^{\text{fit}} / N_{\text{hits}}^{\text{poss}}$ (3.5c) in the data and embedded MC. Normalizations of the signal and backgrounds were established from the comparison of p_T^{miss} and $\Delta\theta$ distributions after full selection (without cut on the presented quantity and without exclusivity cut), as described in Sec. 5.2. Red dashed line and red arrow indicate the range of each quantity which is accepted in analysis.



Figure 3.6: Comparison of the track pseudorapidity η (3.6a) and the track azimuthal angle ϕ (3.6b) in the data and embedded MC. Normalizations of the signal and backgrounds were established from the comparison of p_T^{miss} and $\Delta\theta$ distributions after full selection (without cut on the presented quantity and without exclusivity cut), as described in Sec. 5.2. Red dashed lines and red arrows indicate the range of each quantity which is accepted in analysis.

3.2.3 (C4) RP tracks

3.2.4 (C5) TPC-RP z -vertex matching

In CEP tracks in the central detector and tracks in Roman Pots originate from the same interaction vertex. Measurement of the time of detection of forward protons in RPs gives access to reconstruction of the position of the vertex

$$z_{\text{vtx}}^{\text{RP}} = c \cdot \frac{t_{\text{W}}^{\text{RP}} - t_{\text{E}}^{\text{RP}}}{2} \quad (3.2)$$

independently from TPC, which allows their comparison and rejection of the background if the two values disagree. Time of detection of proton in RP is provided in StMuRpsTrack object - it is an average of all TAC values from PMTs in RPs used to form a track, corrected for the slewing effect and adjusted to have the best correlation with the z -position of the vertex measured in TPC, translated to unit of time (all these steps are done at the level of raw data reconstruction). In Fig. 3.7 the comparisons of the $z_{\text{vtx}}^{\text{RP}}$ and $z_{\text{vtx}}^{\text{TPC}}$ are shown with some preselection cuts applied. A clear signal from the Central Diffraction (and thus CEP) process is manifesting in high correlation of the two values (diagonal in Fig. 3.7a) or significant and relatively narrow peak centered at 0 for the difference of two values (Fig. 3.7b). The sum of two Gaussian distributions was

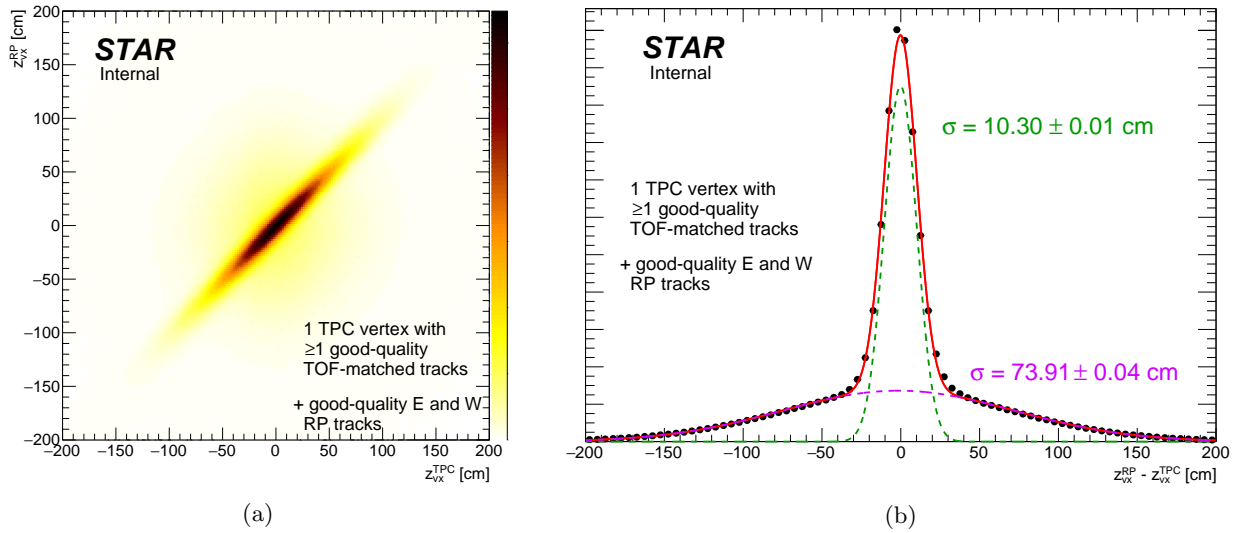


Figure 3.7: Correlation (Fig. 3.7a) and difference (Fig. 3.7b) of z -vertex position measured in Roman Pots and TPC in RP_CPT2 triggers, after preselection described in the plots.

fitted to data in Fig. 3.7b yielding good description of the distribution of Δz_{vtx} with the width parameters equal 10.3 cm (CD signal) and 73.9 cm (pile-up). The first parameter reflects the time resolution of RPs (the $z_{\text{vtx}}^{\text{RP}}$ measurement), as the TPC resolution is much better (~ 1 cm). Value of the second parameter, consistent with $\sqrt{2}\sigma_{z_{\text{vtx}}} \approx \sqrt{2} \cdot 52$ cm ≈ 73.5 cm, confirms that the wide distribution under the narrow signal peak is uncorrelated background, in other words forward protons originating from a different vertex than the central tracks. To reject this background without significant loss of the signal, we introduce $3.5\sigma_{\Delta z_{\text{vtx}}}$ cut on Δz_{vtx} .

3.2.5 (C6) BBC-large signal veto

At the trigger level a veto on signal in small BBC detectors was used. During offline analysis we found that the non-exclusive background can be efficiently rejected if an additional veto on signal in large BBC detectors is added. It is connected with the fact that vast majority of selected RP_CPT2 triggers were from the central diffraction process to which CEP belongs. Many of central diffraction events have particles produced in the rapidity region outside the TPC and TOF acceptance, some hitting large BBC tiles. Presence of signal in large BBC is therefore a signature of background or a pile-up interaction.

The response of large BBC tiles is different from that of small BBC tiles, as shown in sample plots in Fig. ?? (similar distributions for all channels can be found in Appendix A). Typically in small BBC tiles a peak visible in ADC distribution around 100 – 150 (Figs. 4.5a,4.5c), a signature of good separation of the electronics noise and signal from the ionizing particle. No such feature is observed in corresponding distribution for large BBC tile (Figs. 4.5b,4.5d), which can be explained by the difference in geometry (in size) of small and large tiles. In large BBC tiles the path that scintillation light must travel to reach PMT is much longer in comparison to small BBC tiles (multiple reflections on the main tile surface due to small thickness of the tile) therefore it is highly

attenuated and extended in time. This is possible reason of lack of signal peak in the ADC distribution in large BBC tile spectrum (Fig. 4.5d), as well as the late-TAC (TAC < ~600, ADC < 100) tail in the ADC vs. TAC spectrum (slewing effect, Fig. 4.5b). Nevertheless, the above features of BBC-large response does not disqualify this detector from being used as a veto detector, as in this case lower efficiency of the detector only reduce the background rejection power.

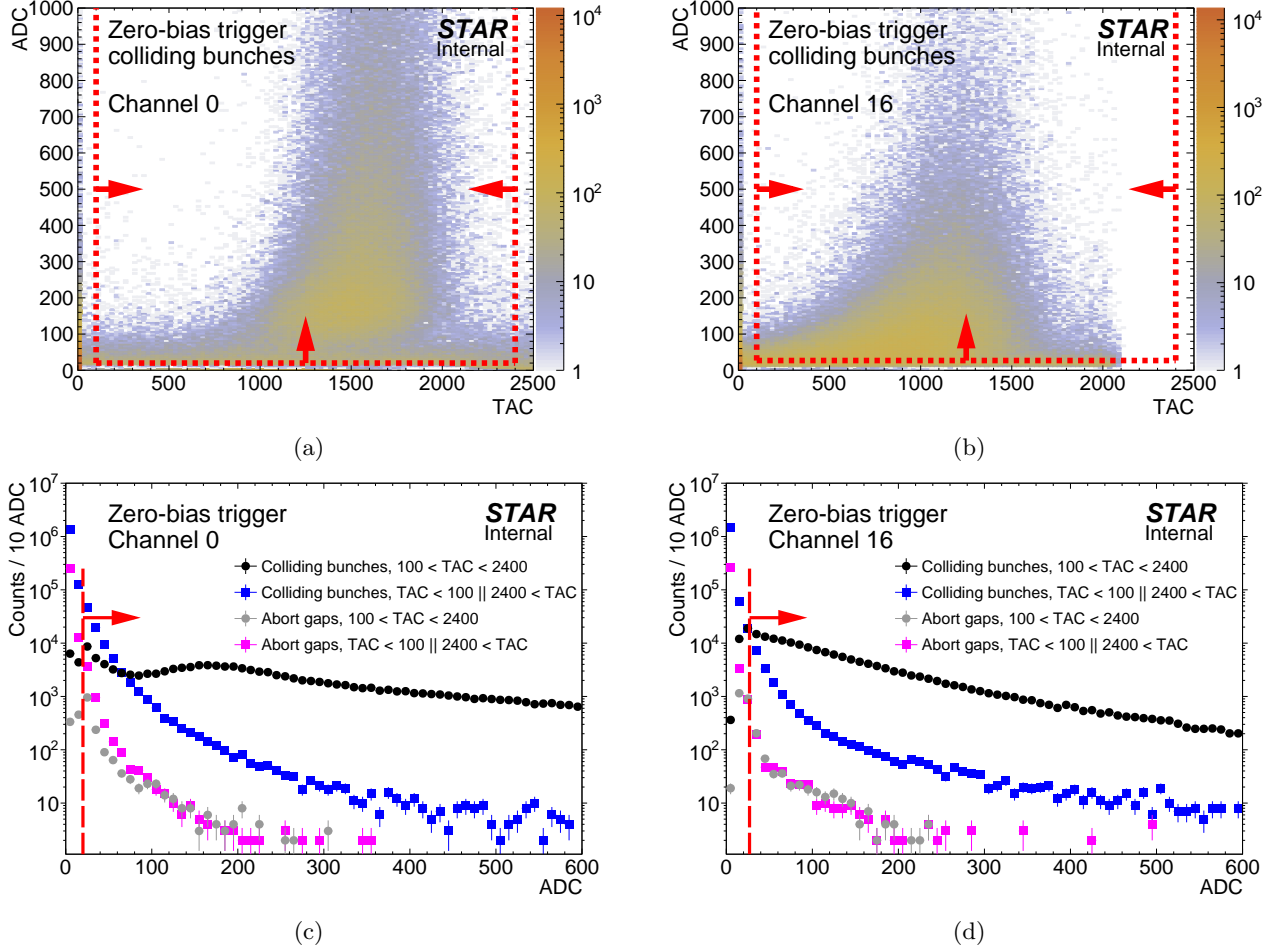


Figure 3.8: Sample BBC-small (left column) and BBC-large (right column) response in zero-bias data. Top row shows TAC vs. ADC distributions, bottom row shows projection of the corresponding two-dimensional distribution on x -axis (ADC) in the TAC range quoted in the legend, for both abort gaps and colliding bunches. Red lines and arrows indicate thresholds for a signal in presented channels.

Each channel of the BBC-large has different response to signal from ionizing particle, as well as different level of noise. We decided to set up a signal threshold for each channel based on a study of the noise in abort gaps (in zero-bias data). This noise, in principle, should be solely the electronics noise. We checked for each channel the probability to detect a signal with ADC above certain threshold and with TAC contained within 100 and 2400 (the same window is default for small BBC). The result is shown in Fig. 3.9. Next, we established final ADC thresholds in each BBC-large channel by requiring that the noise in BBC-large would cause a veto in maximally 3.5% of events. To transform it to ADC_{thr} we first assumed that the noise is uncorrelated between the channels. With this assumption one can connect the probability of the veto in whole BBC-large detector (east and west) caused by noise $\mathcal{P}_{\text{veto}}^{\text{noise}}$ with the probability of the signal induced by noise in single BBC-large channel $\mathcal{P}_{i,\text{sig}}^{\text{noise}}$:

$$\mathcal{P}_{\text{veto}}^{\text{noise}} = 1 - \mathcal{P}_{\text{veto}}^{\text{noise}} = 1 - (1 - \mathcal{P}_{i,\text{sig}}^{\text{noise}})^{N_{\text{ch}}^{\text{BBC}}}. \quad (3.3)$$

In the equation above $N_{\text{ch}}^{\text{BBC}}$ denotes number of active channels in BBC-large. From plots contained in Appendix A one can read that there were 14 active channels in BBC-large. 2 dead channels were found on the west side (40 and 42). By transforming Eq. 3.3 to the form presented below we can calculate the threshold probability for a single BBC-large channel:

$$\mathcal{P}_{i,\text{sig}}^{\text{noise}} = 1 - \sqrt[N_{\text{ch}}^{\text{BBC}}]{1 - \mathcal{P}_{\text{veto}}^{\text{noise}}} = 1 - \sqrt[14]{1 - 0.035} \approx 0.0025. \quad (3.4)$$

In the last step we translated this number to ADC threshold for each channel of BBC-large. For this purpose we used Fig. 3.9. The x -axis projection of the crossing point of each color line with the y -axis value of 0.0025 defines ADC_{thr} for each particular channel. These numbers are listed in Tab. 3.1. The event was dropped from analysis if any of the BBC-large channels registered signal of strength $\text{ADC}_i > \text{ADC}_{i,thr}$ and $100 < \text{TAC}_i < 2400$.

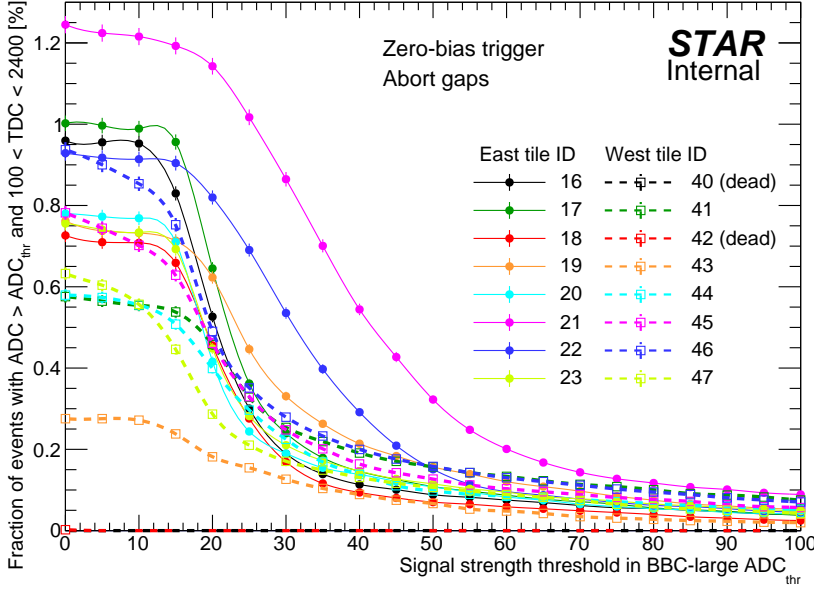


Figure 3.9: Percentage of events in abort gaps from zero-bias triggers with the ADC counts larger than the ADC threshold given in the x -axis, for each BBC-large channel. Measured points with statistical uncertainties are connected with a smooth line of corresponding color for better visualization.

Observation of high purification of CEP sample with described BBC-large veto in the data from run 15 was helpful to improve the CEP trigger for run 17. The improved trigger called RP_CPT2noBBCL was similar to RP_CPT2 with an addition of BBC-large veto using ADC threshold of 50.

3.2.6 (C7) TOF clusters limit

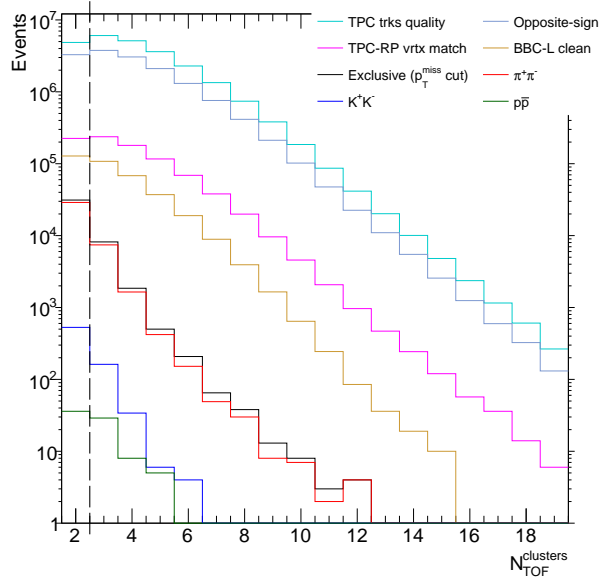


Figure 3.10: NTofClusters.

East		West	
i	ADC_{thr}	i	ADC_{thr}
16	27	40	0
17	30	41	31
18	26	42	0
19	37	43	14
20	25	44	29
21	55	45	30
22	43	46	33
23	27	47	22

Table 3.1: Offline ADC thresholds in BBC-large.

3.2.7 (C9) Exclusivity cut (missing p_T cut)

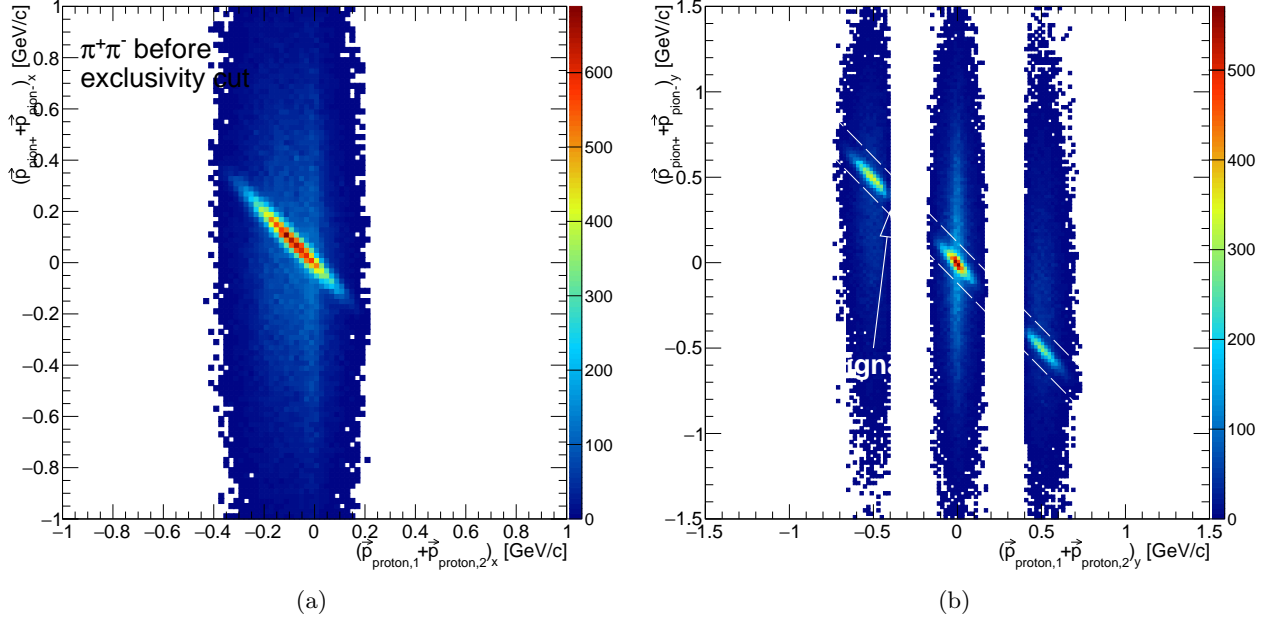


Figure 3.11: Correlation between sum of corresponding momentum components (x in Fig. 3.11a and y in Fig. 3.11b) of Roman Pot proton tracks and TPC tracks.

Tutaj dodac rysunki z suma 1D tych wielkosci i uzasadnic stosowanie ciecia na missing pT takimi samymi rozdzielczosciami w x i y

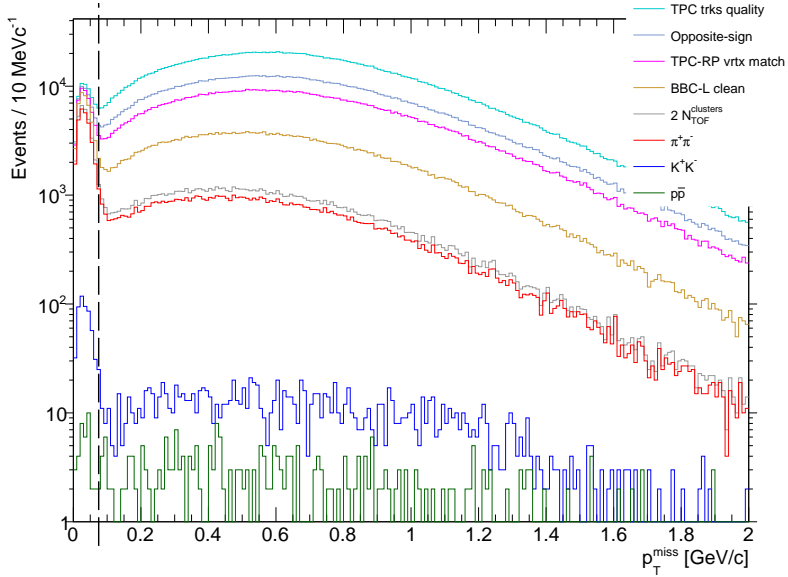


Figure 3.12: MissingPt.

3.2.8 (C8) Particle identification

In addition to information from the TPC we use time of hit detection in the barrel TOF subsystem.

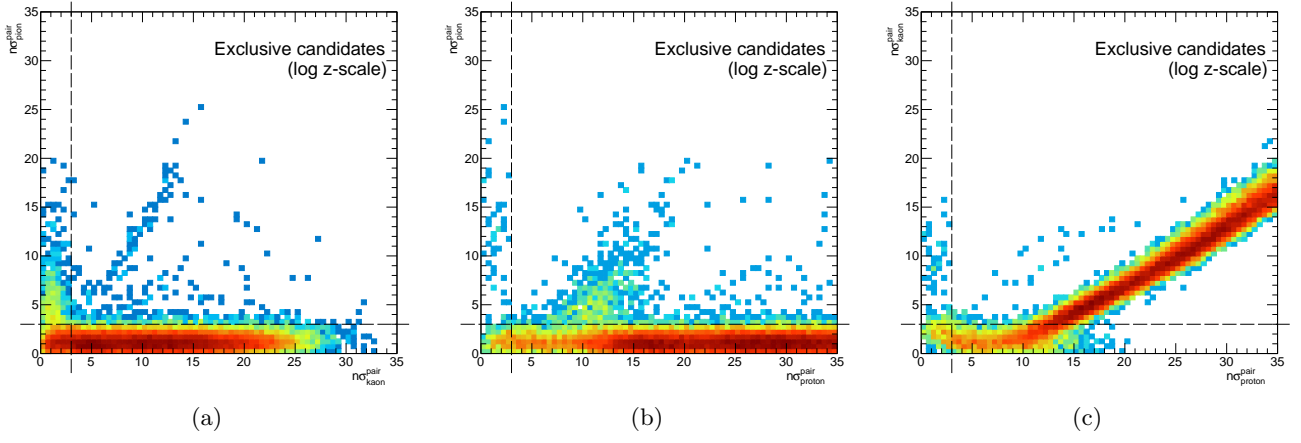


Figure 3.13: Correlation between $n\sigma^{\text{pair}}$ from TPC for $\pi^+\pi^-$, K^+K^- and $p\bar{p}$.

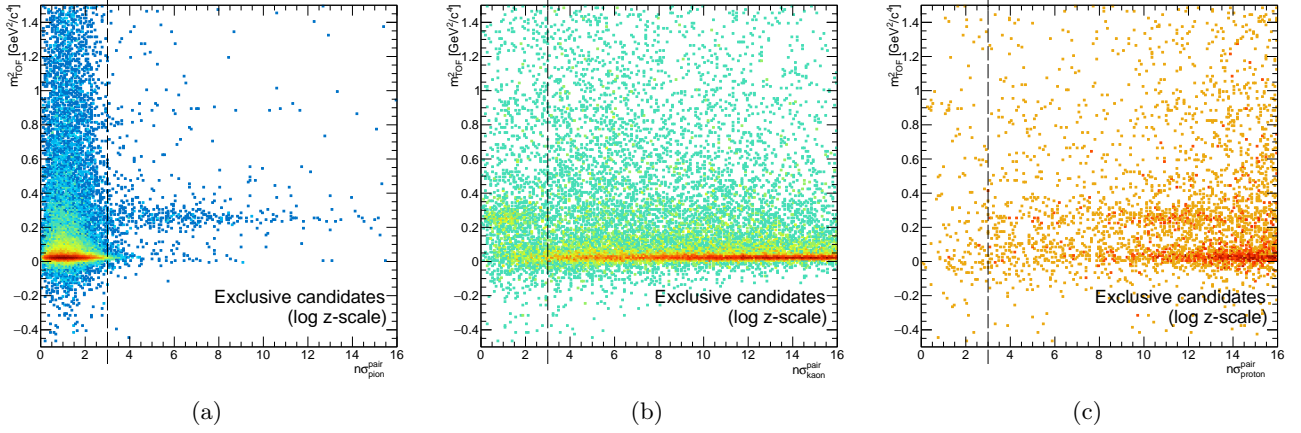


Figure 3.14: Correlation between m^2 from TOF and $n\sigma^{\text{pair}}$ from TPC for $\pi^+\pi^-$, K^+K^- and $p\bar{p}$.

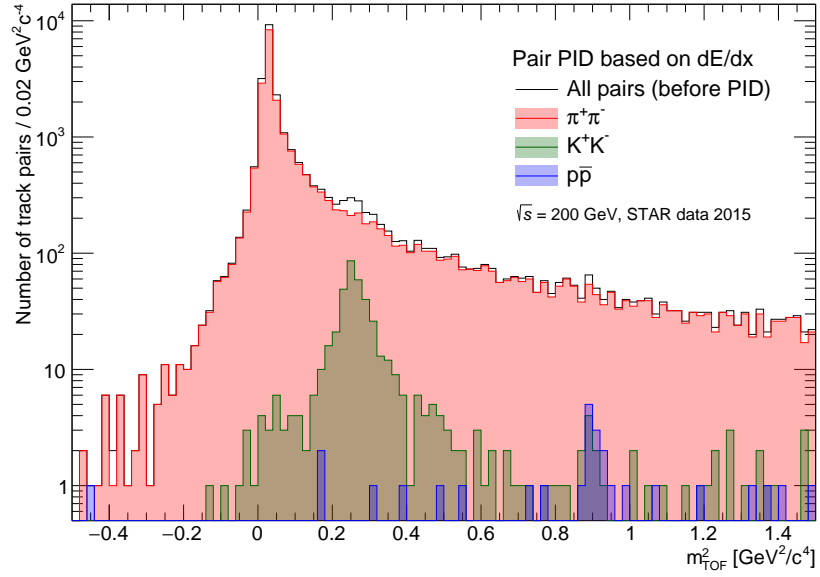


Figure 3.15: Squared particle mass from TOF for candidates of given PID selected based on dE/dx in TPC.

3.3 Signal per integrated luminosity

3.4 Cut flow

4. Corrections

4.1 Method of corrections application

$$\frac{d\sigma}{dq} = \frac{1}{\Delta q} \times \frac{1}{\varepsilon} \times \frac{N^w - N_{\text{bkgd}}^w}{L_{\text{int}}^{\text{eff}}} \quad (4.1)$$

$$L_{\text{int}}^{\text{eff}} = \sum_{\text{run}} L_{\text{int}}^{\text{run}} \times \epsilon_{\text{veto}}(L^{\text{run}}) \quad (4.2)$$

$$\varepsilon = \epsilon_{\text{ET/IT}} \times \epsilon_{\text{vrtx}}(q) \times \epsilon_{C2} \times \epsilon_{C5} \times \epsilon_{C9} \times \epsilon_{\text{PID}}(q) \quad (4.3)$$

$$N^w = \sum_{\text{event}} w_{\text{event}} \quad (4.4)$$

$$w = \left[\prod_{\text{sign}} \epsilon_{\text{TOF}}(\text{sign}, \text{PID}, p_T, z_{vx}, \eta) \times \prod_{\text{sign}} \epsilon_{\text{TPC}}(\text{sign}, \text{PID}, p_T, z_{vx}, \eta) \times \prod_{\text{side}} \epsilon_{\text{RP}}^{\text{side}}(p_x, p_y) \right]^{-1}, \quad (4.5)$$

$\text{sign} \in \{+, -\}, \quad \text{side} \in \{E, W\}$

4.2 Acceptances and efficiencies

In this section we present calculation of all efficiencies except TPC track reconstruction and TOF hit reconstruction and matching efficiency, which were discussed and presented in Ref. [1].

4.2.1 Trigger efficiency

4.2.1.1 Online veto (BBC-small and ZDC veto)

Vetoing signal in BBC-small and ZDC detectors on both sides of STAR was implemented in the logic of RP_CPT2 trigger. Common correction of the online and offline vetoes which is used in the correction procedure explained in Sec. 4.1 is presented in Sec. 4.2.2.3. However, to help quantify effect of just the online vetoes in BBC-small and ZDCs we show the Fig. 4.1 with the efficiency of the joint BBC-small and ZDC veto as a function of the instantaneous luminosity calculated from the zero-bias data. Details of the way the efficiency was calculated as well as description of the data in the Figure is the same as explained in Sec. 4.2.2.3.

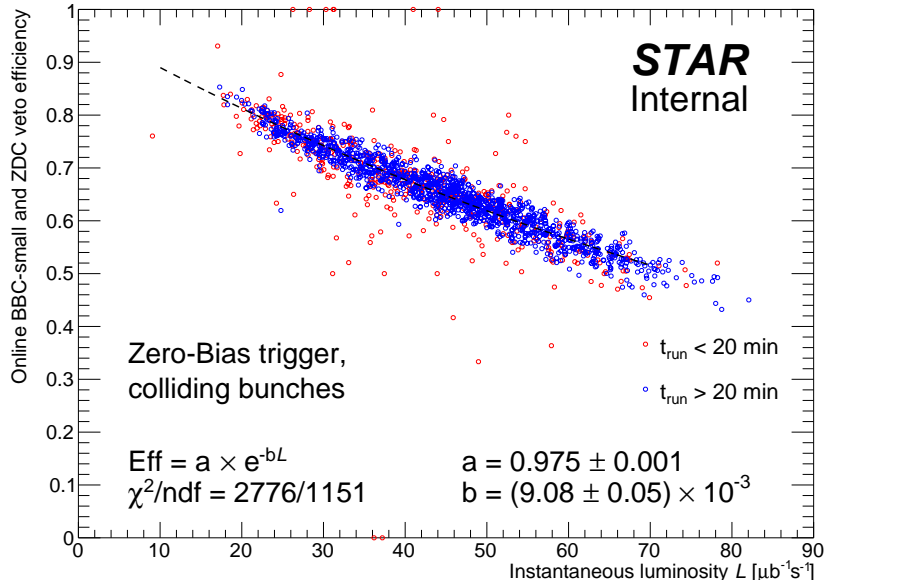


Figure 4.1: Overall efficiency of the online BBC-small and ZDC veto as a function of instantaneous luminosity.

4.2.1.2 RP triggering efficiency

Based on preliminary studies preformed during data taking using fast offline data (MuDst) we concluded that the RP triggering efficiency is very close to 100 % and eventual correction (which is going to be evaluated) is much smaller than overall systematic uncertainty. For the time being we assume that

$$\mathcal{E}(\text{TR}^E \wedge \text{TR}^W) = \mathcal{E}(\text{TR}^W) \times \mathcal{E}(\text{TR}^E) = 1. \quad (4.6)$$

4.2.1.3 Up and Down RP combination veto (due to dead material)

Probability that secondaries induced by proton with successfully reconstructed and selected RP track generate a trigger signal in the other RP branch on the same side was calculated using the embedded MC (see Sec. 6.3 in Ref. [1] for details of RP simulation in Geant4). Forward protons from CEP process provided by GenEx [20] were simultaneously generated from the interaction point spatially distributed the same as in the data. MC samples for all runs with RP_CPT2 triggers were produced to account for non-constant positions of the RP detectors throughout the run 15. Number of simulated events for each run was proportional to number of RP_CPT2 triggers in given run. The angular divergence of the beams was also simulated.

The discussed probability, $\mathcal{P}_{\text{DM veto}}^{\text{side}}$, was calculated as a probability that a MC-trigger signal is present in the branch on given side other than east and west branches where primary forward protons are expected from their initial momenta, under condition that these east and west branches detect a MC-trigger signal and there is no veto due to simultaneous ET&IT trigger bits in the overlayed data (no pile-up veto). By MC-trigger we understand the trigger signal reconstructed solely from the simulated data (not from the data embedded into).

Technically the $\mathcal{P}_{\text{DM veto}}^{\text{side}}$ was obtained in the following procedure:

1. No simultaneous ET&IT trigger bits were allowed in the data of an event that simulated signal was embedded into.
2. It was verified if there are MC-trigger signals in east and west branches that the primary forward protons were expected to reach based on their p_y ($p_y > 0$ - branch UP, $p_y < 0$ - branch DOWN). These events formed set *A*.
3. Events with the MC-trigger signal in RP branch other than the branch with MC-trigger signal expected from proton p_y on given side formed set *B*.
4. The probability was determined by the ratio of histograms from set *B* and set *A*:

$$\begin{aligned} \mathcal{P}_{\text{DM veto}}^{\text{side}}(p_x, p_y, z_{\text{vtx}}) &= \mathcal{E}^{\text{side}}(\text{Veto}^{\text{DM}} | \text{!Veto}^{\text{PU}} \wedge \text{TR}^E \wedge \text{TR}^W) = \\ &= \frac{(p_x, p_y, z_{\text{vtx}}) \text{ histogram for protons from set } B}{(p_x, p_y, z_{\text{vtx}}) \text{ histogram for protons from set } A} \end{aligned} \quad (4.7)$$

It should be noted that the momentum components (p_x, p_y) were taken from the proton with accounted effect of the beam divergence (after the original initial momentum smearing). Sample probability of a dead-material-induced veto is shown in Fig. 4.2, with all the remaining results contained in Appendix D.

The efficiency of the discussed veto which is finally used to correct the data is opposite of the veto probability, namely

$$\epsilon_{\text{DM veto}}^{\text{side}} = 1 - \mathcal{P}_{\text{DM veto}}^{\text{side}}. \quad (4.8)$$

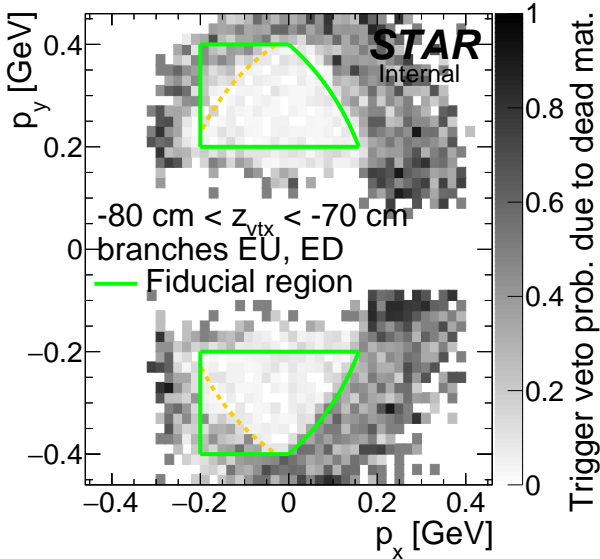


Figure 4.2: Sample probability of ET&IT trigger veto due to forward proton interaction with dead material. Results were obtained from forward proton MC simulation embedded into zero-bias data.

4.2.2 Selection efficiency

4.2.2.1 TPC z -vertex cut (C2)

Removing from analysis specific range of z -positions of primary vertices effectively reduces accepted luminosity with respect to that delivered by the collider. This loss of luminosity has to be accounted when calculating the cross sections, which is the goal of presented analysis. Assuming that the distribution of z_{vtx} of all primary interactions that take place when east and west beams overlap follows a normal distribution (\mathcal{N}), then the formula describing efficiency of the cut C2 has the following form:

$$\epsilon_{z_{\text{vtx}}} = \int_{z_{\text{vtx}}^{\min}}^{z_{\text{vtx}}^{\max}} \mathcal{N}(z_{\text{vtx}}; \mu, \sigma) dz_{\text{vtx}} = \frac{1}{2} \left[\text{Erf} \left(\frac{z_{\text{vtx}}^{\max} - \mu}{\sqrt{2}\sigma} \right) - \text{Erf} \left(\frac{z_{\text{vtx}}^{\min} - \mu}{\sqrt{2}\sigma} \right) \right], \quad (4.9)$$

where z_{vtx}^{\min} and z_{vtx}^{\max} are respectively minimum and maximum value of the longitudinal position of the vertex accepted in analysis (in our case these are -80 cm and 80 cm), and parameters μ and σ are respectively the mean and standard deviation of the normal distribution:

$$\mu = \langle z_{\text{vtx}} \rangle, \quad \sigma = \sigma(z_{\text{vtx}}).$$

Real parameters of z_{vtx} distribution were studied separately for every single fill of the collider. It is motivated by the fact that each fill of the machine is nearly independent from the previous thus the shape and position of z_{vtx} may vary on fill by fill basis. We neglect possible changes within the fill (e.g. widening of the distribution due to intrabeam scattering etc.) arguing that this effect if expected to be smaller than the systematic uncertainties related to determination of position and width of z_{vtx} distribution.

For every fill of RHIC the distribution of z_{vtx} of single TOF vertices was prepared, as shown in Fig. 4.3. This distribution was fitted with the Gaussian function in a range $z_{\text{vtx}} \in [-120 \text{ cm}, 120 \text{ cm}]$. The output parameters of all fits were plotted as a function of the fill number, as shown in Fig. 4.4. The efficiency used in the correction procedure was calculated independently for each fill using presented values of $\langle z_{\text{vtx}} \rangle$ and $\sigma(z_{\text{vtx}})$. Typical numerical value of this efficiency equals $\sim 88\%$.

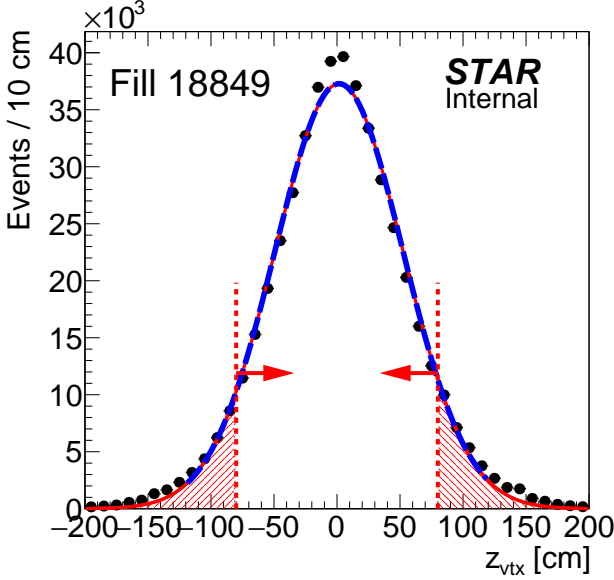


Figure 4.3: Sample distribution of z_{vtx} of single TOF vertices together with the fit of normal distribution (dashed blue) extended outside the range of the fit (solid red). Hashed red area represents part of the distribution rejected by cut C2 with the cut value marked with dashed red vertical lines and arrows.

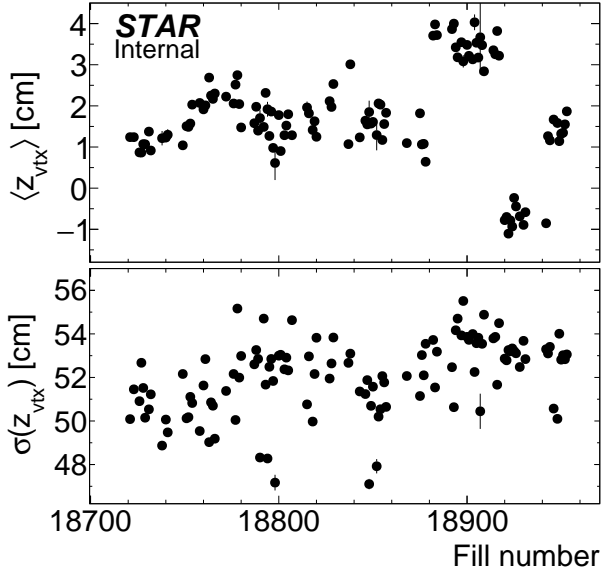


Figure 4.4: Mean (top panel) and width (bottom panel) parameters of the normal distribution obtained from a fit of normal distribution to z_{vtx} distribution in a range $[-120 \text{ cm}, 120 \text{ cm}]$ for each RHIC fill as a function of the fill number.

4.2.2.2 TPC-RP z -vertex matching (C5)

4.2.2.3 Primary vertices limit (C1), BBC-large veto (C6), TOF clusters limit (C7) and Up and Down RP combination veto (due to pile-up)

Combined efficiency of the online veto in BBC-small and ZDC (Sec. 4.2.1.1) and offline cuts (vetoes) on extra TPC-TOF vertices, extra TOF clusters, signal in BBC-large and simultaneous signal in Up and Down RPs, was calculated using the zero-bias data. For each run a fraction of events (for colliding bunches) was calculated in which all mentioned cuts would be satisfied in case of the CEP $\pi^+\pi^-/K^+K^-/p\bar{p}$ event (event would not be vetoed). One can transform this prescription to simple formula below:

$$\epsilon_{b_E b_W}^{\text{veto}} = \frac{\# \text{events in the run without TOF vertices, without signal in BBC-S, BBC-L, ZDC,}}{\# \text{RP branches other than } b_E, b_W, \text{ and with no more than 1 reconstructed TOF cluster}} \quad (4.10)$$

In Fig. 4.5 this efficiency is presented as a function instantaneous luminosity delivered by the machine, for each combination of east and west RP branches. Result for each combination is nearly identical as the effect of ET&IT trigger veto in RPs is not dominant, as well as trigger in all branches had similar acceptance. The data points were fitted with the exponential function (of the form contained in the figure) which reflects the fact that this efficiency should behave similar to the probability of lack of any interaction in the bunch crossing given by the Poisson distribution:

$$\text{Pois}(0; \mu) = \frac{\mu^0}{0!} \times e^{-\mu} = e^{-\mu}. \quad (4.11)$$

Comparison of the μ in Eq. (4.11) with the fit parameters in Fig. 4.5 leads to approximate determination of the average interaction probability per bunch crossing equal $0.2 - 0.9$. The result of the fit, $\epsilon_{b_E b_W}^{\text{veto}}(\mathcal{L})$, is finally used to correct measured data as described in Sec. 4.1.

Comparison of efficiencies in Fig. 4.5 with similar efficiency in Fig. 4.1 demonstrates that offline selection has much smaller impact on the loss of signal events than online selection. It has to be underlined that online vetoes were necessary to set trigger purity to satisfactory level, as well as reduce prescale of the trigger.

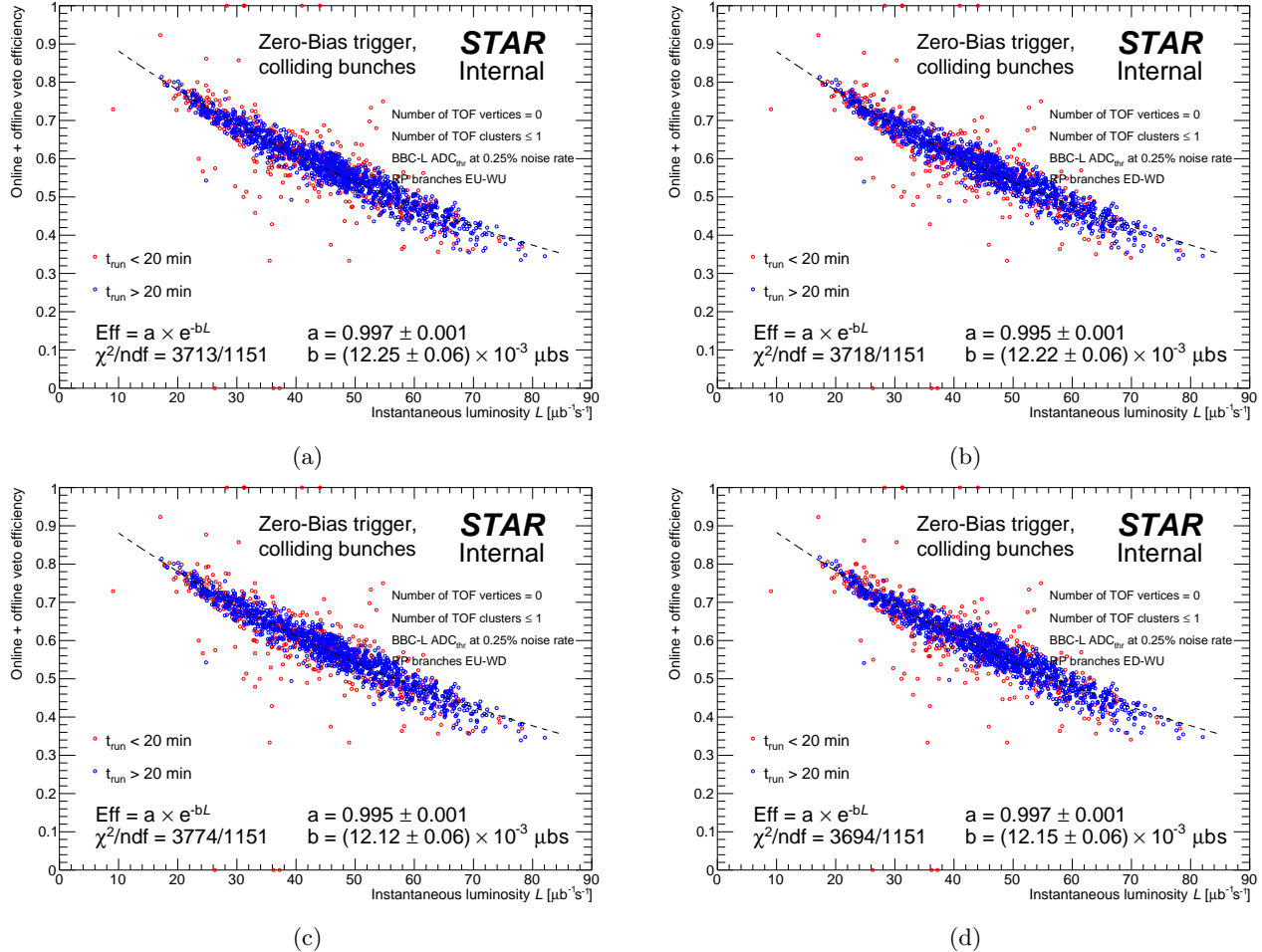


Figure 4.5: Overall efficiency of the online BBC-small, ZDC and ET&IT trigger veto, primary vertices limit (C1), BBC-large veto (C6) and TOF clusters limit (C7) as a function of instantaneous luminosity for all possible combinations of east and west RP branches. Red and blue points represent runs lasting for less and more than 20 minutes, respectively. Black dotted lines represent fits of exponential functions to blue points.

4.2.2.4 Missing p_T cut (C9)

4.2.2.5 Particle identification (C8)

Correction reflecting efficiency of identification requires good modeling of detector response in terms of dE/dx and TOF time (m^2) measurement which were used for this purpose as described in Sec. 3.2.8. In addition to this, significant number of simulated events is needed to reduce statistical uncertainties of efficiency. The former was provided by adjusting dE/dx spectra from embedded MC to match the data, as elaborated in Chap. 7 of Ref. [1]. The latter, however, was not easy to achieve for exclusive K^+K^- and $p\bar{p}$ whose identification is most challenging and information about identification efficiency is the most needed among studied species. Specially for study of particle (exclusive pair) identification a dedicated MC simulation was prepared.

This dedicated MC simulation was designed to work as follows (simulation of single CEP event of predefined pair ID is described):

1. The position of z_{vtx} was drawn from predefined distribution.
2. Kinematics of central state particles was set: momentum (magnitude) p , pseudorapidity η and azimuthal angle ϕ of positive and negative charge particles were drawn from predefined distributions.
3. Both particles were tested if doubled radius of curvature R of associated track in the magnetic field ($B = 0.5$ T) of the TPC ($R \propto p_T/B$) is smaller than the radius of TOF detector barrel (assumed 212 cm). If not then event was skipped and procedure was restarted (back to 1.).
4. The particles were propagated from the vertex at $(0, 0, z_{\text{vtx}})$ through the magnetic field of TPC using Newton's method with the time step (in the laboratory) equal 100 ps, corresponding to space step < 3 cm.

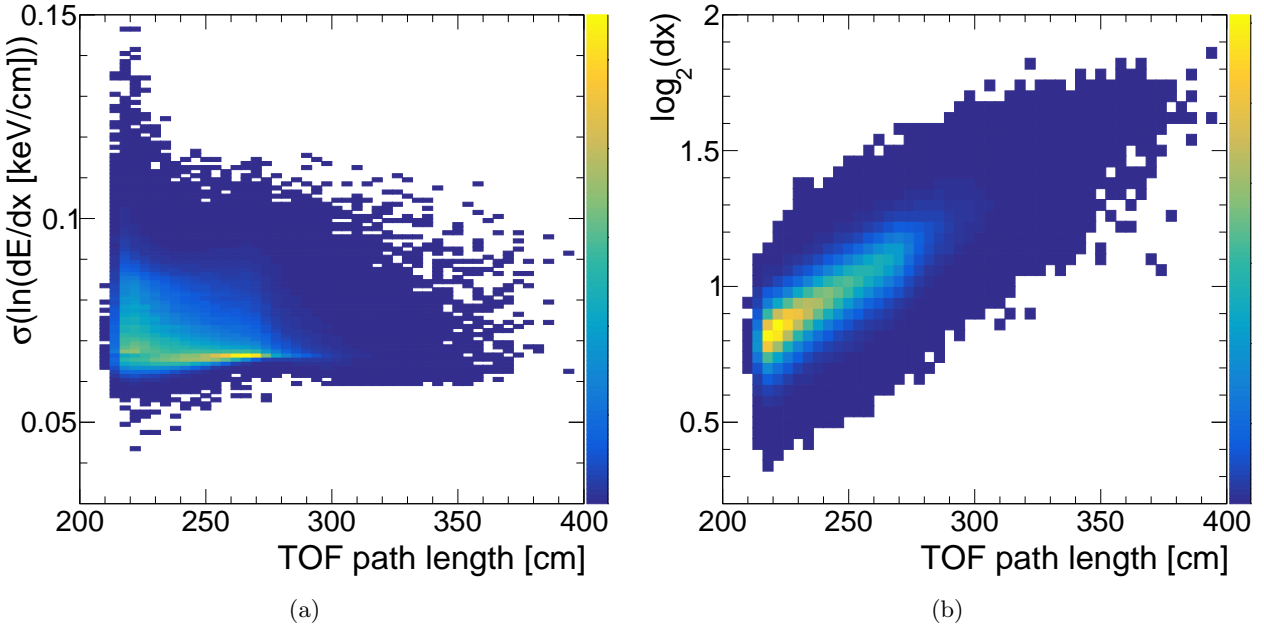


Figure 4.6: Correlation between uncertainty of the natural logarithm of $dE/dx/(1 \text{ keV}/\text{cm})$ and track TOF path length (4.6a) and correlation between base 2 logarithm of dx and track TOF path length (4.6b). The distributions were obtained for the exclusive event candidates after full selection, with all three types of particle pairs combined.

5. After step 4. the position of the TOF cell was known allowing to calculate the TOF path length L between the vertex and position of the TOF hit. Also the TOF hit time t was then known, further smeared by adding random number from normal distribution with mean at 0 and standard deviation $\sigma_{\text{TOF}} = 100 \text{ ps}$ to account for the finite TOF time resolution. In addition to this, reconstructed tracks' momenta were defined as the true momenta smeared by 3%, to account for finite TPC momentum resolution. At this stage it was possible to calculate m_{TOF}^2 using Eq. (C.8).
6. The dE/dx measurement was simulated. For each particle a dE/dx was drawn from the distribution of the form given by Eq. (7.6) and of parameters (for given particle ID and momentum) which were extracted from the data and tabulated in Tab. 7.1, all contained in Chap. 7 of Ref. [1]. This assured that the simulated dE/dx exactly matched the data. Once dE/dx for both particles (tracks) was obtained, value of the dE/dx error (more strictly: uncertainty of $\ln(dE/dx [\text{keV}/\text{cm}])$) and $\log_2(dx)$ was also set up. These quantities depend on the number of TPC hit points used in the reconstruction of dE/dx (the more hits in tracks, the better resolution of dE/dx and higher dx), which obviously is not accessible without full STAR simulation in Geant. This problem was solved by extracting dependence of $\sigma(\ln(dE/dx))$ and $\log_2(dx)$ on the TOF path length from the data (from CEP events, Fig. ??). Since the length of the TOF path is very strongly correlated with the number of hits forming the track and thus number of hits used to reconstruct dE/dx , one is allowed to draw $\sigma(\ln(dE/dx))$ and $\log_2(dx)$ from their distributions for particular TOF path lengths calculated in 5.. In this way the simulation preserves relevant connections between dE/dx -related quantities.

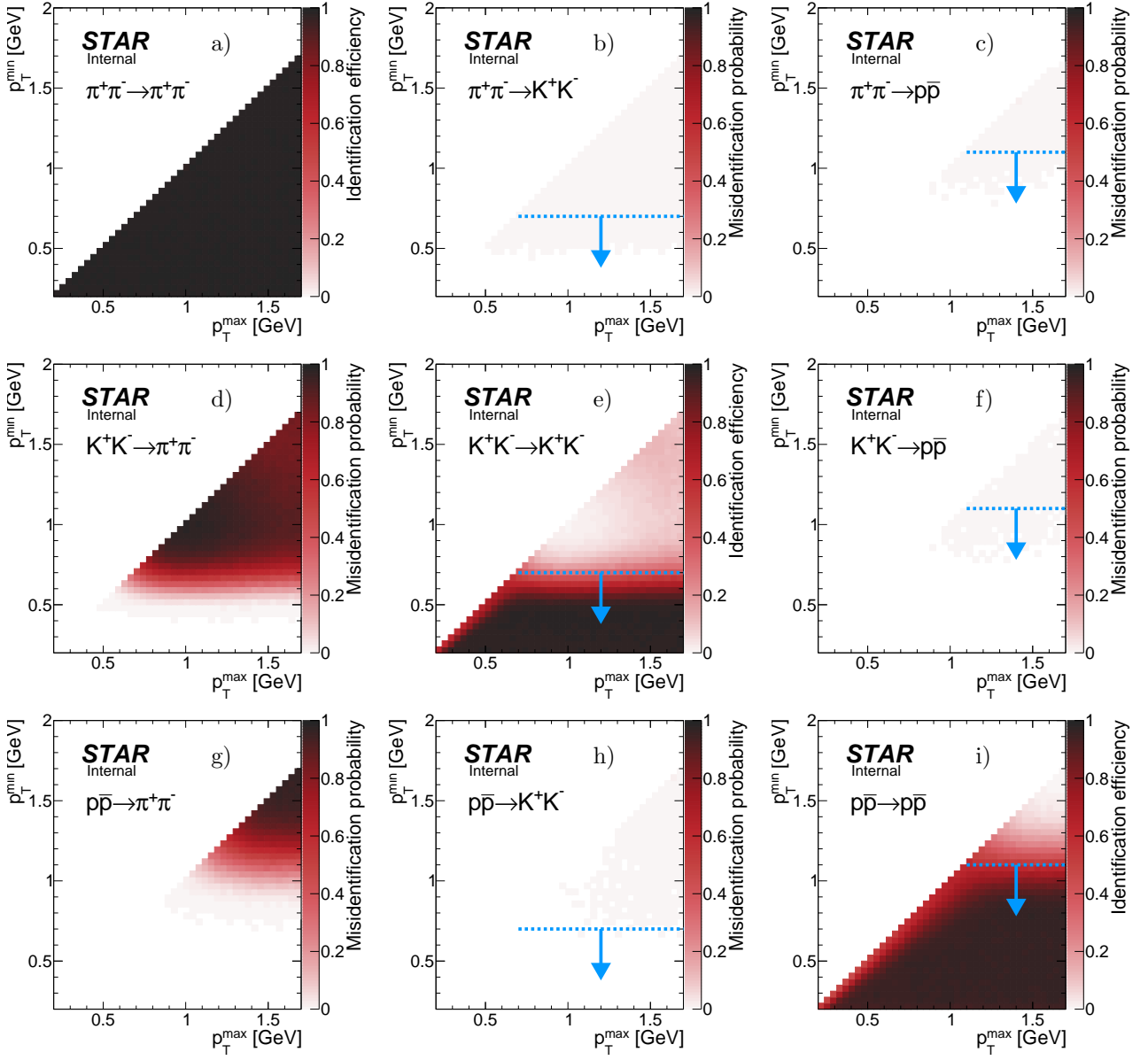


Figure 4.7: Pair identification efficiency (diagonal) and misidentification probability (off-diagonal) as a function of tracks' p_T for $\pi^+\pi^-$, K^+K^- and $p\bar{p}$ pairs. The results were obtained from the dedicated MC simulation described in the text. Blue lines and arrows mark the cut value on lower of the track p_T 's for kaons and protons.

4.2.3 RP track acceptance and reconstruction efficiency

To calculate RP acceptance and track reconstruction efficiency the embedded MC technique was used. The same sample was used as that described in Sec. 4.2.1.3, used for calculation of the dead-material related trigger veto.

The joint RP acceptance and track reconstruction efficiency for a given STAR side, $\epsilon_{RP}^{\text{side}}$, was calculated as a probability that a single good quality RP track (satisfying cuts C4.1-C4.2) matched with true-level primary forward proton is reconstructed on given side in the branch expected based on sign of p_y of the proton, under condition that there is a trigger signal in that branch and there is no trigger signal in the other branch on the same side.

Technically the $\epsilon_{RP}^{\text{side}}$ was obtained in the following procedure:

1. It was verified if there is a trigger signal in the branch that the primary forward proton is expected to reach based on its p_y ($p_y > 0$ - branch UP, $p_y < 0$ - branch DOWN). Additionally required lack of trigger signal in the other branch on the same side. These events formed set *A*.
2. The nominal RP track selection algorithm was used to find a single good quality track (cuts C4.1-C4.2) on given side. If exactly one such track was found, it was additionally checked if it is matched with true-level

primary proton. These events formed *set B*.

3. The efficiency was determined by the ratio of histograms from *set B* and *set A*:

$$\epsilon_{\text{RP}}^{\text{side}}(p_x, p_y, z_{\text{vtx}}) = \mathcal{E} \left(\text{RP}^{\text{side}} \mid \text{TR}^{\text{side}} \wedge !\text{TR}^{\text{side}} \right) = \frac{(p_x, p_y, z_{\text{vtx}}) \text{ histogram for protons from set } B}{(p_x, p_y, z_{\text{vtx}}) \text{ histogram for protons from set } A} \quad (4.12)$$

It should be noted that the momentum components (p_x, p_y) were taken from the proton with accounted effect of the beam divergence (after the original initial momentum smearing).

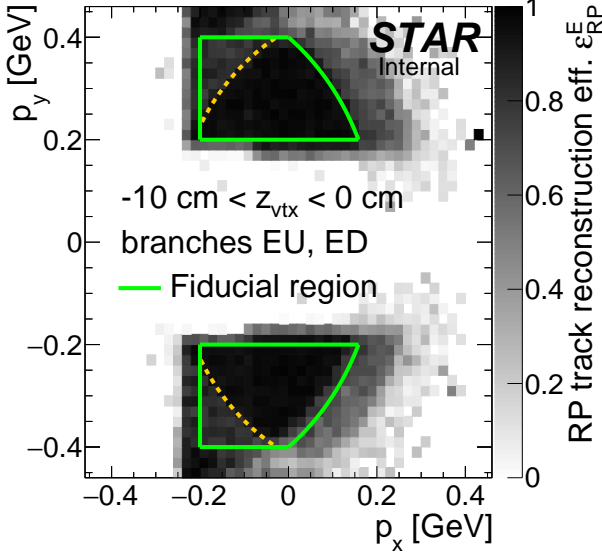


Figure 4.8: Sample RP track reconstruction efficiency in a single z -vertex bin on the east STAR side. The efficiency was calculated using forward proton MC simulation embedded into zero-bias data. Green envelopes mark the fiducial region of the measurement, while dashed yellow lines mark the part of the fiducial region with a data-driven efficiency correction needed, as explained in Sec. 10.3.1 of Ref. [1].

The efficiency calculated in the way described above is, by design, the acceptance, reconstruction and selection efficiency for a single proton on one side of the IP. In CEP event there are two independent forward protons which may be simultaneously not reconstructed or rejected by the selection algorithm due to e.g. elastic pile-up interaction providing additional good quality proton tracks on both sides of IP. One could, in principle, calculate 5-dimensional efficiency for both forward protons (in variables $p_x^E, p_y^E, p_x^W, p_y^W$ and z_{vtx}) which would ultimately account for the simultaneous east and west inefficiency, however this would require orders of magnitude larger statistics of MC to provide reasonably low statistical uncertainty of the efficiency. Instead, on top of the 3-dimensional reconstruction and selection efficiencies for east and west RPs we calculate (from embedded MC) probability that the proton tracks are simultaneously not reconstructed or selected on the east and west side, despite the trigger signal solely in expected RP branches (no trigger veto) and true-level (p_x, p_y) of both forward protons contained in the fiducial region. This probability, denoted as

$$\mathcal{P}_{\text{loss}}^{\text{E\&W}} = \mathcal{E} \left(!\text{RP}^E \wedge !\text{RP}^W \mid \text{TR}^E \wedge \text{TR}^W \wedge !\text{Veto} \right), \quad (4.13)$$

is presented in Fig. 4.9 for all four combinations of east and west RP branches.

4.2.4 TPC vertex reconstruction efficiency

The definition of vertex reconstruction efficiency (ϵ_{vtx}) established in this analysis is the probability that two global tracks, both associated with true-level primary particles from the kinematic region of the measurement, both satisfying kinematic and quality criteria (cuts C3.3 and C3.4) and both matched with hits in TOF, form a

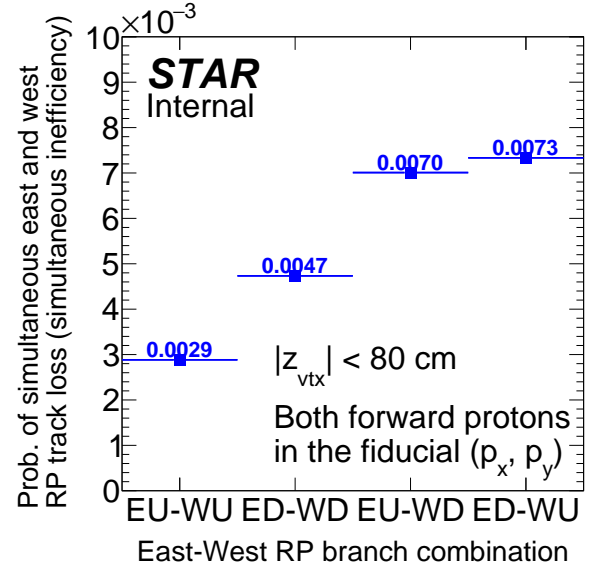
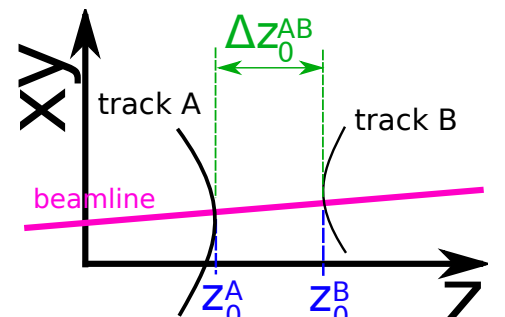


Figure 4.9: Probability of simultaneous inefficiency of the RP track reconstruction calculated from the CEP MC embedded into zero-bias data.



vertex listed in the collection of reconstructed primary vertices and DCA(R) and DCA(z) of both global tracks calculated w.r.t. this vertex is contained within the limits of cut C3.5.

We calculated this efficiency as a function of the longitudinal separation between two tracks (global helices) Δz_0 . Illustration of this quantity is given in Fig. 4.10. We consider this a natural quantity to present the vertexing efficiency - the closer to each other the helices are on the beamline, the more probable it is that two tracks will form a common primary vertex. It is in accordance with the way the vertexing algorithm works.

The vertexing efficiency was calculated from the data in the following way:

1. Data from RP_CPT2 trigger were used. Events were selected with nearly the same cuts as in nominal CEP analysis (Sec. 3.1). The requirement of exactly one primary vertex with exactly two primary TOF tracks was dropped. Instead, analysis utilized only global TOF tracks - exactly two global TOF tracks were required (cut C3.1 without primary track requirement), passing also cuts C3.2-C3.4. In this case the position of the vertex was reconstructed as

$$z_{\text{vtx}} = \frac{z_0^+ + z_0^-}{2}, \quad (4.14)$$

where z_0^+ and z_0^- are longitudinal impact parameters (z -coordinates of points of closest approach to the beamline) of positive and negative charge particle tracks, respectively. The vertex position was normally required to satisfy cut C2. Events after full selection, classified as exclusive $\pi^+\pi^-$ candidates, formed *set A*.

2. The two global TOF tracks were checked if they have associated primary tracks, and the two primary tracks are assigned to the same primary vertex. If yes, the tracks were additionally subjected to cut C3.5. Events passing described selection formed *set B*.
3. The efficiency was determined by the ratio of histograms from *set B* and *set A*:

$$\epsilon_{\text{vtx}}(|\Delta z_0|) = \frac{|\Delta z_0| \text{ histogram for events from set } B}{|\Delta z_0| \text{ histogram for events from set } A}. \quad (4.15)$$

Distribution of $|\Delta z_0|$ between two CEP global track candidates after full selection (*setA*) is presented in Fig. 4.11. The vertexing efficiency obtained with described method is shown in Fig. 4.12. Solid green points represent efficiency calculated with the non-exclusive background preserved, while open black points represent efficiency with this background subtracted (using method described in Sec. 4.4). Since the vertexing efficiency does not depend on the physics process and background is purely of physics origin the black and green points should overlap. Such picture emerges from presented comparison. We have calculated the same efficiency using CEP MC embedded into zero-bias data, the result is shown in Fig. 4.12 with red points. There is very good agreement between vertexing efficiency in the data and embedded MC for $|\Delta z_0| < 1$ cm, where most ($\sim 80\%$) of the signal is present. The differences in high- $|\Delta z_0|$ tail are understood as a result of the imperfect description of the pointing resolution (here: the transverse resolution) of TPC tracks in STARsim. Although the pointing resolution is adjusted to gain more accurate description of the data by MC simulation as described in Chapter 8 of Ref. [1], this does not help with the vertexing which is performed at the level of raw data (MC) processing to MuDst. Another reason could be different p_T (thus also d_0) spectrum of CEP tracks in the data and MC (GenEx).

Based on the width of $|\Delta z_0|$ distribution, the background content as a function of $|\Delta z_0|$, and the value of ϵ_{vtx} as a function of $|\Delta z_0|$, we decided to accept in analysis only tracks which satisfy $|\Delta z_0| < 2$ cm. This assures that the vertexing efficiency does not drop below $\approx 30\%$, as well as it coincides with the primary tracks requirement of $|\text{DCA}(z)| < 1$ cm. In the correction procedure we nominally use the vertexing efficiency represented by open black points in Fig. 4.12 (to correct the MC e.g. in closure tests we use red points instead). The additional correction factor connected with the cut on maximum $|\Delta z_0|$ (2 cm) was calculated from the data and equals 2.4% (Fig. 4.11). This correction is used as an additional normalization correction factor, which is different from $\epsilon_{\text{vtx}}(|\Delta z_0|)$ applied in form of a weight to each selected CEP event.

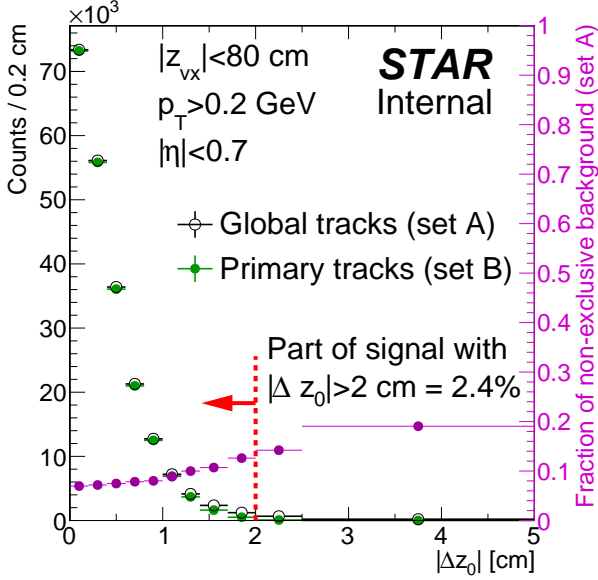


Figure 4.11: Distribution of Δz_0 between two CEP-candidate global tracks (green and black points) together with fraction of non-exclusive background in black distribution as a function of Δz_0 (violet points).

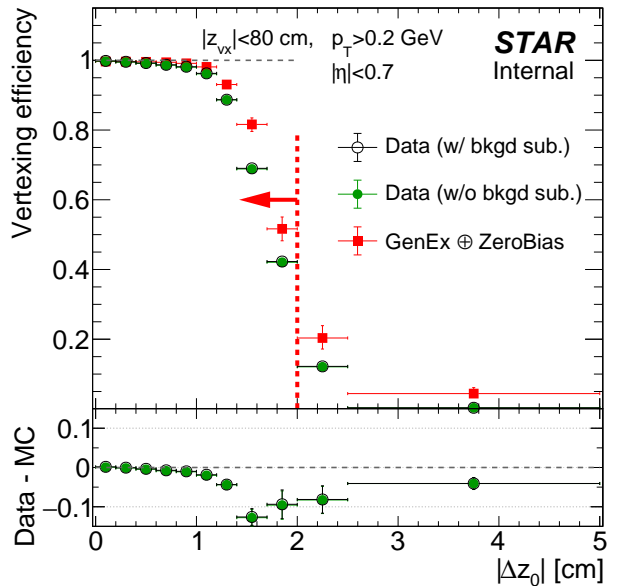


Figure 4.12: Vertexing efficiency calculated from the data (open black and full green points) and from embedded MC (red points) as a function of Δz_0 between two CEP-candidate global tracks.

4.3 Particle energy loss

Energy loss correction as a function of reconstructed particle p_T in bins of z -position of reconstructed vertex has been calculated and presented in Chapter 5 of Ref. [1] for all analyzed particle species and both positive and negative charges. The correction was applied independently for each particle in the following procedure:

1. After central particles were identified (cut C8) an absolute value of the particle transverse momentum correction ($-\Delta p_T = p_T^{\text{meas}} - p_T^{\text{true}}$) was read from the histogram corresponding to reconstructed z_{vtx} and to assigned particle ID (Appendix C of Ref. [1]).
2. The momentum correction factor f_p^{corr} was calculated:

$$f_p^{\text{corr}} = \frac{p_T^{\text{meas}} + \Delta p_T}{p_T^{\text{meas}}}. \quad (4.16)$$

3. New, corrected momentum \vec{p}^{corr} was assigned to the particle:

$$\vec{p}^{\text{corr}} = f_p^{\text{corr}} \cdot \vec{p}^{\text{meas}}. \quad (4.17)$$

In this way all three components of particle momentum are corrected so that the pseudorapidity of a particle remains unchanged.

This new momentum was further used in determination of total transverse momentum of all reconstructed particles, p_T^{miss} , as well as in applying TPC and TOF efficiency corrections and preparing histograms (cross sections) of physics quantities (e.g. invariant mass, rapidity of a pair of central tracks).

4.4 Background subtraction

5. Backgrounds

5.1 Sources of background

5.1.1 Non-exclusive background

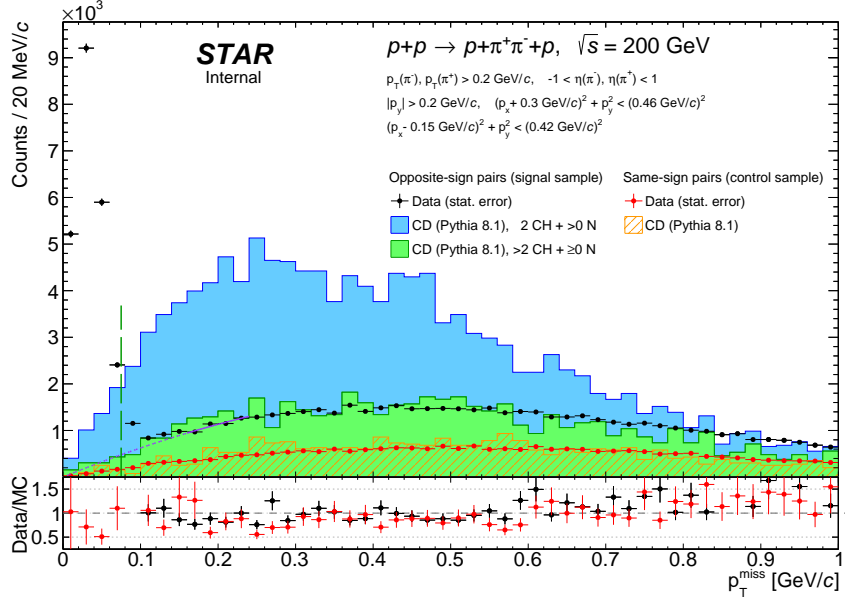


Figure 5.1: Missing pT.

tutaj dodac szkice spodziewanego tla nieekskluzywnego

5.1.2 Exclusive background (particle misidentification)

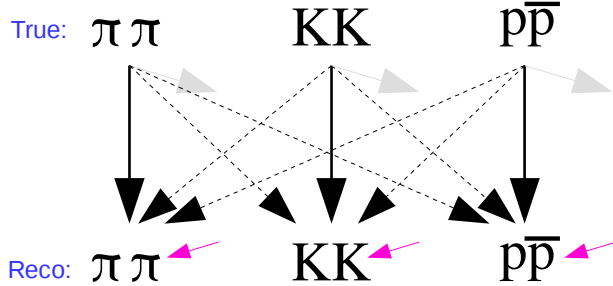


Figure 5.2: Graph illustrating the misidentification problem - the origin of exclusive background in selected samples. Gray arrows represent event rejection due to failed PID selection (C8). Magenta arrows indicate non-exclusive backgrounds described in Sec. 5.1.1. Solid black arrows represent successful identification, whereas dashed black lines show misidentification paths.

$$N_R^{\pi\pi} = \underbrace{\epsilon^{\pi\pi} \cdot N_T^{\pi\pi}}_{\text{true pion pairs}} + \underbrace{\lambda^{KK \rightarrow \pi\pi} \cdot N_T^{KK}}_{\text{kaon pairs reconstructed as pion pairs}} + \underbrace{\lambda^{p\bar{p} \rightarrow \pi\pi} \cdot N_T^{p\bar{p}}}_{\text{proton pairs reconstructed as pion pairs}} + N_{bkgd}^{\pi\pi} \quad (5.1a)$$

$$N_R^{KK} = \underbrace{\lambda^{\pi\pi \rightarrow KK} \cdot N_T^{\pi\pi}}_{\text{pion pairs reconstructed as kaon pairs}} + \underbrace{\epsilon^{KK} \cdot N_T^{KK}}_{\text{true kaon pairs}} + \underbrace{\lambda^{p\bar{p} \rightarrow KK} \cdot N_T^{p\bar{p}}}_{\text{proton pairs reconstructed as kaon pairs}} + N_{bkgd}^{KK} \quad (5.1b)$$

$$N_R^{p\bar{p}} = \underbrace{\lambda^{\pi\pi \rightarrow p\bar{p}} \cdot N_T^{\pi\pi}}_{\text{pion pairs reconstructed as proton pairs}} + \underbrace{\lambda^{KK \rightarrow p\bar{p}} \cdot N_T^{KK}}_{\text{kaon pairs reconstructed as proton pairs}} + \underbrace{\epsilon^{p\bar{p}} \cdot N_T^{p\bar{p}}}_{\text{true proton pairs}} + N_{bkgd}^{p\bar{p}} \quad (5.1c)$$

Eqs. (5.1) can be written in the matrix form, as shown in Eq. (5.2), from which it is straightforward to obtain final formula for unfolded number of events of given ID, Eq. (5.3):

$$\begin{bmatrix} N_R^{\pi\pi} - \textcolor{magenta}{N}_{bkgd}^{\pi\pi} \\ N_R^{KK} - \textcolor{magenta}{N}_{bkgd}^{KK} \\ N_R^{p\bar{p}} - \textcolor{magenta}{N}_{bkgd}^{p\bar{p}} \end{bmatrix} = \underbrace{\begin{bmatrix} \epsilon^{\pi\pi} & \lambda^{KK \rightarrow \pi\pi} & \lambda^{p\bar{p} \rightarrow \pi\pi} \\ \lambda^{\pi\pi \rightarrow KK} & \epsilon^{KK} & \lambda^{p\bar{p} \rightarrow KK} \\ \lambda^{\pi\pi \rightarrow p\bar{p}} & \lambda^{KK \rightarrow p\bar{p}} & \epsilon^{p\bar{p}} \end{bmatrix}}_{\text{"mixing matrix" } \Lambda} \begin{bmatrix} N_T^{\pi\pi} \\ N_T^{KK} \\ N_T^{p\bar{p}} \end{bmatrix} \rightarrow \begin{bmatrix} N_T^{\pi\pi} \\ N_T^{KK} \\ N_T^{p\bar{p}} \end{bmatrix} = \Lambda^{-1} \begin{bmatrix} N_R^{\pi\pi} - \textcolor{magenta}{N}_{bkgd}^{\pi\pi} \\ N_R^{KK} - \textcolor{magenta}{N}_{bkgd}^{KK} \\ N_R^{p\bar{p}} - \textcolor{magenta}{N}_{bkgd}^{p\bar{p}} \end{bmatrix} \quad (5.2)$$

5.2 Relative normalization of background and signal

6. Systematic errors

7. Physics results

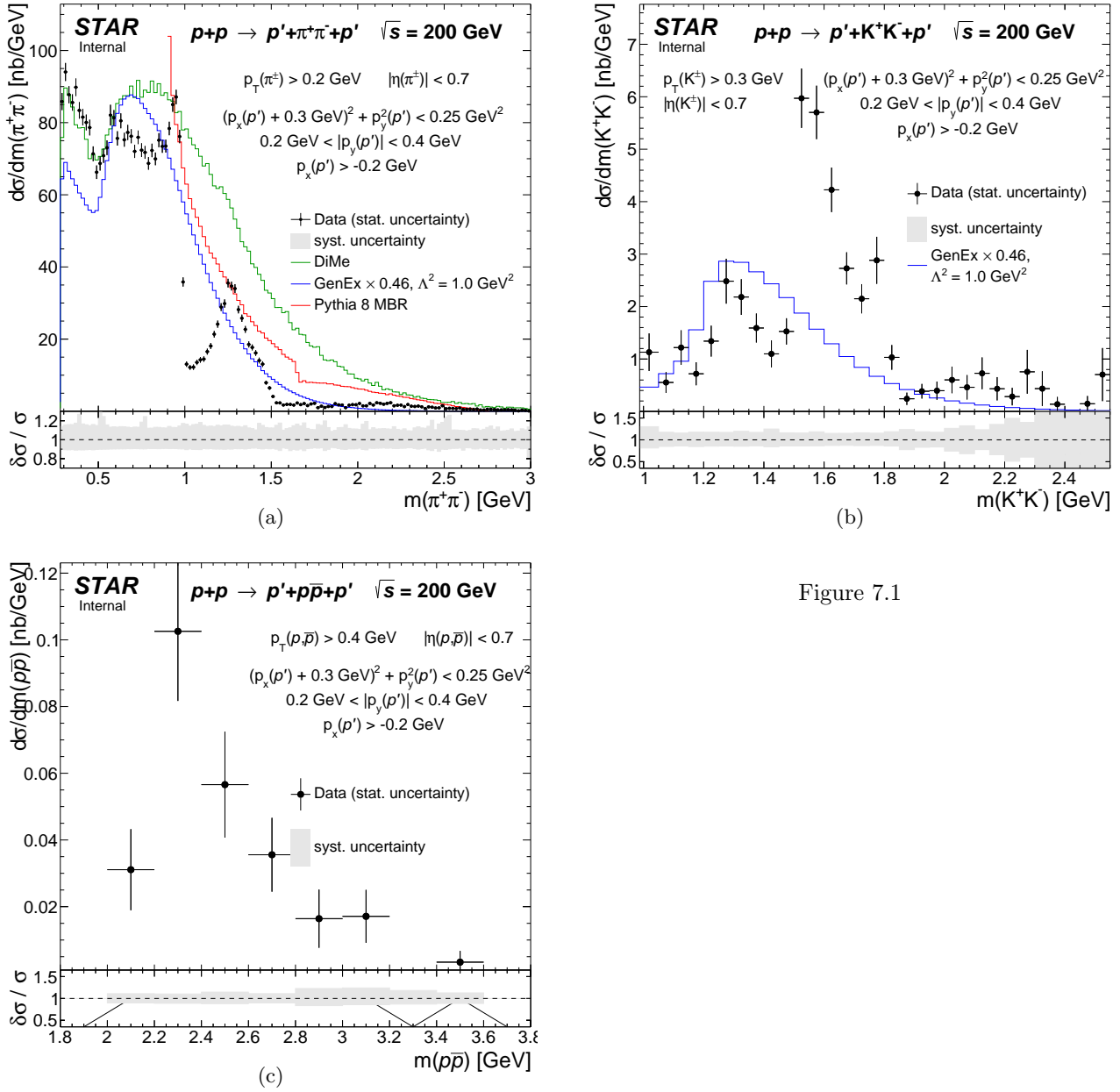


Figure 7.1

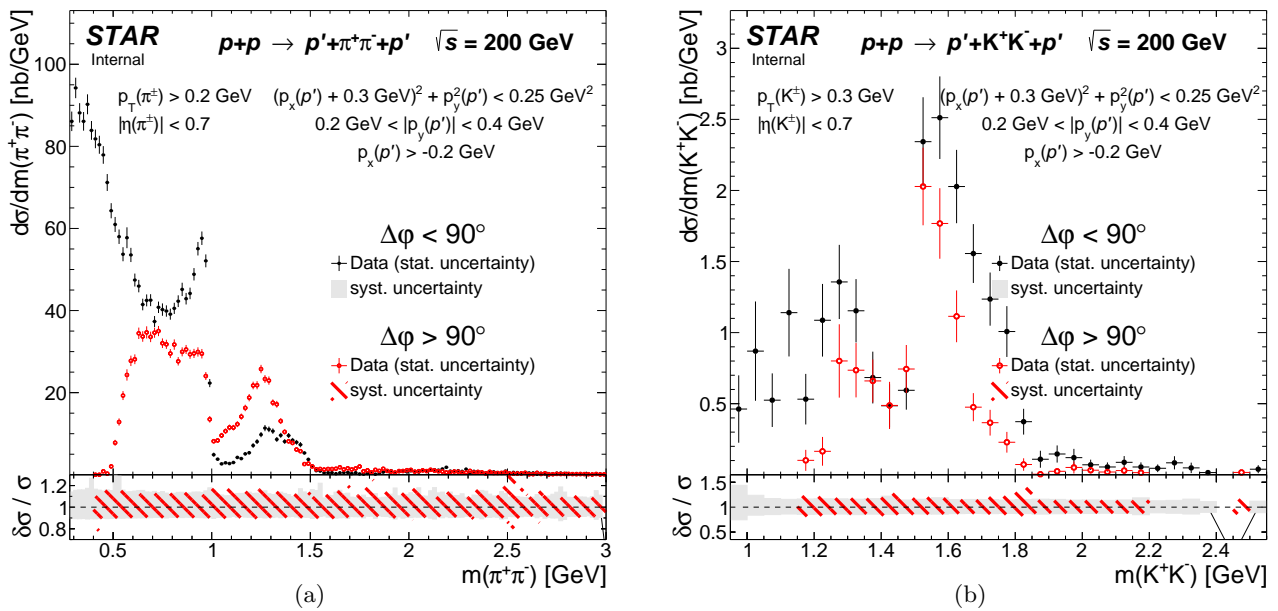


Figure 7.2

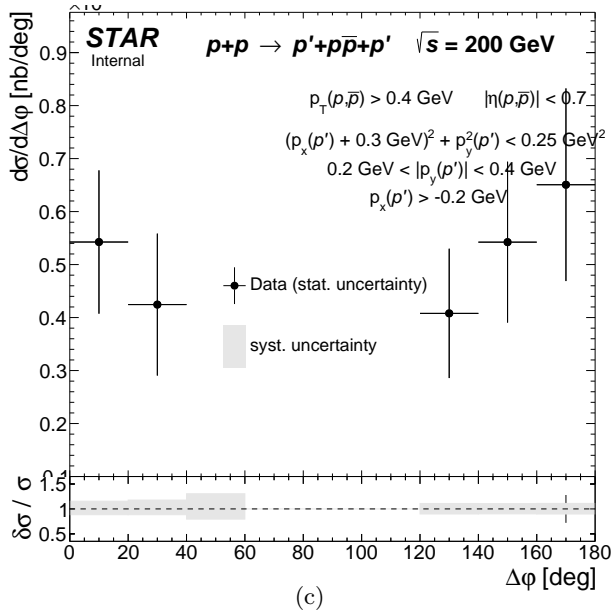
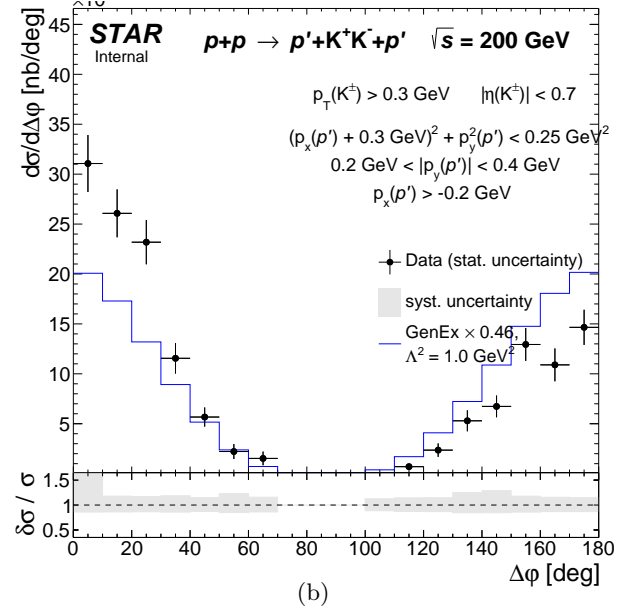
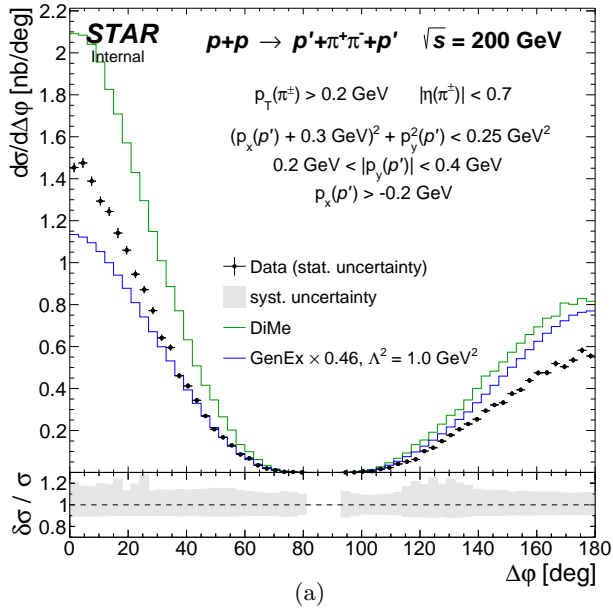


Figure 7.3

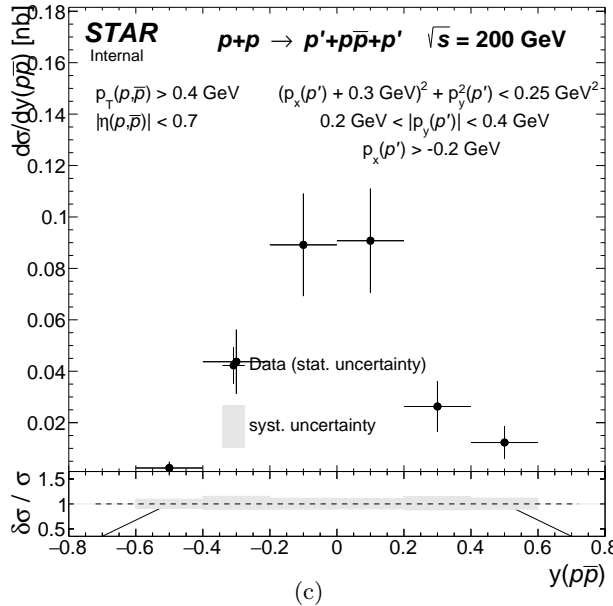
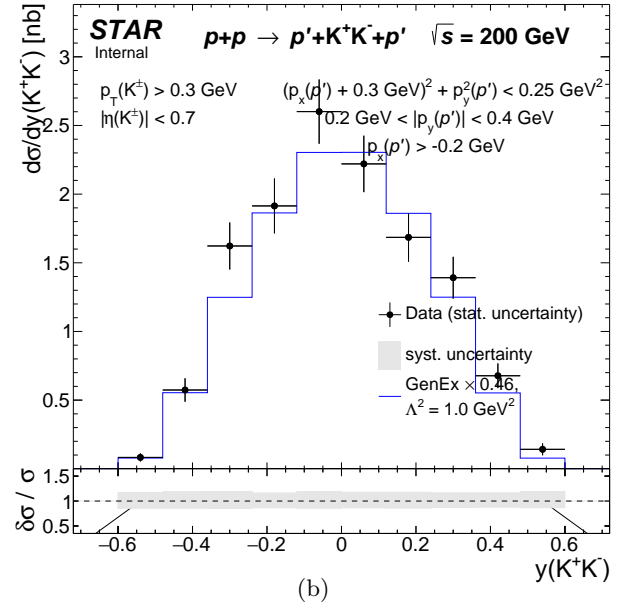
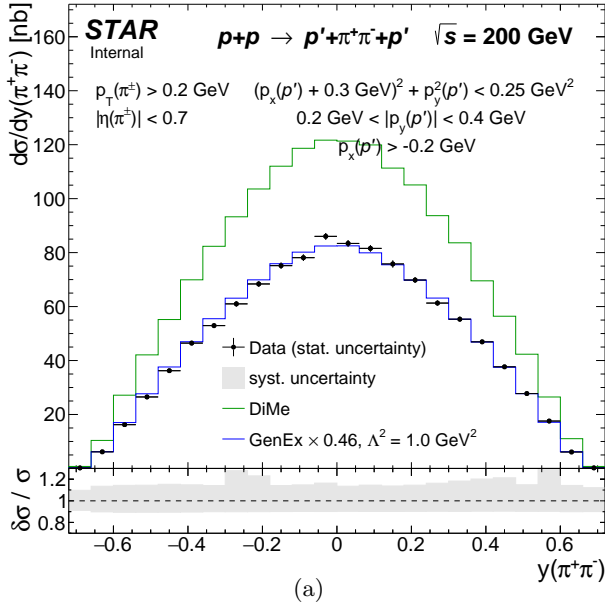


Figure 7.4

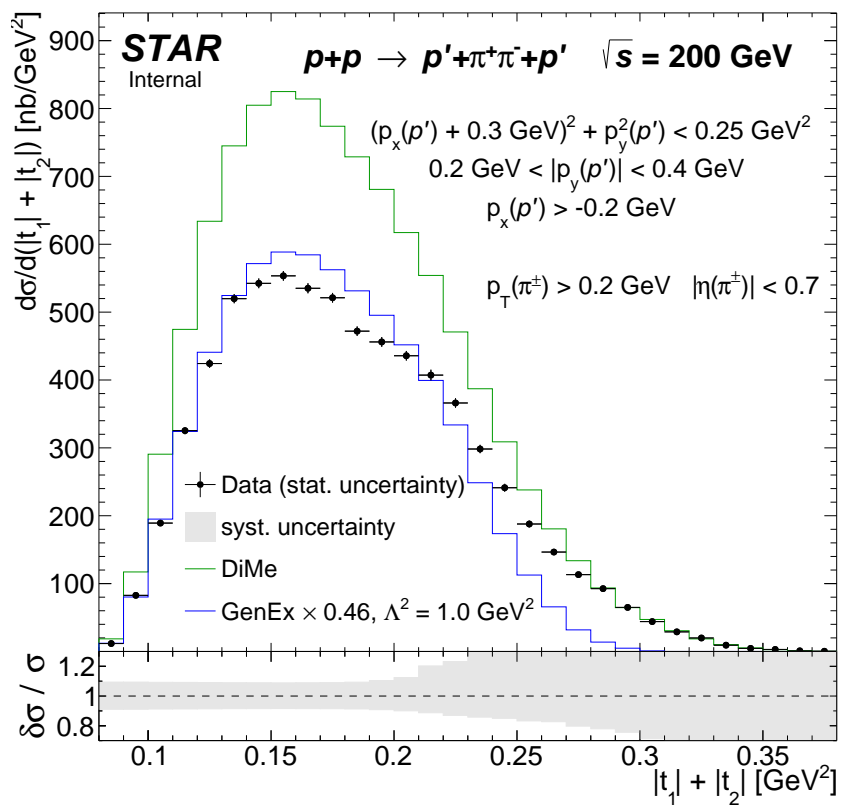
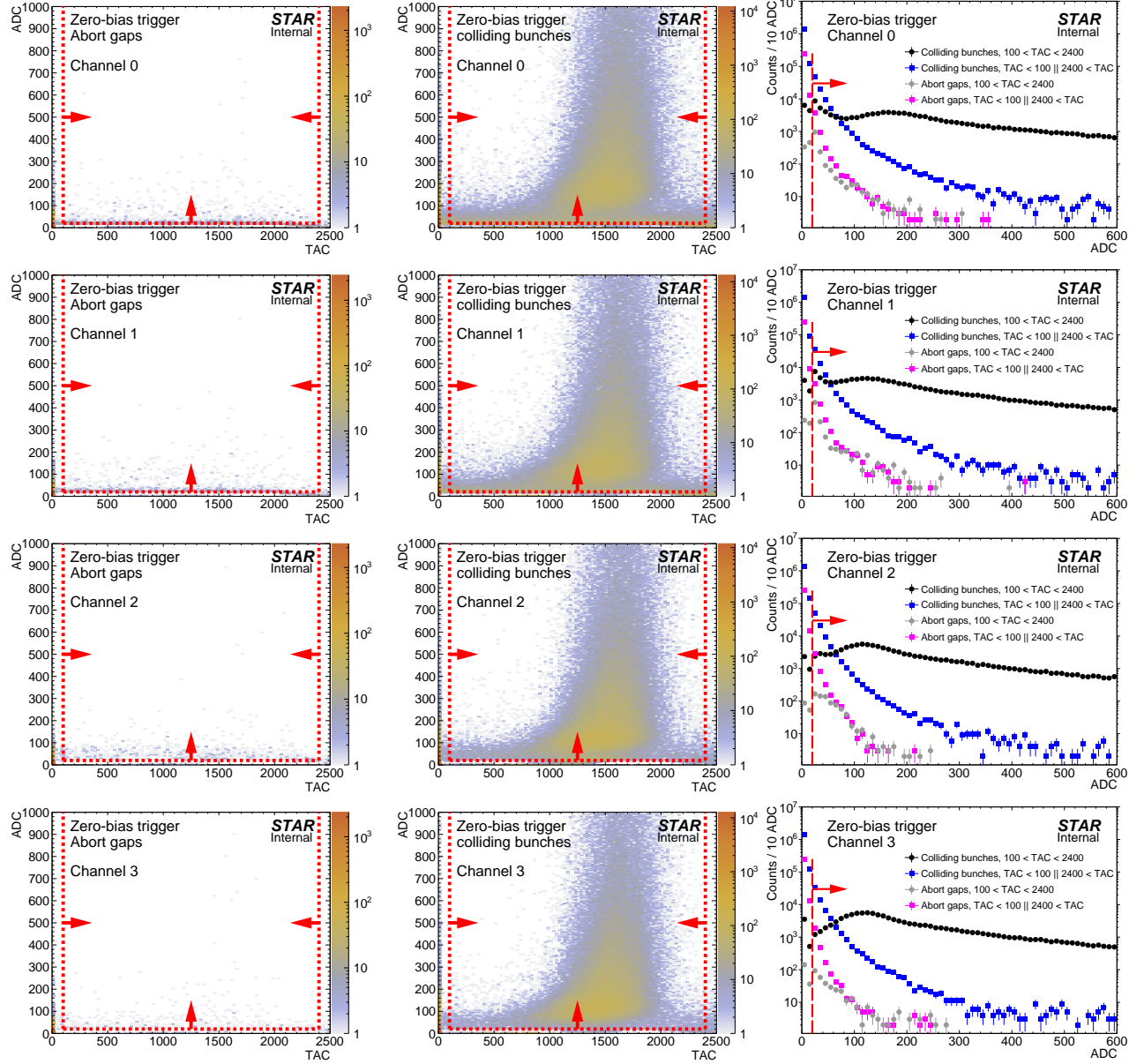
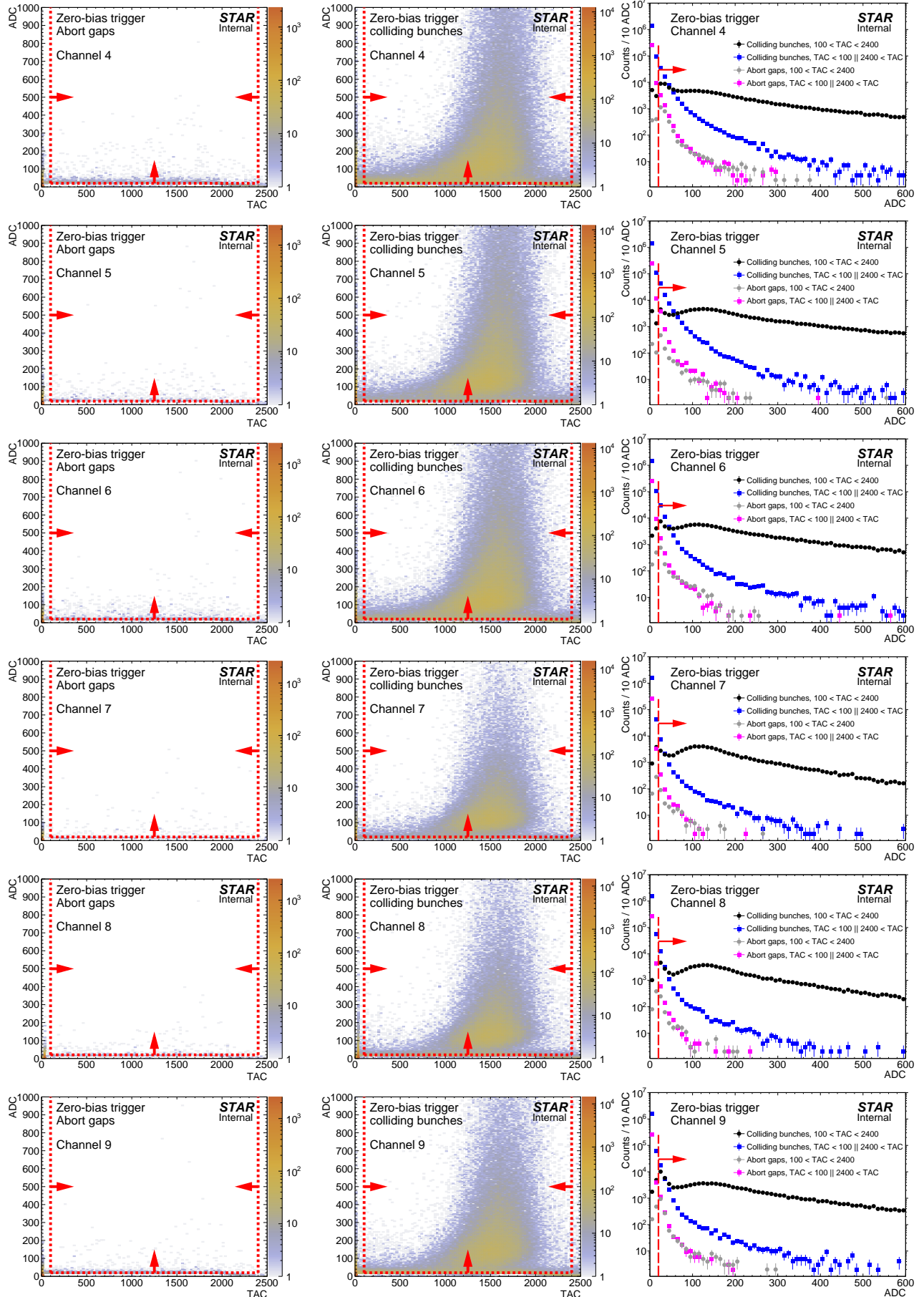


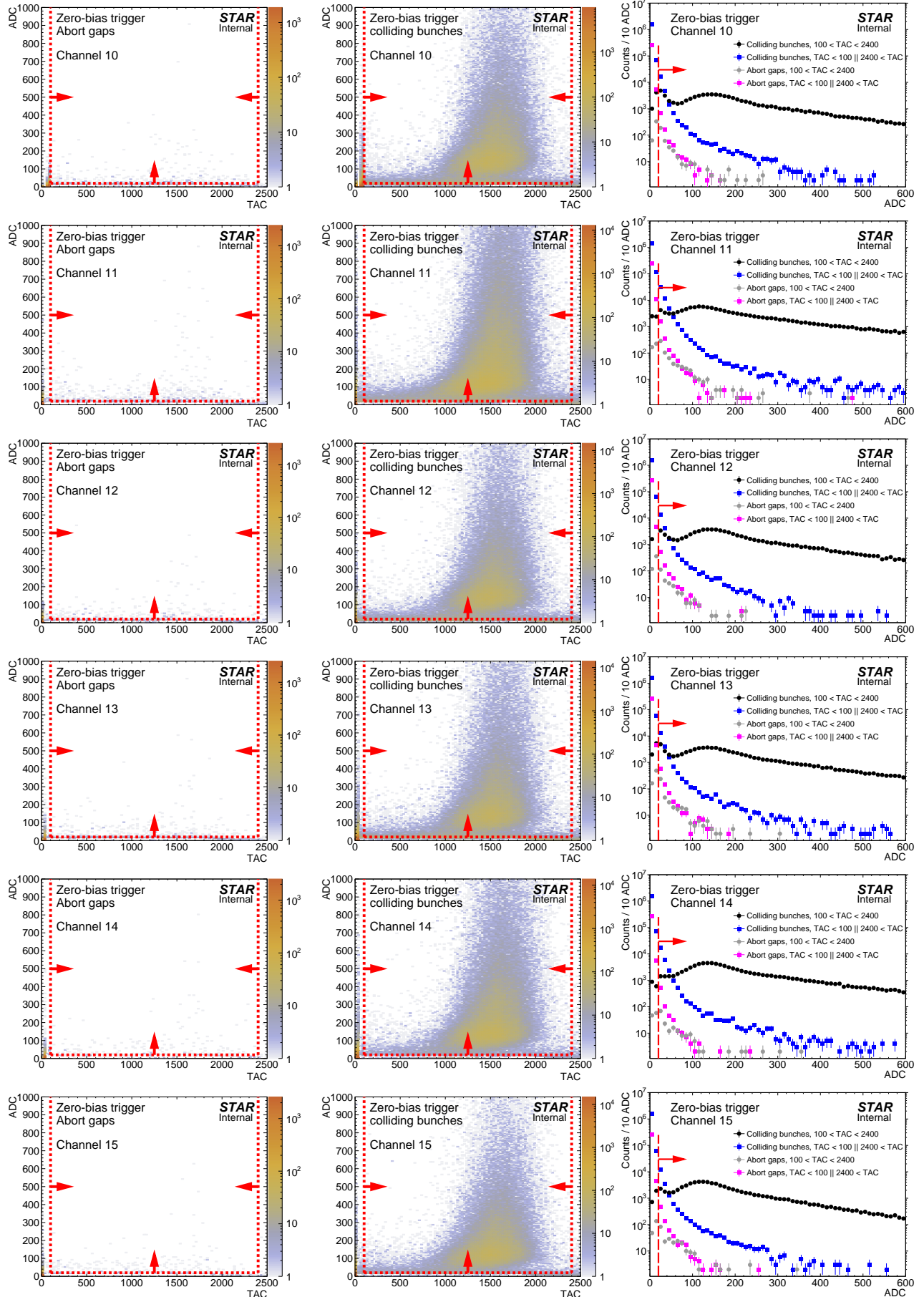
Figure 7.5: Cut flow.

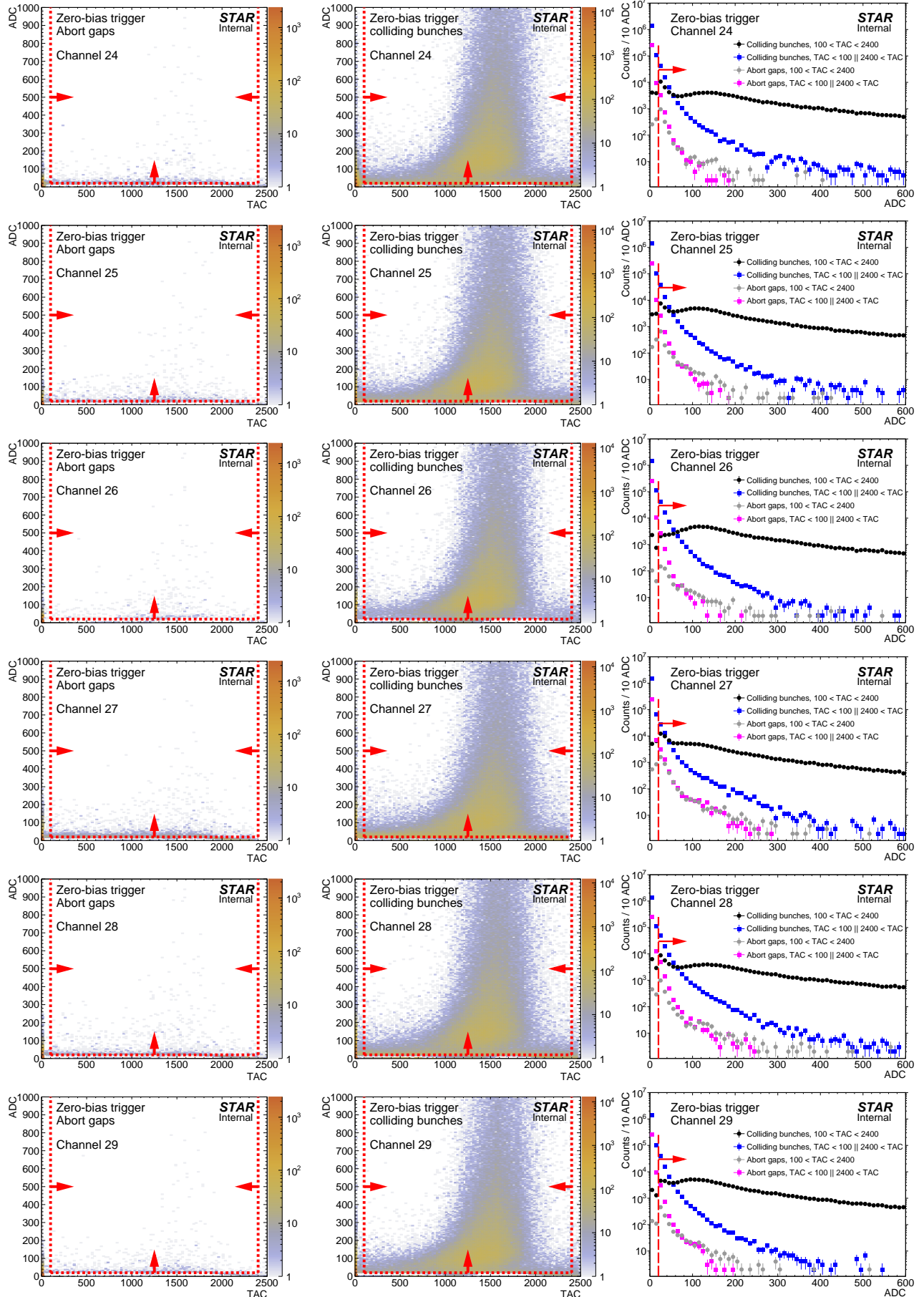
A. BBC response

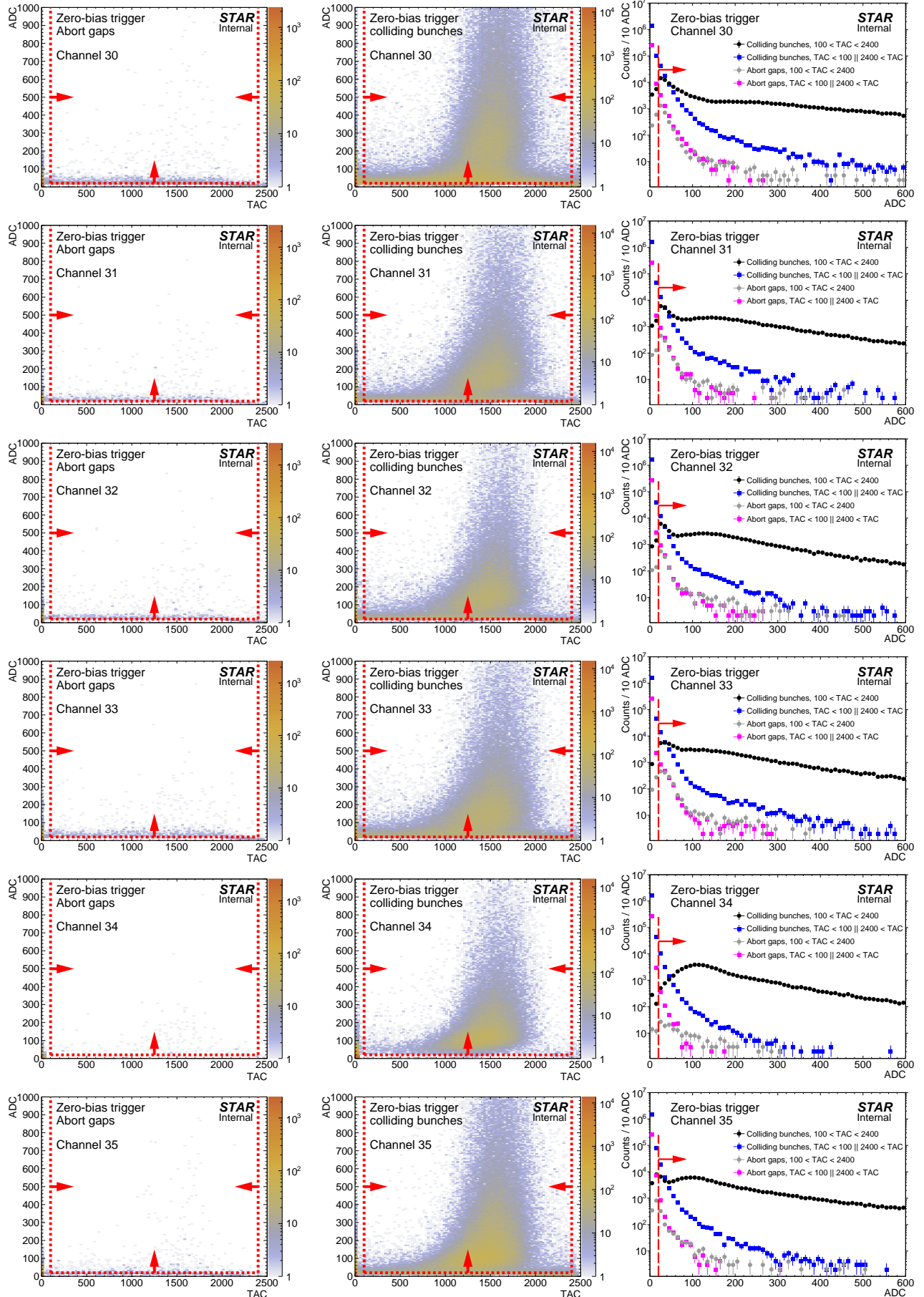
Figure A.1: Two-dimensional distribution of ADC vs. TAC counts per BBC-small channel in abort gaps (left) and colliding bunches (middle), and one-dimensional projection on x -axis (ADC) for selected ranges of TAC for colliding bunches and abort gaps (right). Each row represents single channel (small BBC tile). Red lines and arrows indicate thresholds for a signal in given channel.











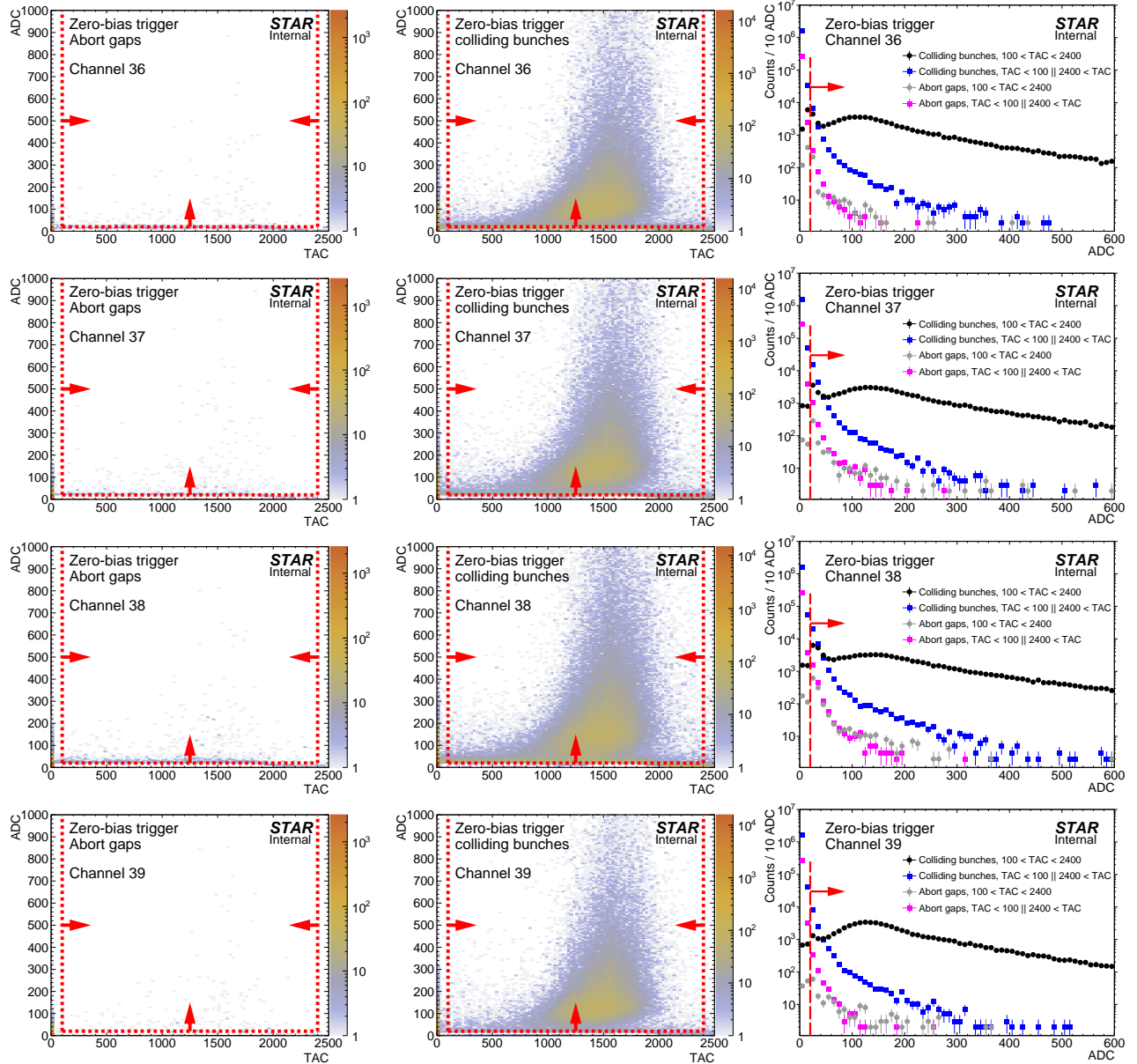
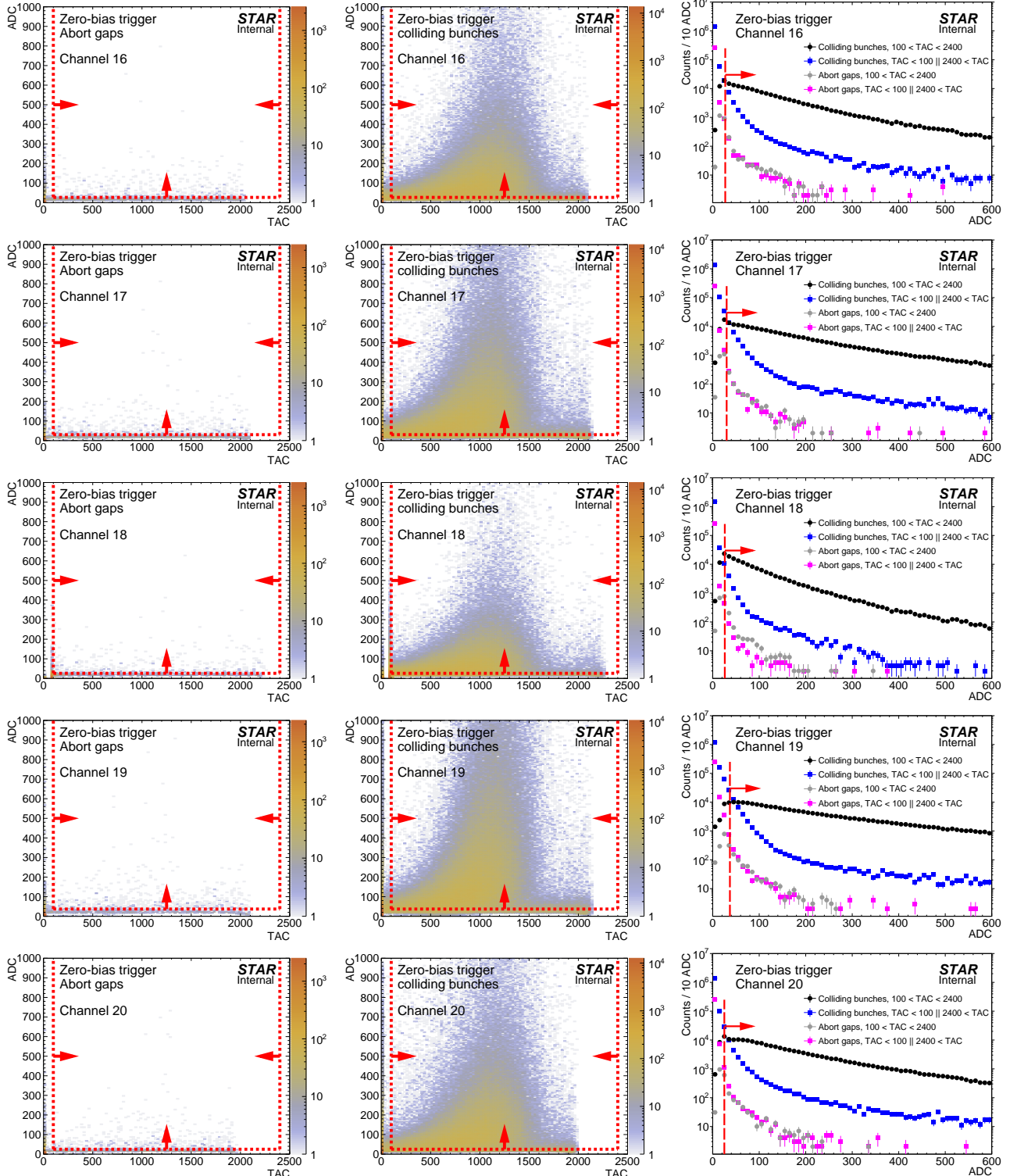
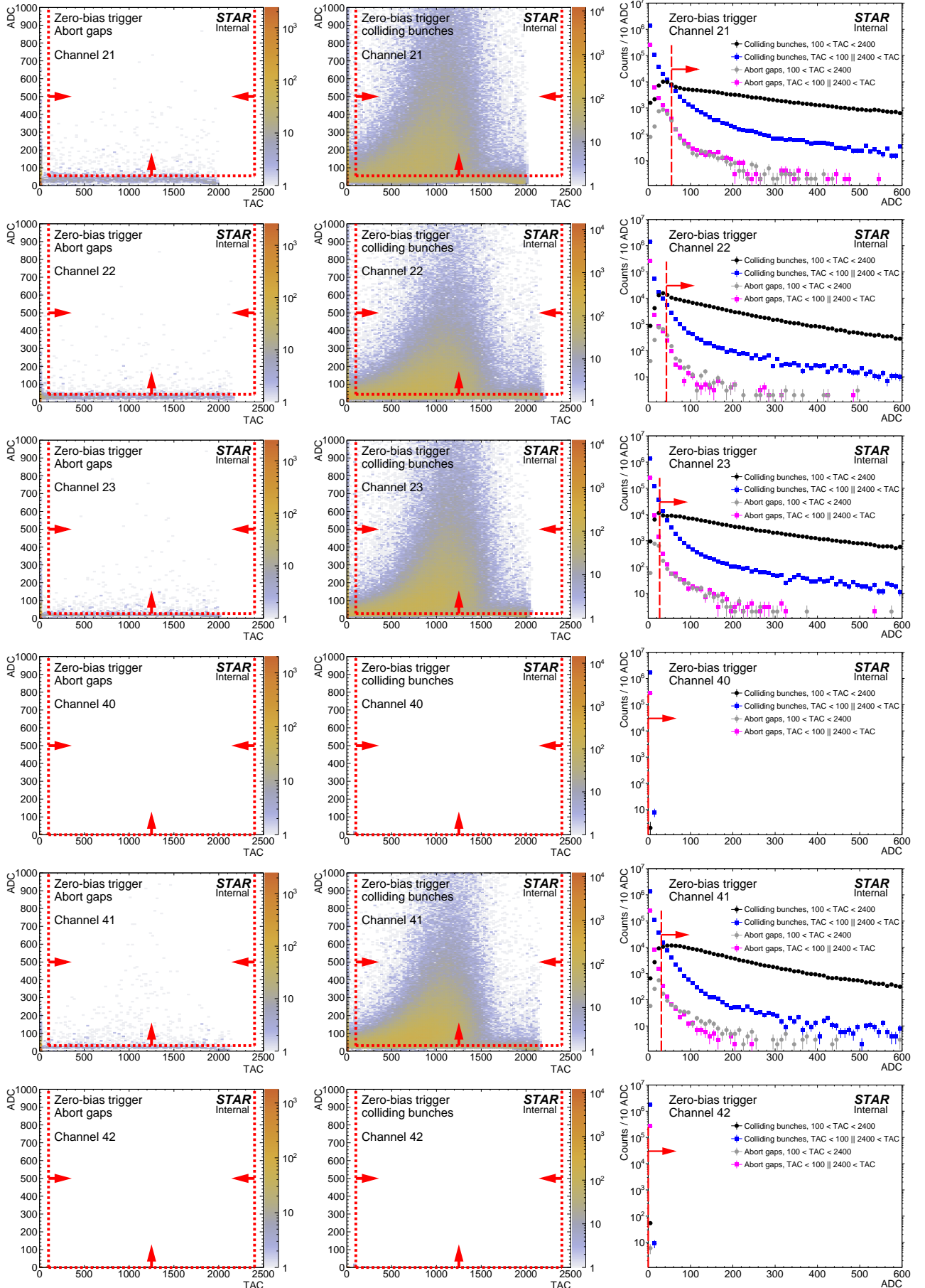
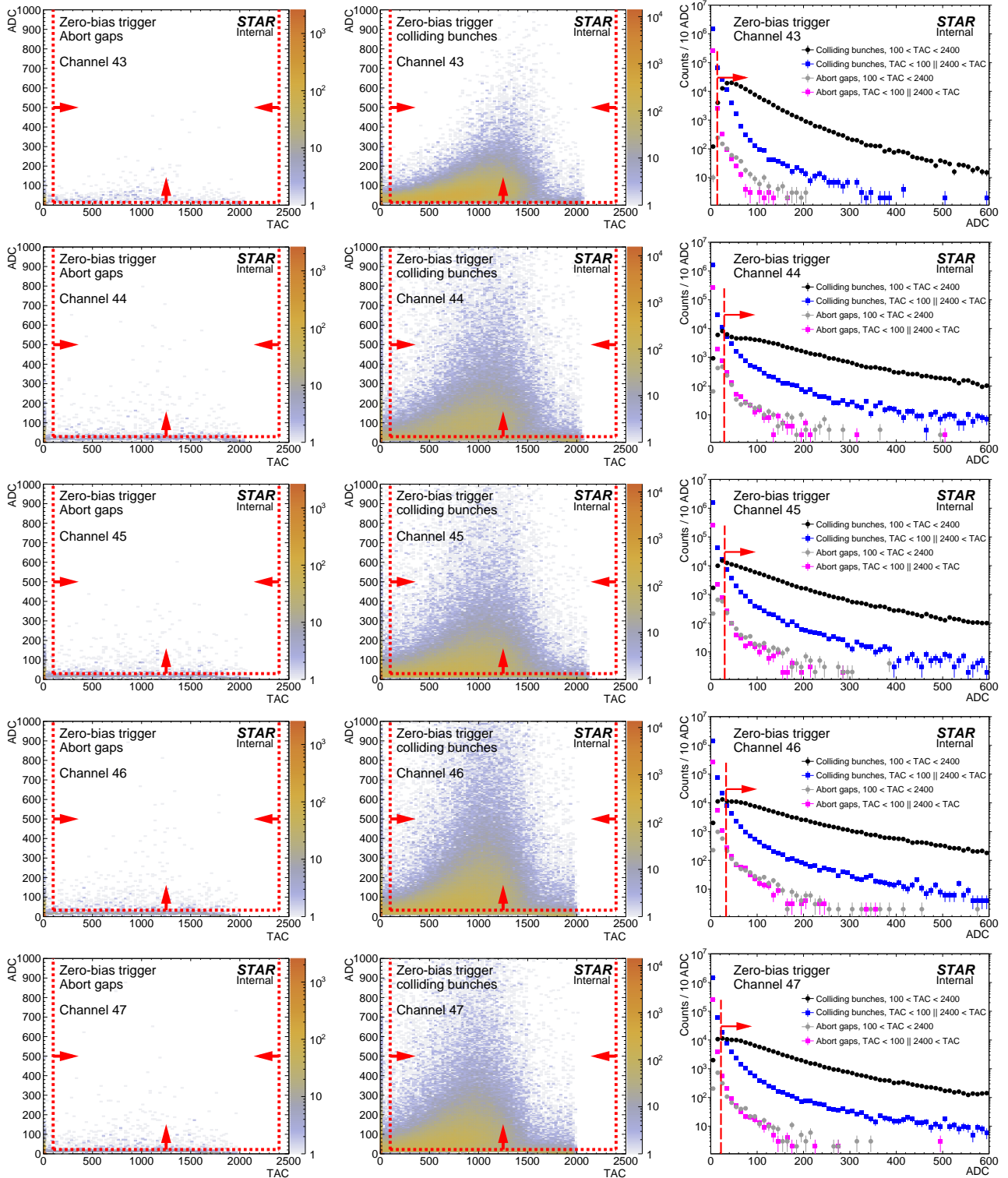


Figure A.2: Two-dimensional distribution of ADC vs. TAC counts per BBC-large channel in abort gaps (left) and colliding bunches (middle), and one-dimensional projection on x -axis (ADC) for selected ranges of TAC for colliding bunches and abort gaps (right). Each row represents single channel (large BBC tile). Red lines and arrows indicate thresholds for a signal in given channel.







B. Formulation of total RP efficiency

Definitions:

- RP^E - single good quality track (satisfying cuts C4.1-C4.2) on the east side,
- RP^W - single good quality track (satisfying cuts C4.1-C4.2) on the west side,
- TR^E - trigger signal in the RP branch with single good track on the east side,
- $TR^{\neq E}$ - trigger signal in the RP branch other than branch with single good track on the east side,
- TR^W - trigger signal in the RP branch with single good track on the west side,
- $TR^{\neq W}$ - trigger signal in the RP branch other than branch with single good track on the west side,
- $Veto$ - trigger veto on the simultaneous trigger signal in Up and Down RPs (ET&IT),
- $Veto^{PU}$ - trigger veto on ET&IT (Veto) due to pile-up interactions,
- $Veto^{DM}$ - trigger veto on ET&IT (Veto) due to forward proton interaction with dead material.

The total efficiency related to both east and west forward protons in CEP event has the following form:

$$\mathcal{E}(RP^E \wedge RP^W \wedge TR^E \wedge TR^W \wedge !Veto) = \mathcal{E}(RP^E \wedge RP^W | TR^E \wedge TR^W \wedge !Veto) \times \mathcal{E}(TR^E \wedge TR^W \wedge !Veto), \quad (B.1)$$

where the r.h.s. part of the equation is factorized using the rules of conditional probability to two components describing reconstruction and selection efficiency (first) and trigger efficiency (second).

The reconstruction and selection efficiency part can be represented as a product of single-proton reconstruction and selection efficiencies described in Sec. 4.2.3 with an additional scaling factor in the denominator:

$$\mathcal{E}(RP^E \wedge RP^W | TR^E \wedge TR^W \wedge !Veto) = \frac{\mathcal{E}(RP^E | TR^E \wedge !TR^{\neq E}) \times \mathcal{E}(RP^W | TR^W \wedge !TR^{\neq W})}{1 - \mathcal{E}(!RP^E \wedge !RP^W | TR^E \wedge TR^W \wedge !Veto)} \quad (B.2)$$

This denominator accounts for the fact that the efficiencies of the east and west RPs are correlated. To be more precise, unsuccessful reconstruction/selection of RP track on the east and west side in the same event can be a result of a pile-up interaction, typically of elastic proton-proton scattering, producing additional tracks/showers simultaneously in east and west RPs and thus introducing simultaneous east and west RP inefficiency. Without this factor the sole product of east and west efficiencies would account for discussed inefficiency twice - the total RP efficiency would be then underestimated. The effect is small (as can be read from Fig. 4.9), but we correct for it for completeness.

In the component of RP efficiency related to the trigger we can use again the conditional probability and factorize it to part connected with the trigger veto (first) and the efficiency of detecting a signal of both forward protons by the trigger system (second):

$$\mathcal{E}(TR^E \wedge TR^W \wedge !Veto) = \mathcal{E}(!Veto | TR^E \wedge TR^W) \times \mathcal{E}(TR^E \wedge TR^W). \quad (B.3)$$

Efficiency of the triggering $\mathcal{E}(TR^E \wedge TR^W)$ is basically 1. Efficiency of the (lack of) veto if forward protons are triggering in east and west RPs can be decomposed to efficiency of the veto induced by the pile-up interaction in the same bunch crossing ($Veto^{PU}$) and efficiency of the veto induced by the interaction of the CEP protons with the material of the accelerator and detectors ($Veto^{DM}$):

$$\begin{aligned} \mathcal{E}(!Veto | TR^E \wedge TR^W) &= \left| Veto = Veto^{PU} \vee Veto^{DM} \right| = \mathcal{E}(!Veto^{PU} \wedge !Veto^{DM} | TR^E \wedge TR^W) = \\ &= \mathcal{E}(!Veto^{DM} | !Veto^{PU} \wedge TR^E \wedge TR^W) \times \mathcal{E}(!Veto^{PU} | TR^E \wedge TR^W). \end{aligned} \quad (B.4)$$

The first term of the last part of Eq. (B.4) described in Sec. 4.2.1.2 can be safely factorized as the probability of veto induced by the primary CEP proton on the east side is totally independent from the similar probability on the west side:

$$\begin{aligned} \mathcal{E}(!Veto^{DM} | !Veto^{PU} \wedge TR^E \wedge TR^W) &= \\ &= \mathcal{E}^E(!Veto^{DM} | !Veto^{PU} \wedge TR^E \wedge TR^W) \times \mathcal{E}^W(!Veto^{DM} | !Veto^{PU} \wedge TR^E \wedge TR^W) \end{aligned} \quad (B.5)$$

The second term of the last part of Eq. (B.4) related with the pile-up is incorporated to overall efficiency of online and offline vetoes described in Sec. 4.2.2.3 - this is required by the correlation of vetoes, the possibility that vetoes in independent subdetectors take place in the same bunch crossing. This could happen if e.g. single diffraction event occurs on top of the CEP event, yielding a BBC signal and RP signal, both vetoing RP_CPT2 trigger.

C. Reconstruction of m_{TOF}^2

Definitions:

- t_0 - time of the primary pp interaction
- $t_{1,2}$ - time of detection of the hit in TOF by particle 1(2)
- $L_{1,2}$ - helical path of the particle 1(2) from the interaction vertex to the TOF cell with reconstructed hit,
- $p_{1,2}$ - magnitude of momentum of particle 1(2),
- $m_{1,2}$ - mass of particle 1(2),

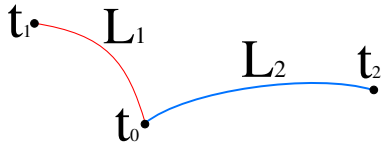


Figure C.1: Scheme of two central tracks of lengths L_1 and L_2 , produced in common vertex in moment t_0 , hitting cells in TOF detector in moments t_1 and t_2 .

From the simple algebra below which describes relation between track lengths, momenta and times of hit detection one can derive formula for the squared mass of two particles, assuming that their masses are equal (particles are of the same type).

Below we assume $c = 1$. We can write a set of two equations connecting the time that it takes for each particle to reach the TOF, starting from the interaction vertex:

$$\begin{cases} t_1 - t_0 = L_1 \sqrt{1 + \frac{m_1^2}{p_1^2}}, \\ t_2 - t_0 = L_2 \sqrt{1 + \frac{m_2^2}{p_2^2}}. \end{cases} \quad (\text{C.1})$$

By adding the two equations above we get

$$\Delta t = t_1 - t_2 = L_1 \sqrt{1 + \frac{m_1^2}{p_1^2}} - L_2 \sqrt{1 + \frac{m_2^2}{p_2^2}}. \quad (\text{C.2})$$

In CEP of two opposite-sign particles always the same species of particles are produced, therefore

$$m_1 = m_2 = m. \quad (\text{C.3})$$

If we substitute m_1 and m_2 with m in Eq. (C.2) and transform the equation to remove the square roots we get a quadratic equation of the form

$$\mathcal{A} \times (m_{\text{TOF}}^2)^2 + \mathcal{B} \times m_{\text{TOF}}^2 + \mathcal{C} = 0. \quad (\text{C.4})$$

Parameters of the Eq. (C.4) are given below:

$$\mathcal{A} = -2 \frac{L_1^2 L_2^2}{p_1^2 p_2^2} + \frac{L_1^4}{p_1^4} + \frac{L_2^4}{p_2^4}, \quad (\text{C.5})$$

$$\mathcal{B} = -2 L_1^2 L_2^2 \left(\frac{1}{p_1^2} + \frac{1}{p_2^2} \right) + \frac{2 L_1^4}{p_1^2} + \frac{2 L_2^4}{p_2^2} - 2 (\Delta t)^2 \left(\frac{L_1^2}{p_1^2} + \frac{L_2^2}{p_2^2} \right), \quad (\text{C.6})$$

$$\mathcal{C} = (\Delta t)^4 - 2 (\Delta t)^2 (L_1^2 + L_2^2) + L_1^4 + L_2^4 - 2 L_1^2 L_2^2, \quad (\text{C.7})$$

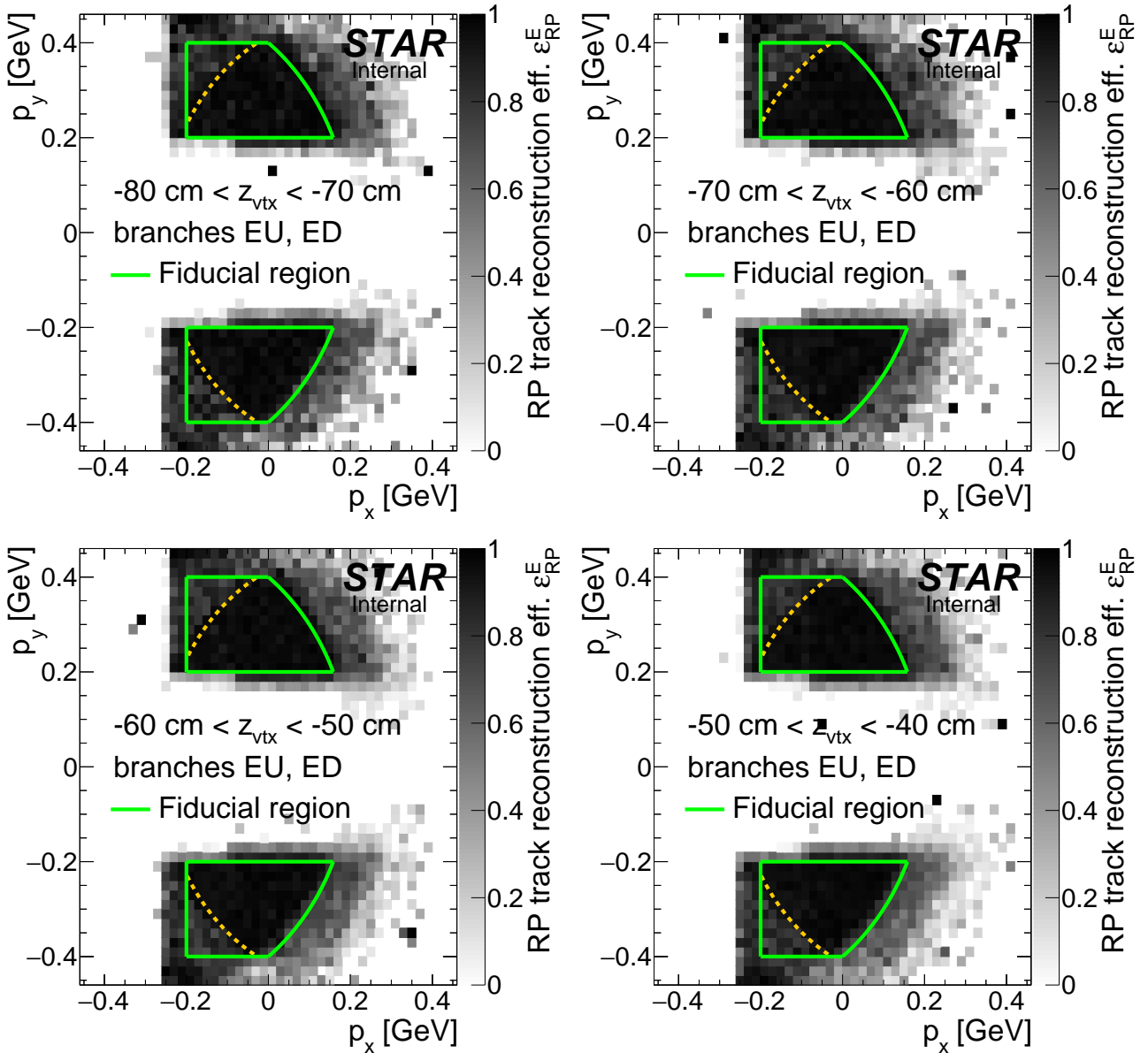
together with the final formula for a physical root of the quadratic equation which is used in the m_{TOF}^2 reconstruction:

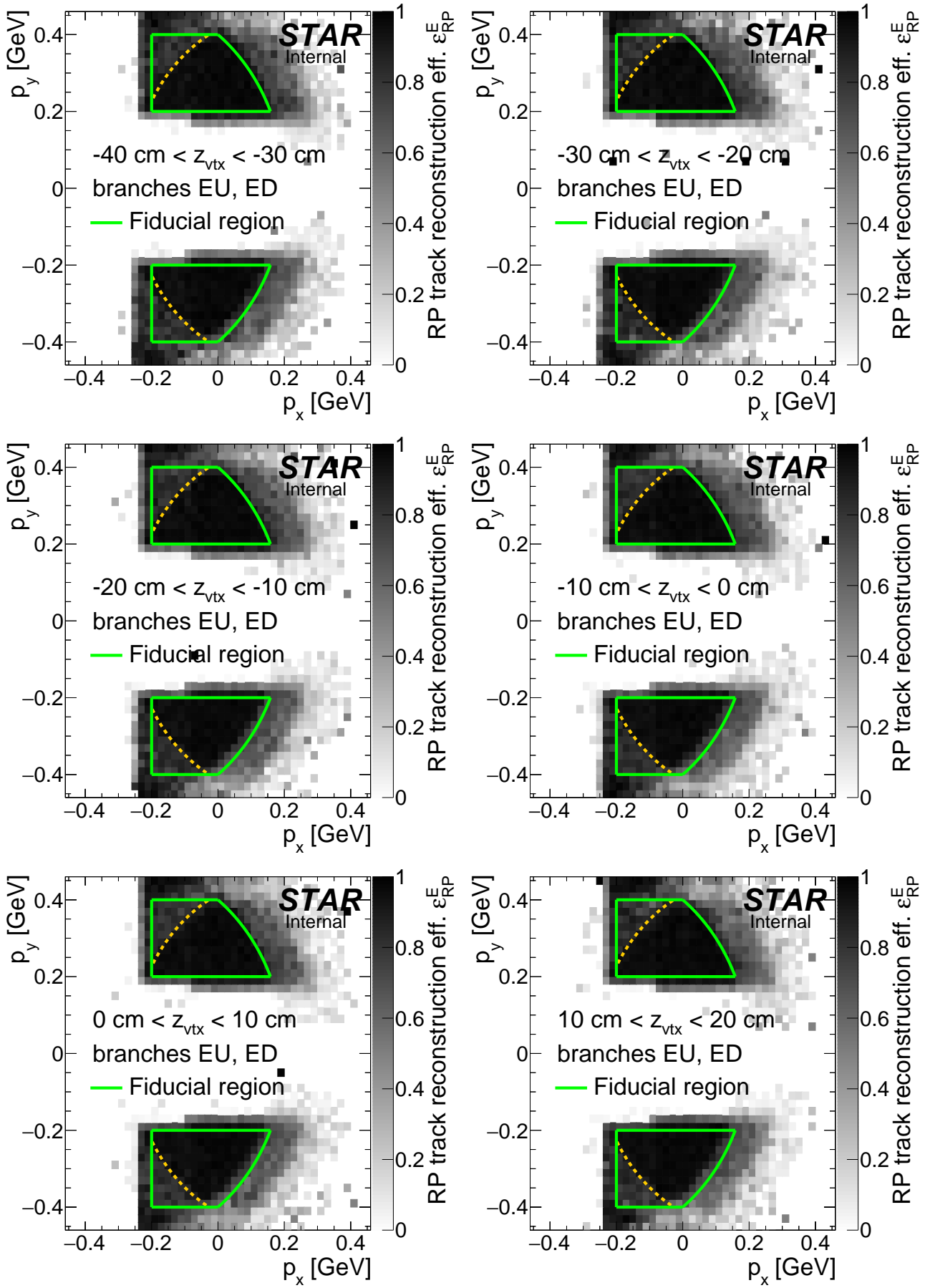
$$m_{\text{TOF}}^2 = \frac{-\mathcal{B} + \sqrt{\mathcal{B}^2 - 4\mathcal{A}\mathcal{C}}}{2\mathcal{A}}. \quad (\text{C.8})$$

D. RP efficiency

D.1 RP track acceptance, reconstruction and selection efficiency

Figure D.1: RP track acceptance, reconstruction and selection efficiency on the east side obtained from MC simulation embedded into zero-bias data. Each plot corresponds to z -vertex range given in the plot.





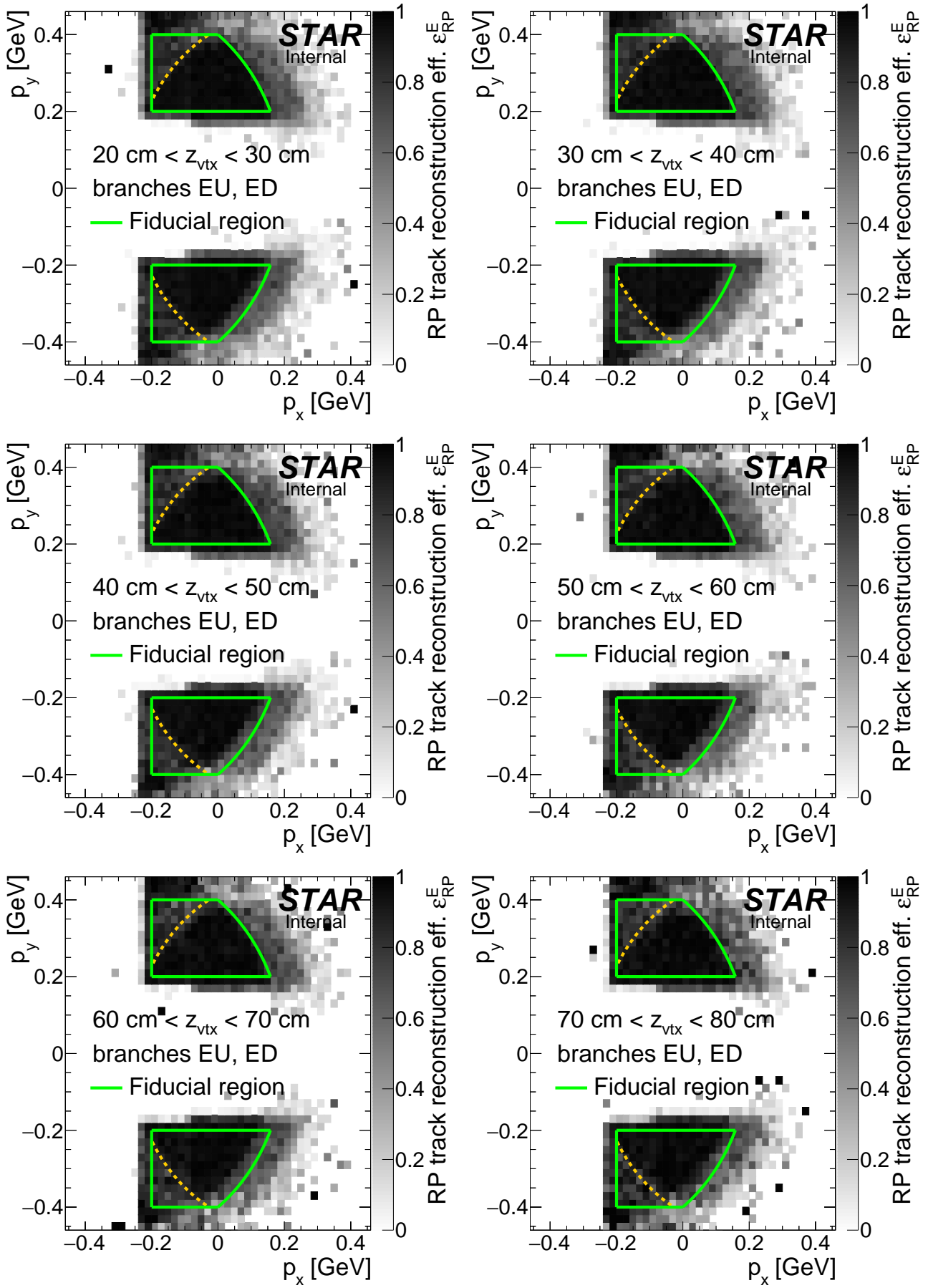
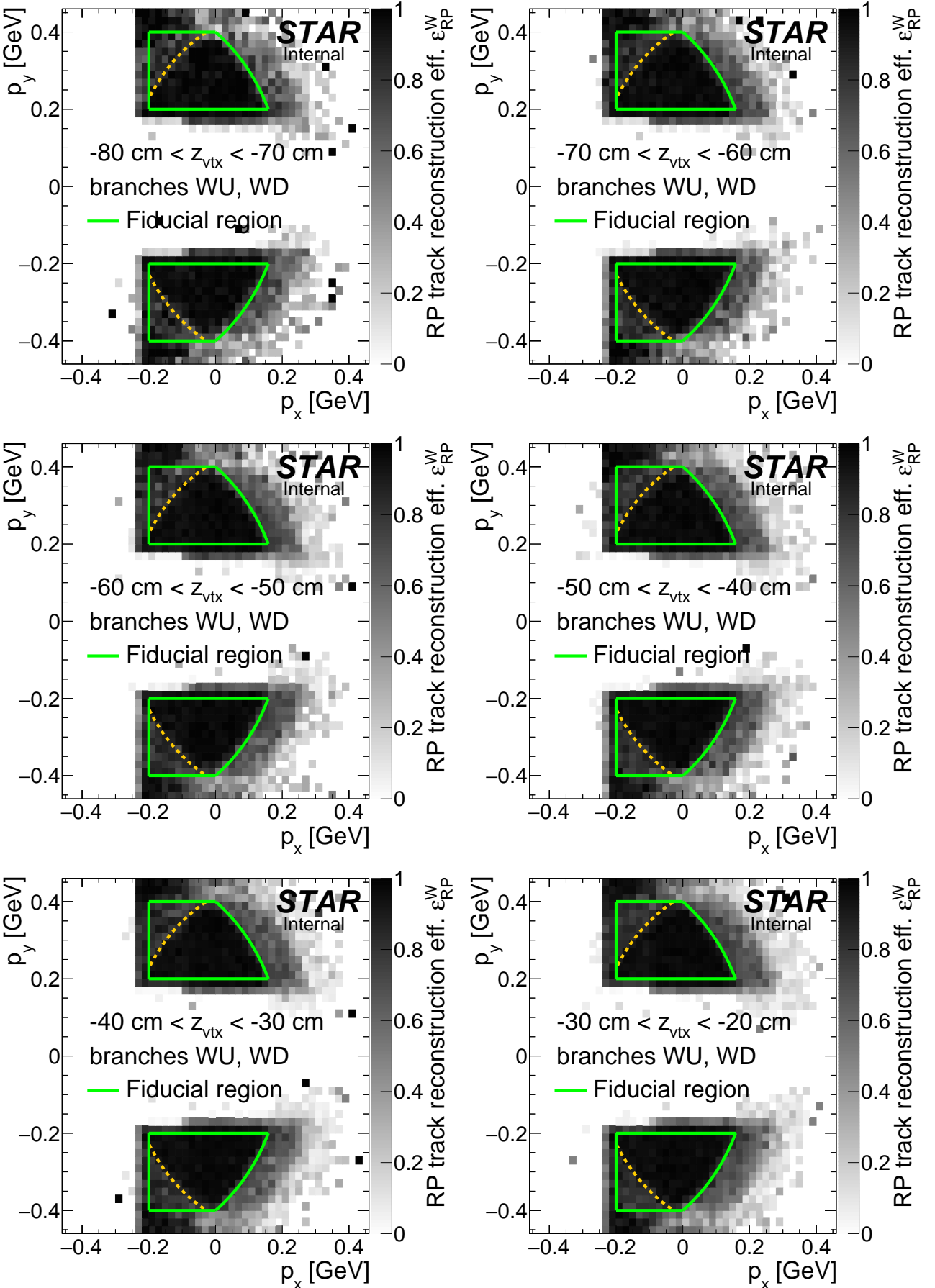
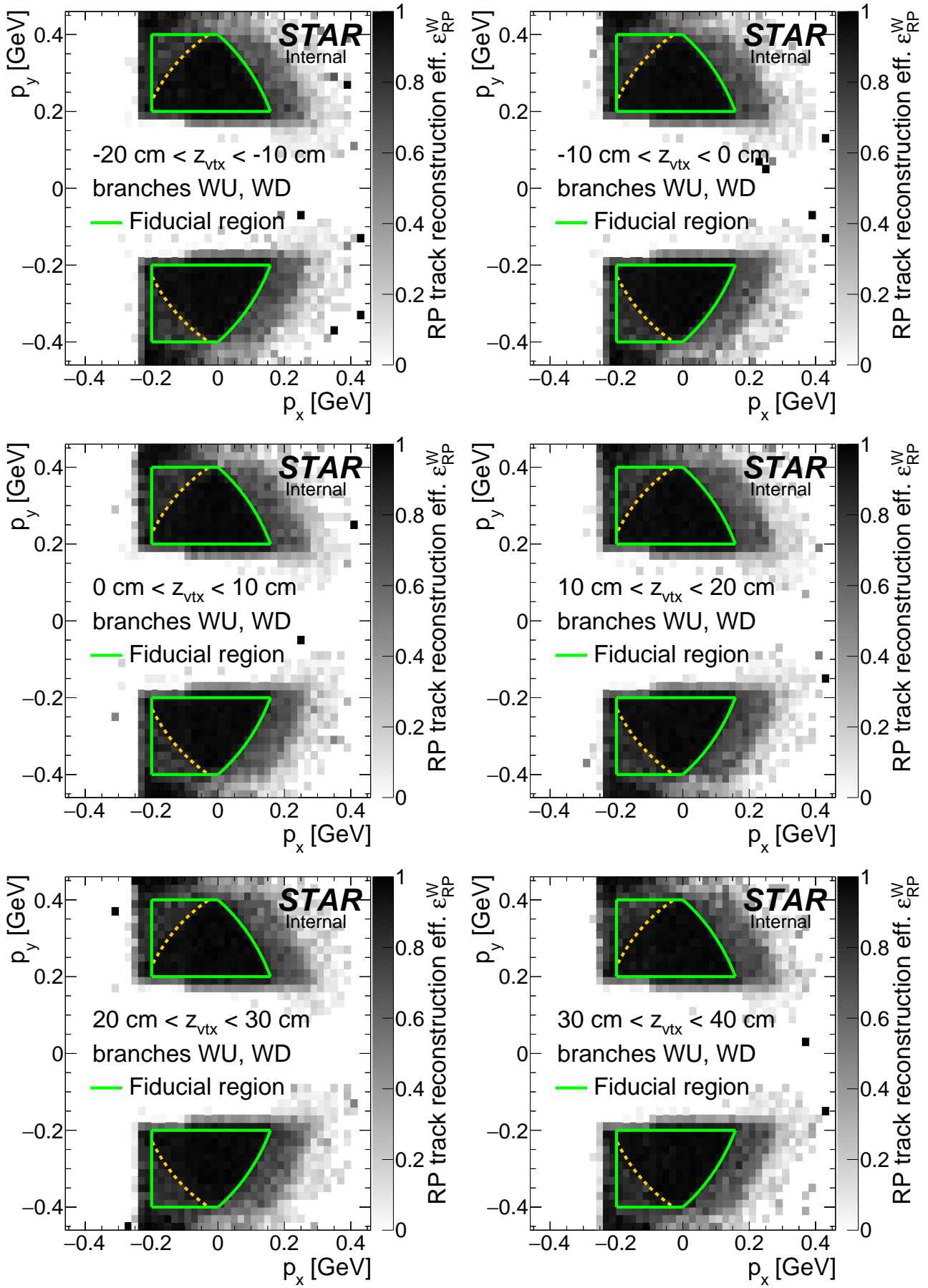
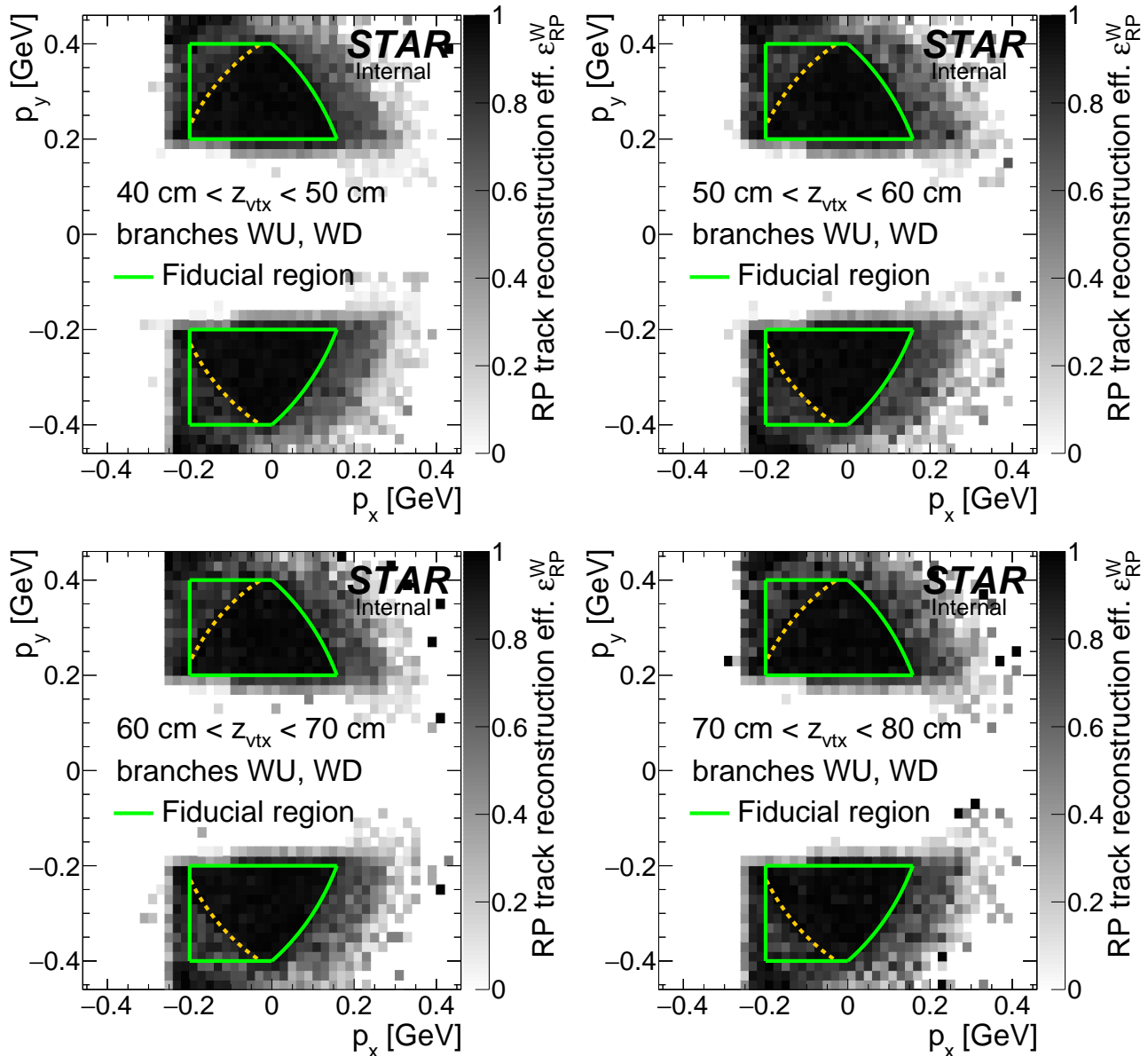


Figure D.2: RP track acceptance, reconstruction and selection efficiency on the west side obtained from MC simulation embedded into zero-bias data. Each plot corresponds to z -vertex range given in the plot.

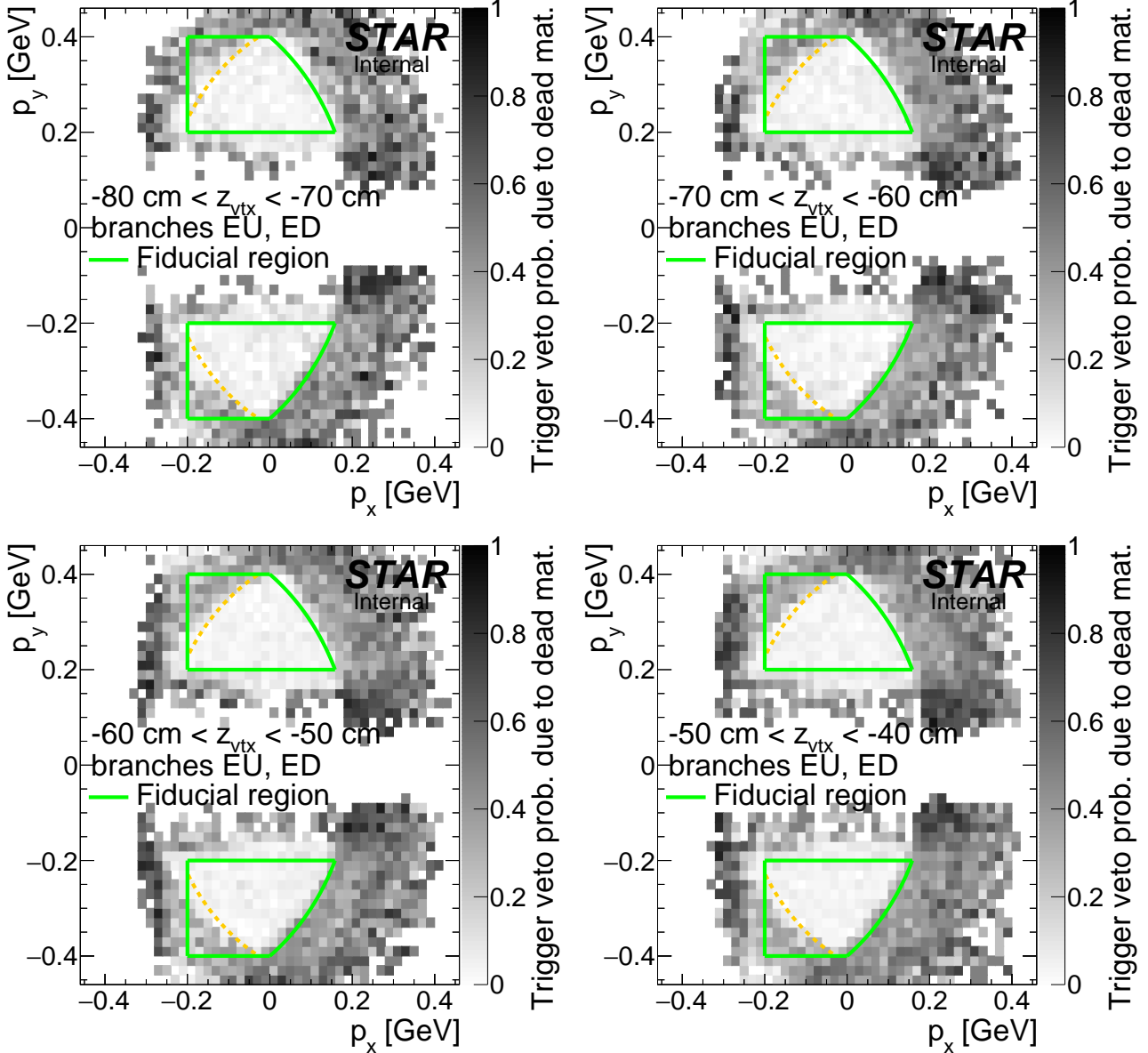


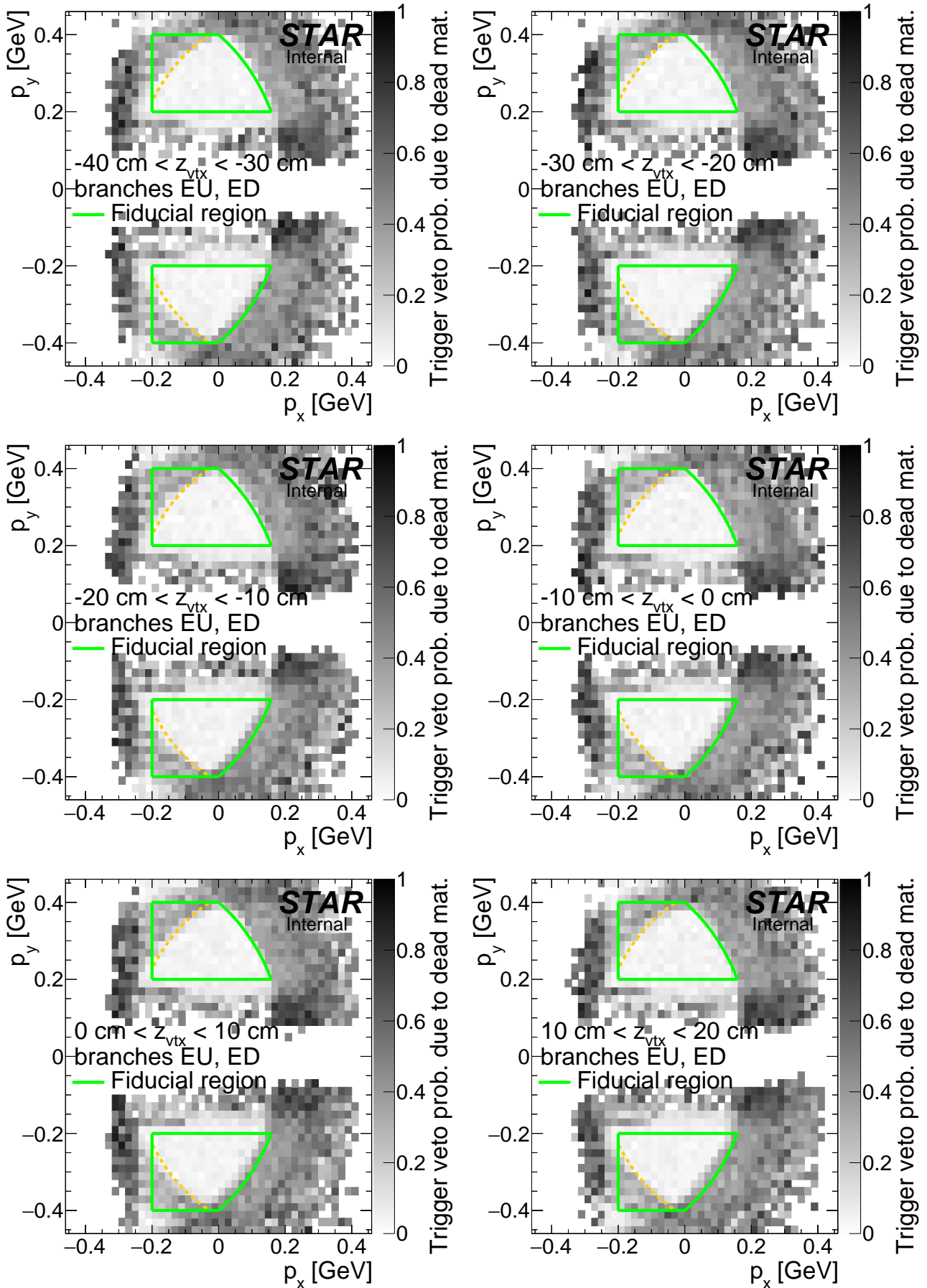




D.2 RP trigger veto probability related to dead material

Figure D.3: Probability of ET&IT trigger veto due to forward proton interaction with dead material on the east side. Results were obtained from forward proton MC simulation embedded into zero-bias data. Each plot corresponds to z -vertex range given in the plot.





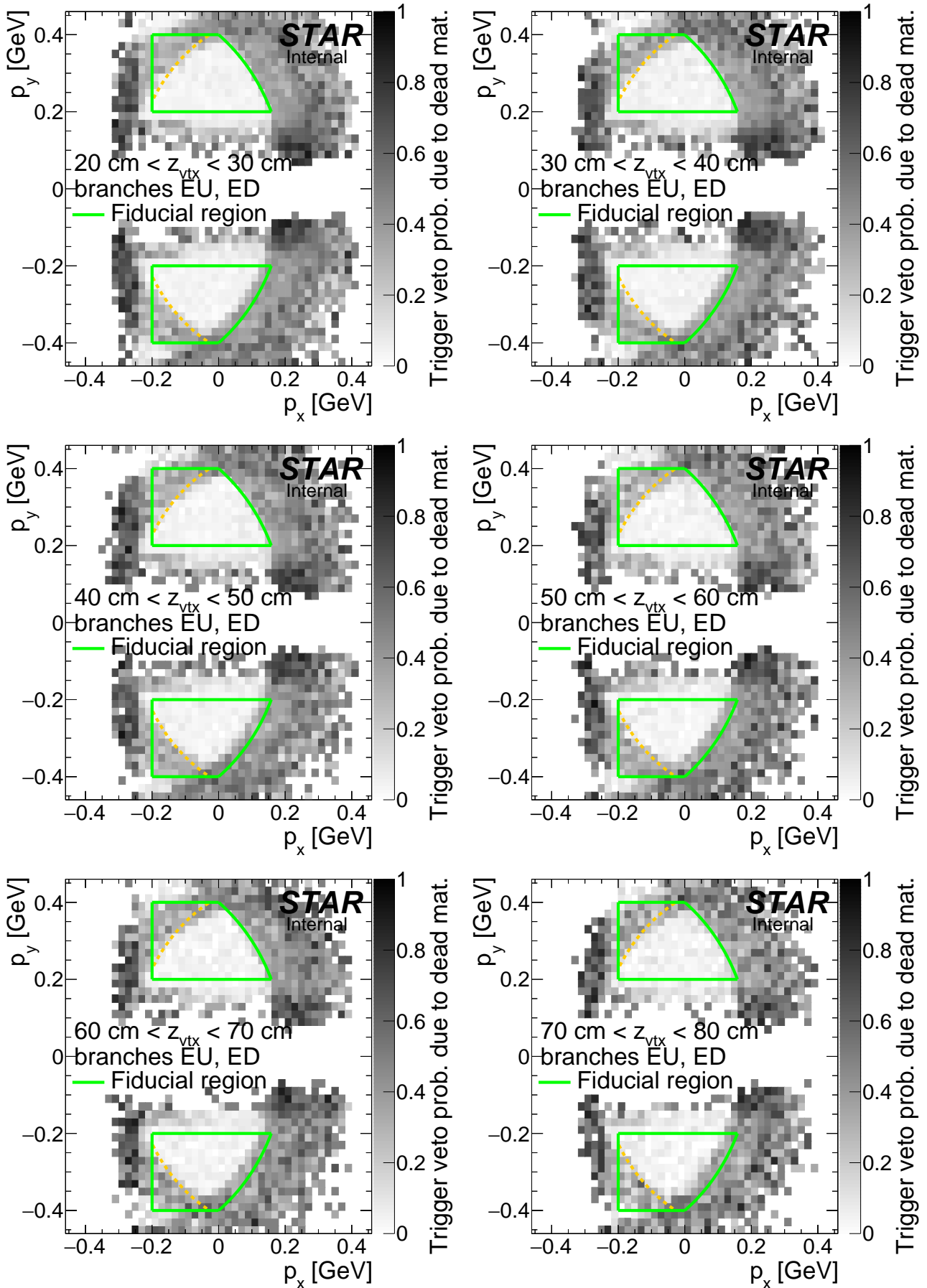
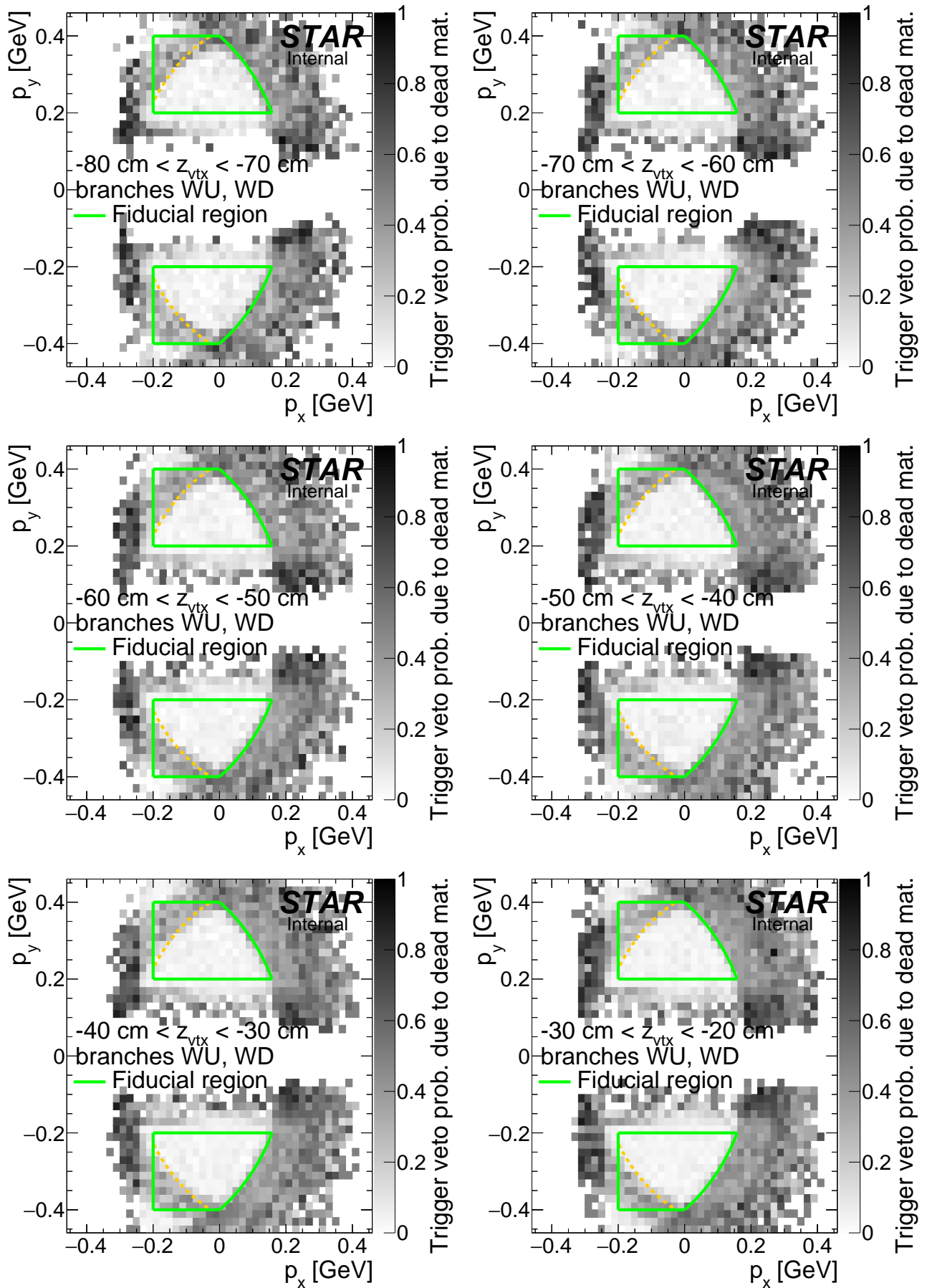
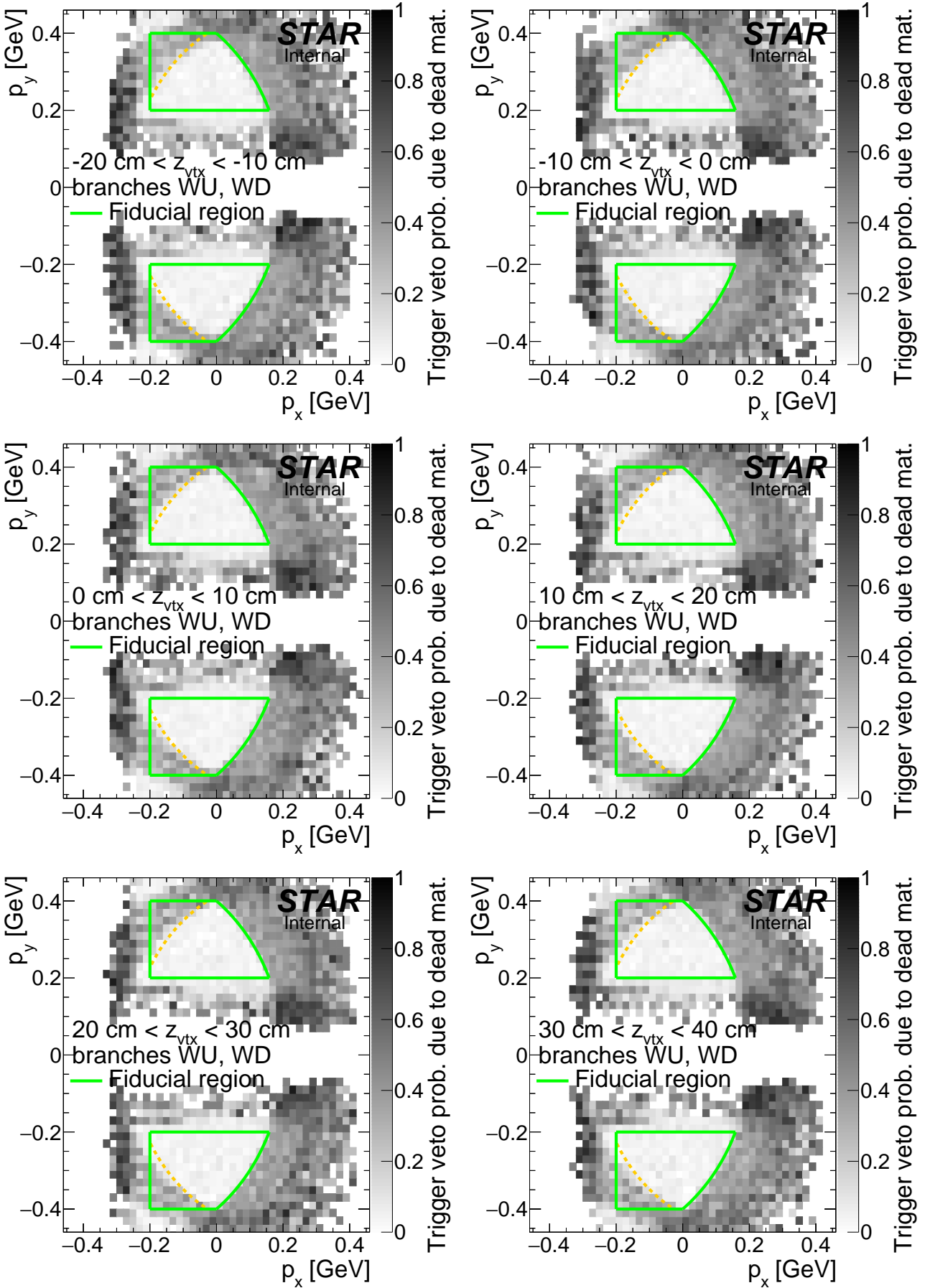
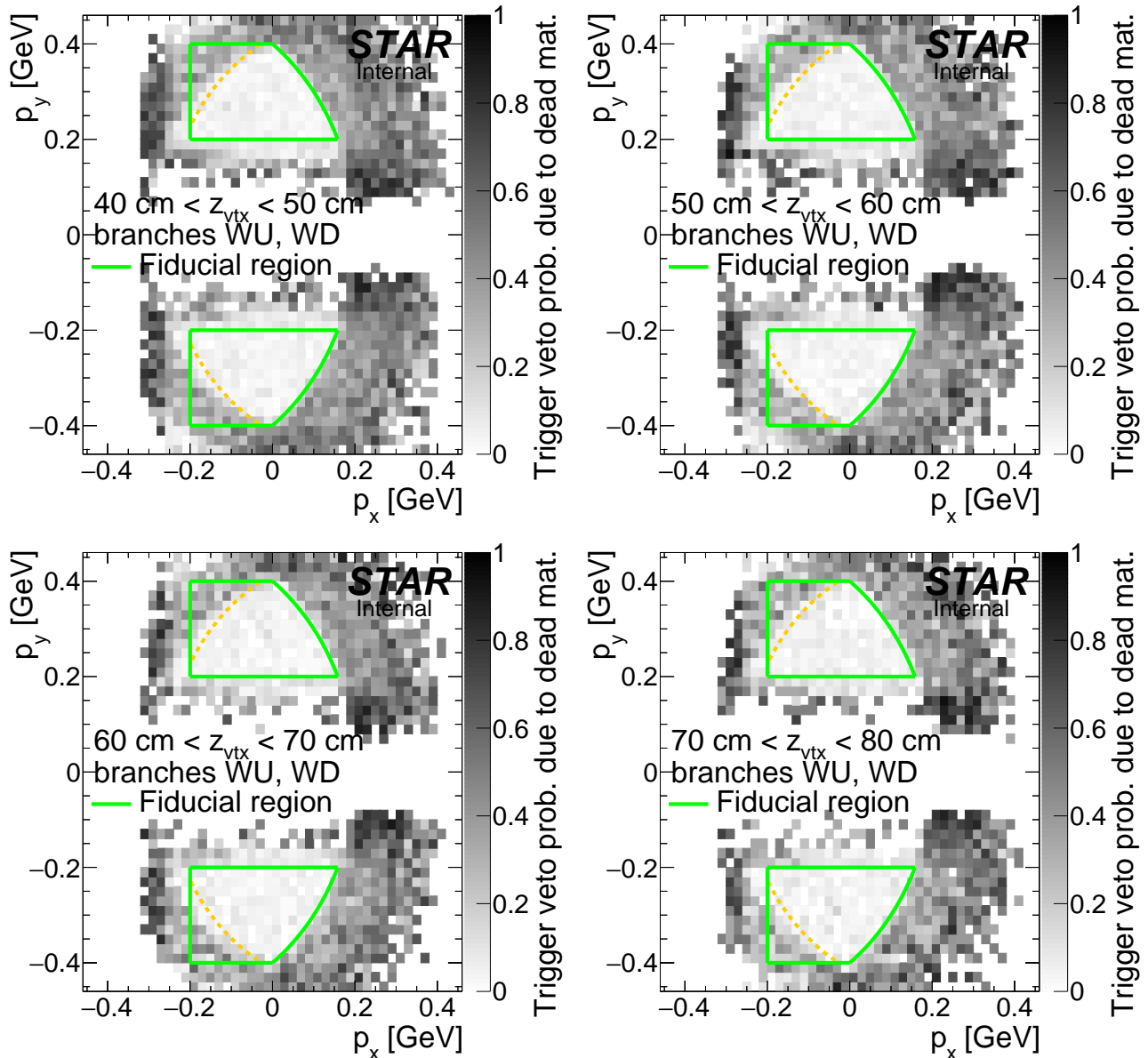


Figure D.4: Probability of ET&IT trigger veto due to forward proton interaction with dead material on the west side. Results were obtained from forward proton MC simulation embedded into zero-bias data. Each plot corresponds to z -vertex range given in the plot.







E. Particle identification efficiency

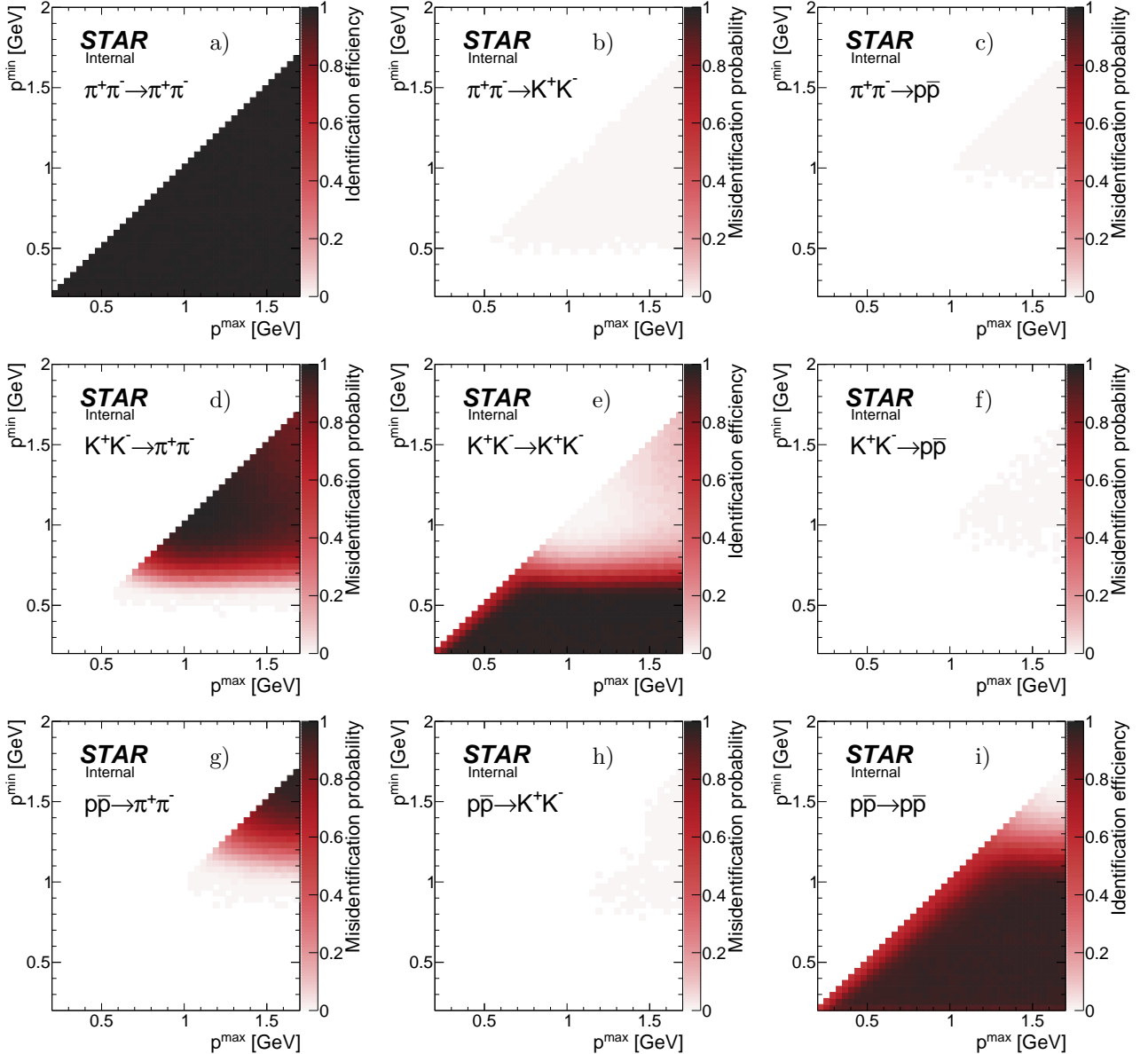


Figure E.1: Pair identification efficiency (diagonal) and misidentification probability (off-diagonal) as a function of tracks' p for $\pi^+\pi^-$, K^+K^- and $p\bar{p}$ pairs. The results were obtained from the dedicated MC simulation described in Sec. 4.2.2.5.

List of Figures

1.1	Diagram of DIPE process.	5
1.2	CEP represented in η - ϕ space.	5
1.3	Central Production event at STAR.	5
2.1	Sketch of the trigger components used in definitions of diffractive triggers in run 15.	7
3.1	Primary vertex multiplicity. Red arrow marks bin with events with exactly one primary vertex (with track(s) matched with hit in TOF), which are used in physics analysis.	10
3.2	z -position of the primary vertex in single TOF vertex events. Red dashed line indicate range of longitudinal vertex position accepted in analysis.	10
3.3	Multiplicity of primary TPC tracks matched with hit in TOF for single TOF vertex events	11
3.4	Distribution of a distance in $\eta - \phi$ space between the BEMC cluster closest to primary TPC track (R_{\min})	11
3.5	Comparison of distribution of $N_{\text{hits}}^{\text{fit}}$, $N_{\text{hits}}^{\text{dE/dx}}$ and $N_{\text{hits}}^{\text{fit}}/N_{\text{hits}}^{\text{poss}}$ in the data and embedded MC	12
3.6	Comparison of distribution of track η and ϕ in the data and embedded MC	13
3.7	Correlation and difference of z -vertex position measured in Roman Pots and TPC.	14
3.8	Sample BBC-small and BBC-large response in zero-bias triggers.	15
3.9	Probability of false BBC-large signal (noise-induced).	16
3.10	NTofClusters.	16
3.11	Correlation between sum of corresponding momentum components (x in Fig. 3.11a and y in Fig. 3.11b) of Roman Pot proton tracks and TPC tracks.	17
3.12	MissingPt.	17
3.13	Correlation between $n\sigma^{\text{pair}}$ from TPC for $\pi^+\pi^-$, K^+K^- and $p\bar{p}$.	18
3.14	Correlation between m^2 from TOF and $n\sigma^{\text{pair}}$ from TPC for $\pi^+\pi^-$, K^+K^- and $p\bar{p}$.	18
3.15	Squared particle mass from TOF for candidates of given PID selected based on dE/dx in TPC.	18
4.1	Overall efficiency of the online BBC-small and ZDC veto as a function of instantaneous luminosity.	19
4.2	Sample probability of ET&IT trigger veto due to forward proton interaction with dead material.	21
4.3	Sample distribution of z_{vtx} with fitted normal distribution.	22
4.4	Mean and width of the z_{vtx} distribution as a function of the RHIC fill number.	22
4.5	Overall efficiency of online and offline cuts as a function of instantaneous luminosity.	23
4.6	dE/dx error vs. TOF path length and $\log_2(dx)$ vs. TOF path length for exclusive event candidates.	24
4.7	Pair identification efficiency and misidentification probability as a function of tracks' p_T .	25
4.8	Sample RP track reconstruction efficiency in a single z -vertex bin.	26
4.9	Probability of simultaneous inefficiency of the RP track reconstruction calculated from the CEP MC embedded into zero-bias data.	26
4.10	Sketch with definition of Δz_0 .	26
4.11	Distribution of Δz_0 together with fraction of non-exclusive background.	28
4.12	Vertexing efficiency.	28
5.1	Missing pT.	29
5.2	Graph illustrating the misidentification problem.	29
7.1		32

7.2	33
7.3	34
7.4	35
7.5	Cut flow.	36
A.1	Distribution of ADC vs. TAC counts (2D) and ADC conunts (1D) per BBC-small channel in abort gaps and colliding bunches.	37
A.2	Distribution of ADC vs. TAC counts (2D) and ADC conunts (1D) per BBC-large channel in abort gaps and colliding bunches.	43
C.1	Scheme of two central tracks with common vertex, hitting cells in TOF detector.	48
D.1	RP track acceptance, reconstruction and selection efficiency on the east (MC embedded into zero-bias data).	49
D.2	RP track acceptance, reconstruction and selection efficiency on the west (MC embedded into zero-bias data).	52
D.3	Probability of ET&IT trigger veto due to forward proton interaction with dead material on the east.	55
D.4	Probability of ET&IT trigger veto due to forward proton interaction with dead material on the west.	58
E.1	Pair identification efficiency and misidentification probability as a function of tracks' p .	61

List of Tables

2.1	Central Diffraction physics triggers and control triggers involving Roman Pot detectors in run 15.	7
3.1	Offline ADC thresholds in BBC-large.	16

References

- [1] L. Adamczyk, L. Fulek, and R. Sikora, “Supplementary note on diffractive analyses of 2015 proton-proton data.” <https://drupal.star.bnl.gov/STAR/blog/rafals/supplementary-note-diffractive-analyses-2015-proton-proton-data>, January, 2019.
- [2] P. D. B. Collins, *An Introduction to Regge Theory and High-Energy Physics*. Cambridge Monographs on Mathematical Physics. Cambridge Univ. Press, Cambridge, UK, 2009.
<http://www-spires.fnal.gov/spires/find/books/www?cl=QC793.3.R4C695>.
- [3] S. Donnachie, H. G. Dosch, O. Nachtmann, and P. Landshoff, *Pomeron physics and QCD*, vol. 19. 2002.
- [4] V. Barone and E. Predazzi, *High-Energy Particle Diffraction*, vol. v.565 of *Texts and Monographs in Physics*. Springer-Verlag, Berlin Heidelberg, 2002.
<http://www-spires.fnal.gov/spires/find/books/www?cl=QC794.6.C6B37::2002>.
- [5] P. Lebiedowicz and A. Szczurek, “Exclusive $pp \rightarrow pp\pi^+\pi^-$ reaction: From the threshold to LHC,” *Phys. Rev.* **D81** (2010) 036003, [arXiv:0912.0190 \[hep-ph\]](https://arxiv.org/abs/0912.0190).
- [6] P. Lebiedowicz, O. Nachtmann, and A. Szczurek, “Central exclusive diffractive production of $\pi^+\pi^-$ continuum, scalar and tensor resonances in pp and $p\bar{p}$ scattering within tensor pomeron approach,” *Phys. Rev.* **D93** no. 5, (2016) 054015, [arXiv:1601.04537 \[hep-ph\]](https://arxiv.org/abs/1601.04537).
- [7] L. A. Harland-Lang, V. A. Khoze, and M. G. Ryskin, “Modelling exclusive meson pair production at hadron colliders,” *Eur. Phys. J.* **C74** (2014) 2848, [arXiv:1312.4553 \[hep-ph\]](https://arxiv.org/abs/1312.4553).
- [8] R. Fiore, L. Jenkovszky, and R. Schicker, “Resonance production in Pomeron–Pomeron collisions at the LHC,” *Eur. Phys. J.* **C76** no. 1, (2016) 38, [arXiv:1512.04977 \[hep-ph\]](https://arxiv.org/abs/1512.04977).
- [9] F. E. Close and A. Kirk, “A Glueball - q anti-q filter in central hadron production,” *Phys. Lett.* **B397** (1997) 333–338, [arXiv:hep-ph/9701222 \[hep-ph\]](https://arxiv.org/abs/hep-ph/9701222).
- [10] <https://online.star.bnl.gov/rp/pp200/>.
- [11] <https://online.star.bnl.gov/RunLogRun15/>.
- [12] <http://www.star.bnl.gov/protected/common/common2015/trigger2015/lumipp200GeV/>.
- [13] I. Alekseev and J. H. Lee, “Trigger Definitions for RP phase-II* for Run15.”
https://drupal.star.bnl.gov/STAR/system/files/trigger_updated_run15_v2.doc, December, 2014.
- [14] I. Alekseev, “Trigger with Roman Pots Phase II*.”
https://drupal.star.bnl.gov/STAR/system/files/trigger4RP2_v2.pdf, December, 2014.
- [15] R. Sikora, “Naming convention and layout of the Roman Pot Phase II* subsystem in the STAR experiment.” https://drupal.star.bnl.gov/STAR/system/files/RomanPotNomenclature_0.pdf, October, 2014.
- [16] <http://www.star.bnl.gov/public/comp/prod/DataSummary.html>.
- [17] <https://drupal.star.bnl.gov/STAR/event/2017/09/27/software-and-computing-meeting/revertexing-2015-rp-stream>.
- [18] L. Adamczyk. https://drupal.star.bnl.gov/STAR/system/files/talk_42.pdf, March, 2016.
- [19] <https://github.com/rafalsikora/CEP-STAR>.

- [20] R. A. Kycia, J. Chwastowski, R. Staszewski, and J. Turnau, “GenEx: A simple generator structure for exclusive processes in high energy collisions,” *Commun. Comput. Phys.* **24** no. 3, (2018) 860–884, arXiv:1411.6035 [hep-ph].